Estimation of fading time and irradiation dose in thermoluminescence dosimetry using uni- and multivariate analysis techniques

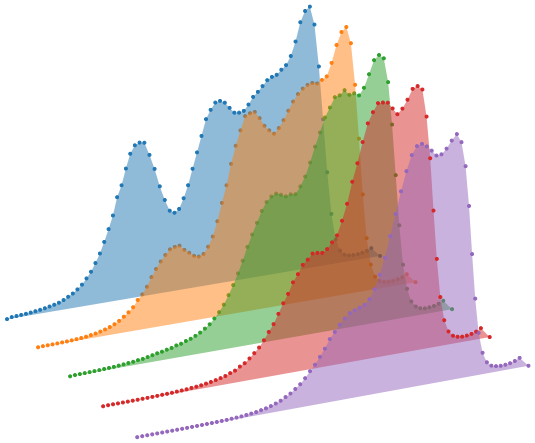

Dissertation
zur Erlangung des akademischen Grades
Doktor der Naturwissenschaften

vorgelegt von
Robert Theinert
geboren in Hamm

Lehrstuhl für Experimentelle Physik IV
Fakultät Physik
Technische Universität Dortmund
2018

1. Gutachter:	Prof. Dr. Kevin Kröninger
2. Gutachter:	Prof. Dr. Dr. Wolfgang Rhode
Prüfungsvorsitz:	Prof. Dr. Dmitri Yakovlev
Prüfungsbeisitz:	Dr. Bärbel Siegmann

Datum der Disputation: 12.10.2018

Abstract

Fading influences are a crucial point in dosimetry using thermoluminescence dosemeters. Due to thermal fading, the thermoluminescence signal decreases over time resulting in a potential underestimation of the irradiation dose.
This thesis presents two techniques for a fading time independent irradiation dose estimation. Both methods are based on glow curve deconvolution.

In the first approach, the fraction of signal photons of two peaks in the glow curve is used to estimate fading time and irradiation dose. The second approach is based on a multivariate analysis using a neural network with multiple features as inputs to predict the fading time and the irradiation dose.

The measurements presented in this thesis are performed within the context of the TL-DOS project, in which the monitoring service of the Materialprüfungsamt North Rhine-Westphalia and the Lehrstuhl Experimentelle Physik IV at the TU Dortmund are developing a new thermoluminescence dosemeter system for application in routine personal dosimetry.

Kurzfassung

Bei der Verwendung von Thermolumineszenzdetektoren in der Dosimetrie sind Fadingeinflüsse ein entscheidender Faktor. Durch das thermische Faden nimmt das Thermolumineszenzsignal im Laufe der Zeit ab, was zu einer Unterschätzung der berechneten Dosis führen kann.
In dieser Arbeit werden zwei Techniken vorgestellt, mit denen es möglich ist, eine von der Fadingzeit unabhängige Dosis zu berechnen. Beide Ansätze basieren auf einer Zerlegung der Glühkurve in ihre einzelnen Peaks.

Im ersten Ansatz wird der Anteil der Signalphotonen an der gesamten Glühkurve verwendet, um die Fadingzeit und die Dosis zu bestimmen. Der zweite Ansatz basiert auf einer Multivariaten Analyse, in der ein neuronales Netz mit mehreren Eingangsvariablen benutzt wird, um die Fadingzeit und die Dosis vorherzusagen.

Die Messungen in dieser Arbeit wurden im Rahmen des TL-DOS Projektes durchgeführt, in dem die Personendosismessstelle des Materialprüfungsamts Nordrhein-Westfalen und der Lehrstuhl Experimentelle Physik IV an der TU Dortmund ein Thermolumineszenzdosimetriesystem entwickeln, das in der amtlichen Personendosimetrie eingesetzt werden soll.

Contents

Chapter 1

Introduction

> *"I also brought [a diamond] to some kind of glimmering light, by taking it into bed with me, and holding it a good while upon a warm part of my naked body in the darkness of his bed room."* 1663, Robert Boyle [1]

In 1663 Robert Boyle was the first one who reported on the phenomenon of thermoluminescence (TL) by heating a diamond. Since then a lot of experiments investigated the phenomenon and found many different materials which exhibit TL. However, a theoretical description of the phenomenon was presented by Randall and Wilkins [2] only in 1945. In the late 1940s and early 1950s the development of dosemeters based on TL began.

Nowadays, TL dosemeters are commonly used in various fields of radiation protection dosimetry such as environmental or personal dosimetry. They all take advantage of the correlation between the amount of incident radiation and the measured photon counts during heating in order to estimate an irradiation dose.
However, due to thermal stimulation, the measured signal decreases over time after the irradiation, the so-called fading, resulting in an underestimation of the irradiation dose. To overcome the influence of fading on the estimated irradiation dose, different techniques have been investigated. However, most approaches suffer from a loss of information and the corresponding loss of accuracy on the estimated irradiation dose.

The main goal of this thesis is to estimate an irradiation dose independent of the elapsed time between irradiation and readout without losing accuracy. Two different techniques are developed based on the investigation of photon counts as a function of the temperature, the so-called glow curve.
First the fading time is estimated based on one variable, the fading ratio which is the fraction of signal photons of two peaks in the glow curve. With the known fading time the irradiation dose can be estimated independent of the elapsed time between irradiation and readout. The uncertainties on the fading time as well as on the irradiation dose are investigated.

As a second approach, multiple variables are used in a multivariate analysis (MVA) to estimate the fading time and reduce the corresponding uncertainties. In addition, the measured data is used to study several detector and reader characteristics.

The Materialprüfungsamt North Rhine-Westphalia, which is one of the four monitoring services in Germany, is developing a new thermoluminescence dosemeter system (TL-DOS) for application in routine personal dosimetry. In the context of this project, the fading time and irradiation studies are performed.

A theoretical background of personal dosimetry, the phenomenon of TL and the TL-DOS project is given in Chapter 2. The model, with which the glow curves are analyzed, is presented in Chapter 3 including background investigations and a reconstruction of the temperature.
To study the fading time and irradiation dose dependency of the TL dosemeters, multiple measurements, summarized in Chapter 4, are performed. The recorded data set also offers the possibility to investigate several detector and reader characteristics which are discussed in Chapter 5. The detector response is studied as a function of the amount of sensitive material and the influence of a reflective layer is investigated. Furthermore, a sensitivity decrease of the TL reader used during the measurements is observed and characterized as well as the contribution of natural radiation to fading measurements.
A first approach to estimate the fading time and the irradiation dose, which is based on one variable, is introduced in Chapter 6 including robustness tests and the uncertainty estimation of the calculated fading time and irradiation dose.
In Chapter 7, a second technique using a neural network to estimate the fading time is described as well as the corresponding uncertainty estimation. Furthermore the two possible estimations of the irradiation dose are presented and further applications of an MVA in the context of dosimetry are given. The thesis is concludes with a summary and an outlook.

Parts of this dissertation were already published in [3, 4].

Chapter 2

Theoretical considerations

2.1 Dosimetry

Radiation causes damage in human body and living tissue, respectively. Thus, it can be very dangerous to human life. However, radiation can also be very helpful, e.g. for diagnostic in medicine, material screening or for safety control by using x-ray scanners for luggage inspection.
Consequently it is desirable to use radiation under supervised conditions. These conditions of radiation protection are regulated in Germany by the "Strahlenschutzverordnung" (StrlSchV) [5] and the "Röntgenverordnung" (RoeV) [6]. The aim of the legal radiation protection is to enable the handling with radioactive sources and simultaneously avoid deterministic damage and reduce stochastic defects to below an acceptable threshold.

If radiation interacts with material it deposits energy. The mean deposited energy per mass D depends on the material and is given in units of Gy ($1\,\mathrm{Gy} = 1\,\mathrm{J/kg} = 1\,\mathrm{m^2/s^2}$). To determine and assess the influence of radiation to human body, protection quantities are defined like the equivalent and the effective dose.

The equivalent dose H takes into account the effects of different radiation types on human tissue. Each type of radiation is weighted with a different factor w_R which represents the potential risk for human tissue of the irradiation type, e.g. $w_R = 1$ for beta- and gamma-radiation, but $w_R = 20$ for alpha-irradiation. H is then calculated as the weighted sum of absorbed dose.

The effective dose E considers the susceptibility of different organs to irradiation damage. It is calculated as a weighted sum of H over tissues as follows:

$$E = \sum_T w_T H_T = \sum_T w_T \sum_R w_R D_{T,R} \tag{2.1}$$

with $\sum_T w_T = 1$ as the weighting factors for tissue, w_R as the weighting factor for the radiation type, $D_{T,R}$ as the mean absorbed dose from radiation type R in tissue T. The values of the weighting factors are given in the recommendations of the International Commission on Radiological Protection (ICRP) [7].

Both, the equivalent and the effective dose are measured in units of Sv ($1\,\mathrm{Sv} = 1\,\mathrm{J/kg}$). In comparison to Gy, Sv includes the biological effect to human tissue. Based on this protection dose quality, legal limits are defined.

However, it is impossible to measure the protection quantities directly and thus, operative quantities are defined. The most important quality in personal dosimetry is the personal dose equivalent $H_\mathrm{p}(d)$, which gives an estimate of the effective dose in a tissue at the depth d, in mm, and has the unit Sv. Examples for personal dose equivalents are the whole body dose ($H_\mathrm{p}(10)$), the skin dose ($H_\mathrm{p}(0.07)$) and the eye lens dose ($H_\mathrm{p}(3)$). $d = 10\,\mathrm{mm}$ is taken for example to approximate the whole body dose, because it is assumed that most organs are located in about 10 mm under the skin. Similar the depth of the skin and the eye lens are selected. All these operative quantities give an estimate on the not mensurable protection quantities.
Figure 2.1 shows the connection between the protection quantities (left) and the measurable operative quantities (right).

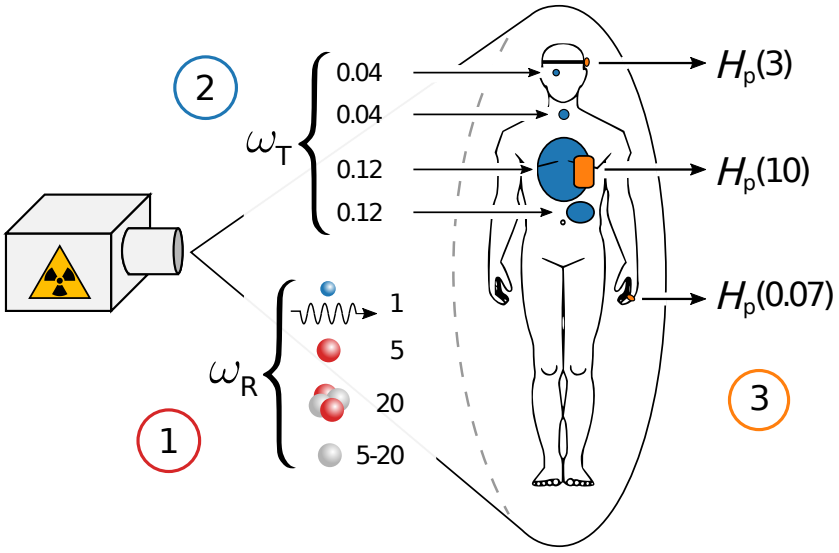

Figure 2.1: Protection quantities and their estimation over operative quantities. 1: Weighting factors for different types of radiation. 2: Weighting factors for different tissues in the human body. 3: Operative quantities. The values of the weighting factors are defined in Ref. [7].

The operative quantities can be calculated via the measurable quantity Kerma (kinetic energy released per unit mass). It is defined as the loss of kinetic energy from secondary

particles per mass in a material. Secondary particles are produced if ionizing radiation interacts with matter. For dosimetry applications the Kerma in air K_a is mainly used, because the handling is very easy.In case of a secondary electron equilibrium the Kerma is equal to the absorbed dose and therefore, it is the main quality of an irradiation field and the other operative quantities can be easily calculated via conversion factors.

2.1.1 Personal dosimetry

According to StrlSchV [5] and RoeV [6], any person who can be occupationally exposed to radiation has to be officially monitored. The official monitoring in Germany is conducted by four individual dose monitoring services, the "Strahlenmessstelle" of the Senate Department for the Environment, Transport and Climate Protection in Berlin, the "Landesanstalt für Personendosimetrie und Strahlenschutzausbildung" (LPS) in Berlin, the individual monitoring service of the Materialprüfungsamt North Rhine-Westphalia (MPA NRW) in Dortmund and the "Auswertestelle" (AWST) of the Helmholz Zentrum Munich, ascending by number of monitored persons.

The dosemeters used for the official individual dosimetry have to fulfill national and international standards [8, 9], e.g. the response of the dosemeter as a function of the irradiation energy and angle has to be in a given range. Furthermore, all monitoring services have to regularly participate in comparison measurements for quality assurance of the European Radiation Dosimetry Group (EURADOS).

The individual monitoring service of the MPA NRW is the second largest measurement facility with approximately 110 000 dosemeter evaluations per month. The main monitoring parameter in radiation protection dosimetry is $H_p(10)$, which is currently done by using film dosemeter which is described in the next section.

2.1.2 The film dosemeter

Film dosemeter consists of a photo-film and if the film gets irradiated it becomes darker. The gray tone of the optical density of the film is directly correlated to the amount of incoming irradiation.

The film itself is very sensitive to the irradiation energy as well as its angle. To achieve the requirements to an official dosemeter, the gliding-shadow method was developed [10]. With a combination of two filters the energy and angular dependency of dosemeter response can be reduced.
One filter consists of several metals and guarantees a good response for higher irradiation energies, whereas the filter made of plastic provides a good response for lower energies.

For the analysis the two gray tones of the film under the two filters are examined and differently weighted to induce an energy independent value so that the overall energy dependency of the film can be compensated. The filters are placed at a certain distance in front of the dosemeter and are designed so that the density of the film is independent of the irradiation angle. Furthermore, the badge contains four lead pins to estimated the direction of incident radiation by analyzing their shadow on the film. Two more filters are added to distinguish between beta- and gamma-irradiation.

After the film is developed, it can be read out in a fully automated setup. The film dosemeter does not loose signal due to thermal fading, which is explained in Section 2.3. However, after its production, the film loses sensitivity due to accumulation of natural radiation and is a single-use detector.

The film dosemeter is currently still the predominantly used dosemeter type in routine dosimetry to monitor the whole body dose $H_{\mathrm{p}}(10)$. However, it loses its approval at the end of 2024 and thus, the dosimetry services are in the process of switching to other types of dosemeters, like thermoluminescence or optically stimulated luminescence. Thermoluminescence dosemeters are already used in various fields of dosimetry, e.g. beta-ring dosemeter to measure the skin dose $H_{\mathrm{p}}(0.07)$.

2.2 Thermoluminescence

The phenomenon of *thermoluminescence* (TL) describes a process in which light is emitted by an irradiated material when it is heated. The phenomenon is utilized in various fields of radiation protection and dating.
This process can be divided into two steps, first the irradiation of the sample, second its light emission during heating. The previous radioactive irradiation is essential to observe the phenomenon, otherwise only black body radiation or incandescence, respectively, occur. Therefore, it is actually more accurate to call the phenomenon *thermally stimulated luminescence*, because the heat is not the exclusive reason but rather the activator for the photon emission, similar to *optically stimulated luminescence* (OSL) where an optical laser stimulates the light output of an irradiated sample. However, the term TL is more commonly used and thus, used in the following.

TL detectors are mainly made of material which are insulator, e.g. lithium fluoride or calcium fluoride. The TL in these solids can be explained with the help of the band-model. The uppermost band, which is completely filled with electron, is the valence band. The electrons in this band are bound to the ions of the lattice. The conduction band is the first band, which is generally empty.
If the sample is irradiated, electrons are exited from the valence band to the conduction

band, where they are unbounded and can move freely before they return to their ground state in the valence band.

However, there is no TL light emission during the return if the irradiated material is pure and have no defects. To be able to undergo the effect of TL, a material needs certain types of defects which are capable of trapping electrons and holes, coming from the interaction of ionizing irradiation with material. Those defects can be inserted by doping the material, e.g. LiF is often doped with magnesium and titanium (LiF:Mg,Ti) to create *traps*. The energy levels of the traps lie between both bands, as shown in Figure 2.2. The binding energy of a charge carrier to a trap is called trap depth.

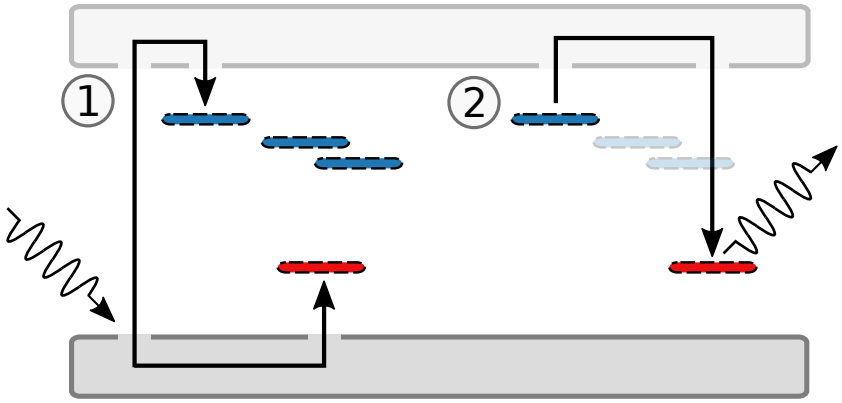

Figure 2.2: Schematic of the band structure in a doped insulator. The traps for electrons (blue) and for holes (red) lie between the valence band (bottom) and the conductive band (top). 1: An electron-hole pair is created and the free charge carriers get trapped in defects. 2: The electron is released from its trap and recombines with an hole under emission of TL light.

If ionizing radiation interacts with a material electron-hole pairs are induced. During this process, the electrons are exited and are able to move freely in the conductive band. The holes are able to move freely in the valence band. On the one hand, they can recombine directly afterwards, which is called radioluminescence. On the other hand, it is possible that the charge carriers get captured in traps, left part of the figure.
Traps which have a higher binding energy compared to other traps are often called *recombination centers*. In the following, it is assumed that electrons are captured in traps and holes in recombination centers. However, also the other way round is possible depending of the material and the doping.

The trapped charge carriers stay in the traps and recombination centers until they have an energy equal or higher than the binding energy E of the trap, e.g. if the sample is heated. The ratio of particles n/n_0 which have an energy of ΔE above their ground state at a given temperature T is given by the Boltzmann function with the Boltzmann

constant k.

$$\frac{n}{n_0} = \mathrm{e}^{-\Delta E/(kT)} \tag{2.2}$$

For typical values of e.g. $\Delta E = 1.2\,\mathrm{eV}$ and $T = 473\,\mathrm{K}$ the fraction n/n_0 is smaller than $1 \cdot 10^{-12}$. However, for such values TL light emission is observed and this is due to an additional factor s, the so-called frequency factor. This factor was introduced in Ref. [2] and describes the rate with which the electrons "try" to escape. It is the product of the frequency with which electron strikes the wall of the potential box of the trap and the reflection coefficient on it. Thus, s also depend on the temperature of the sample, but this dependency is very small and can be neglected in the following.
The probability, p_{release}, that an electron is released from a trap can be described as

$$p_{\mathrm{release}} = s\mathrm{e}^{-\Delta E/(kT)}. \tag{2.3}$$

The value of s is in the range of $(n/n_0)^{-1}$ and thus, the electron is released from the trap if its energy is equal to or higher than the binding energy. Consequently, the higher the temperature the more electrons from deeper traps can be released. For application of TL, the required energy is usually supplied by heating the sample.

During the heating, electrons are excited into the conduction band, from where they can be either recombine with a hole in a recombination center under the emission of TL light (see right part of Figure 2.2) or the electrons can be trapped again either in the same or another trap, called re-trapping.
The simplified *one trap one recombination center* (OTOR) model is often used in literature to describe these processes, e.g. Ref. [2]. As the name of the model states, only one kind of traps with a binding energy of $\Delta E = E$ and one kind of recombination center are considered.

Ref. [2] assumes that in most cases the re-trapping can be neglected and presented Equation (2.4) which describes the intensity I of emitted TL light as a function of time t, where n is the number electrons trapped with an energy of E at the time t and a temperature T. The constant C includes all measurement efficiencies and is set to 1 in the following.

$$I(t) = -\frac{\mathrm{d}n}{\mathrm{d}t} = Cns\mathrm{e}^{-E/(kT)} \tag{2.4}$$

The model, in which re-trapping is neglected, is often referred to as first-order kinetics. In this model the light emission is directly correlated to the excitation of electrons from traps.
If the the amount of re-trapping is equal to that of recombination, the model is referred to as second-order kinetics [11]. Everything in between is summarized in the model of

general-order kinetics [12]. The difference between these models as well as an extension to mixed-order kinetics are discussed in Refs. [13, 14, 15].

Equation (2.4) describes the TL intensity I in the OTOR model for one trap depth. However, usually traps at different depths exist in a doped material and each trap depth results in a separate glow peak. If the superposition of all glow peaks is plotted versus the temperature T or versus the time t it is called glow curve.
Since the number of measured photons is proportional to the number of trapped electrons, which is proportional to the incident irradiation dose, it is possible to use the TL phenomenon for dosimetry. Thus, TL dosemeters are an alternative to the deprecated film dosemeter presented in the previous section. Summaries of the State-of-the-art of TL dosimetry applications can be found in Refs. [16, 17].

In addition to LiF:Mg,Ti, several other materials are suitable for TL dosimetry, e.g. LiF:Mg,Cu,P, CaF_2:Tm or $CaSO_4$:Dy. Information about six commonly used TL materials and their characteristics can be found in Ref. [18] and references therein. The dosemeters, investigated in the following, are produced with LiF:Mg,Ti. As the sensitive TL material, MT-N is used, which is manufactured by Radcard [19].

LiF:Mg,Ti has five significant glow peaks, denoted by P_1 to P_5, in a temperature range between room-temperature and 573 K, which is the readout temperature. The half-lifes of the individual peaks depend of the depth of the trap and range from a few minutes to several years, for more details on the different peaks see next section.
In most practical applications the first peak P_1 vanishes completely due to its very short half-life and thus, only four glow peaks, P_2 to P_5, are taken into account in the analysis presented in the next chapters. A typical glow curve with its individual glow peaks is shown in Figure 2.3

LiF:Mg,Ti can not only be used for TL but also as proton bragg peak [20] or fluorescent nuclear track detectors [21]. Both uses the phenomenon of radiophotoluminescence. This type of luminescence occurs if the irradiated LiF:Mg,Ti sample is subsequently illuminated with blue or ultra-violet light.

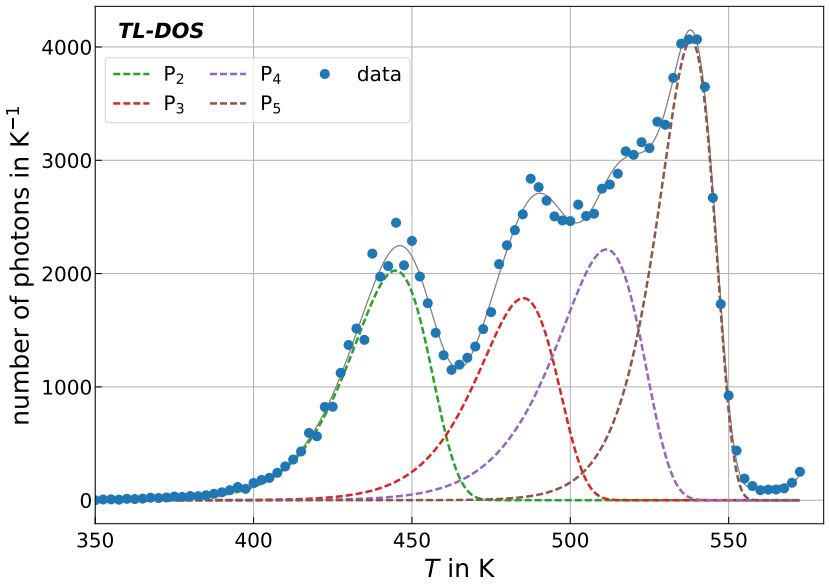

Figure 2.3: Typical glow curve with a dose of $H_p(10) = 15\,\mathrm{mSv}$. The four individual glow peaks are plotted as dashed lines. The gray line which described the whole glow curve is plotted to guide the eye.

2.3 Thermal fading in LiF:Mg,Ti

Trapped charge carriers can be released by applying energy in the form of heat as described in the previous section. Due to Equation (2.3) there is a chance to release electrons from their traps already at room-temperature. This phenomenon is called thermal fading or simply fading.

Consequently, thermal fading results in a smaller TL signal when read out. For example the signal of the used LiF:Mg,Ti dosemeters decreases by up to 30% in a typical routine monitoring cycle of 40 d. The individual peaks are affected in different ways. High-temperature peaks are more stable than low-temperature peaks, because shallow traps can be released more easily by thermal stimulation than traps with higher activation energies.

The fading dependency of the single glow peaks is shown in Fig. 2.4. Each of the five glow curves shown is an averaged over 40 measurements, each irradiated with a dose of $H_p(10) = 10\,\mathrm{mSv}$. The fading time ranges from 0 d to 40 d.
Peak P_2 shows a significant decrease of more than 50% within the first 24 h after irradiation. Afterwards, it decreases slower due to re-trapping and after 10 d it is hard to spot in the glow curve. In contrast, P_3, increases slightly within the first 24 h due to re-trapping processes and only then begins to decrease so that a significant reduction of the peak strength is visible after 40 d. The peaks P_4 and P_5 remain constant in the

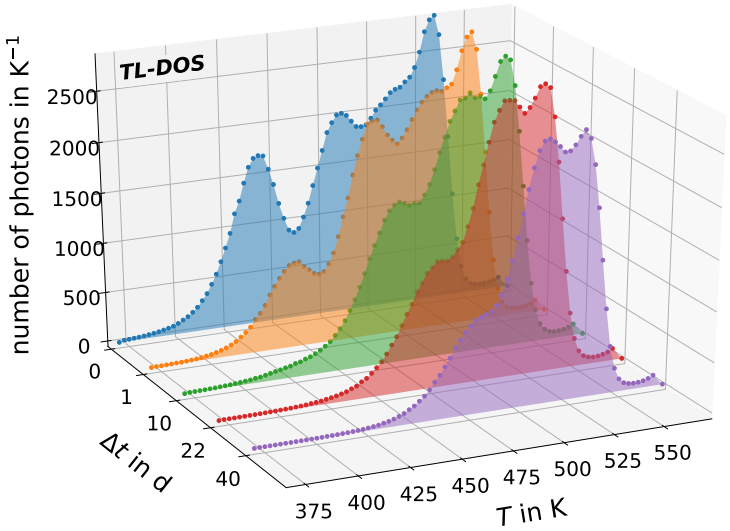

Figure 2.4: Glow curves for different fading times. Each glow curve is an average of several glow curves irradiated with $H_p(10) = 10\,\mathrm{mSv}$. Adapted from Ref. [4].

first days after irradiation. The significant fading of the first peaks and a re-trapping to P_4 ensure a significant increase of more than 10% in peak height of the fourth peak after 10 d. Afterwards, the low-temperature peaks are almost gone and P_4 can not be strongly refilled anymore. Thus, it starts to decrease for longer fading times. However, P_5 remains constant for a longer time after irradiation and only after approximately 40 d a small decrease is visible.

It is difficult to estimate half-lifes of the individual glow peaks from this data due to superposition of two effects, namely fading and re-trapping. This process can result in a slight increase of the TL light of one glow peak. Therefore, the changes of the glow peak heights depending on the fading time are only described qualitatively.

There are several techniques to handle the fading influence during dosimetry. One possibility is to wait some days after the return of the dosemeters until the decrease induced by fading is not so steep and then multiply the number of measured photon by a scaling factor.
Another possibility is to apply a complex annealing procedure on the detectors with which they become less dependent on fading. A more accurate and less time-consuming possibility is to pre-heat the detectors before readout [22, 23].

During the pre-heating process, more electrons from the low-temperature peaks P_2 and P_3 are released compared to those in deeper traps. Both peaks, P_2 and P_3, are sensitive to fading and by depleting those traps the most fading time dependent signal can be erased. Due to re-trapping of some released electrons the TL signal in P_4 and P_5 increases slightly.

Figure 2.5 shows the difference between a pre-heated and a non pre-heated glow curve. Both curves are read out within one hour after irradiation. Although the the peaks most

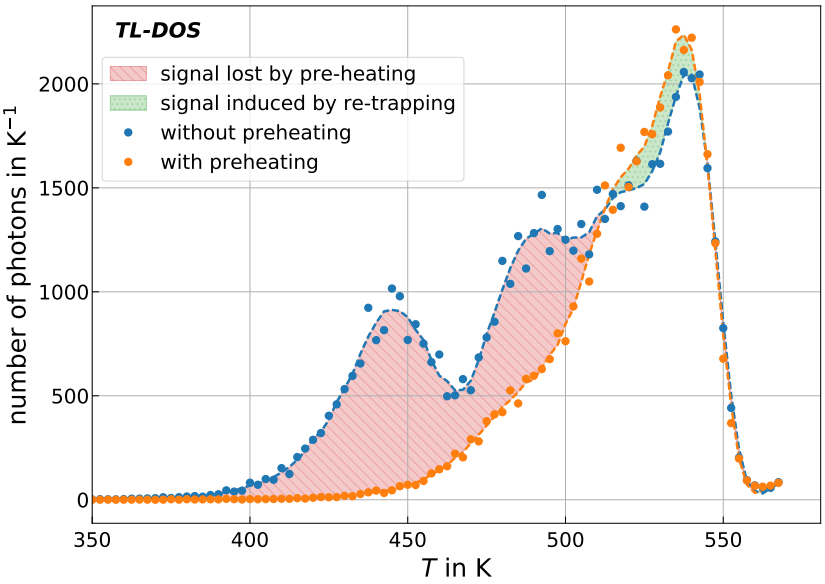

Figure 2.5: Comparison between a glow curve with (orange) and without (blue) pre-heating. The red area indicates the amount of signal and information loss. The green area shows the increase of the TL signal in P_4 and P_5 due to re-trapping.

affected by fading time are depleted, the remaining signal shows still a small dependency on the fading time. However, this amount can be neglected for dosimetry purpose.

The pre-heated glow curve is in fact nearly fading time independent, but a large amount of information gets lost. Therefore, another approach is investigated in this thesis. The fading time will be estimated and then the measured signal can be corrected. Consequently, the detectors used for these studies are not pre-heated.

2.4 The TL-DOS system

The Monitoring Service at the Materialprüfungsamt North Rhine-Westphalia (MPA NRW) is developing a thermoluminescence dosemeter system (TL-DOS) for the application in their routine dosimetry. The system was first introduced in Ref. [22] and includes the detectors, the badge of the dosemeter and the TL reader. The Lehrstuhl Experimentelle Physik IV at the TU Dortmund participates in this project, especially in the development of the automated analysis of the data.

TL-DOS is designed as a multipurpose system to read out whole body as well as partial body dosemeters and also neutron dosemeters.

However, the main focus is on the realization of a whole body TL dosemeter to simultaneously measure the personal dose equivalents $H_p(10)$ and $H_p(0.07)$ according to EN 62387 [9]. In addition, the dosemeters have to fulfill requirements of the Physikalisch-Technische Bundesanstalt (PTB) [8], e.g. the response of the dosemeter as a function of the irradiation energy and angle has to be in a given range. Furthermore $H_p(10)$ dosemeters must not measure more than 10% of the irradiation dose from a beta irradiation. This so-called beta-criterion is required because beta irradiation is not expected to contribute to the effective dose in a depth of 10 mm.

In comparison to a gliding shadow film dosemeter, the TL-DOS dosemeter has several advantages. The sensitive material LiF:Mg,Ti, used for the detectors, is less energy dependent and also tissue equivalent, which slightly simplifies the calibration process. The detector of the TL-DOS dosemeter can be used multiple times because on the one hand it is still sensitive to irradiation after readout and on the other hand it can be reset to the initial state, a process known as annealing. This is done by heating the detector to a temperature of 673 K so that all traps, which are responsible for the glow peaks up to the readout temperature of 573 K, get depleted and the complete information on the detector is erased before the detector is used again. Thus, the detector is not affected by previous irradiations. This process ensures that the detector has the same sensitive for every measurement. Furthermore the complete annealing offers the possibility to calibrate every detector individually. After the readout and the annealing of the detector, it is irradiated with a known dose and subsequent measured to estimate the calibration factor.

A schematic workflow of how measurements are performed with the TL reader is shown in Figure 2.6. During routine dosimetry the received detectors (blue) are pre-heated and subsequently read out. To estimate the irradiation dose, the detectors have to be calibrated (orange). The detectors are annealed, irradiated with a known dose and read out after pre-heating to estimate the calibration factor.

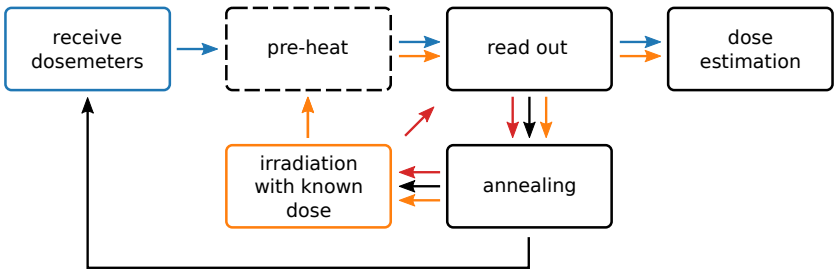

Figure 2.6: Schematic workflow of the measurements of the detectors. The way of the received detectors is shown in blue, the calibration in orange and the way of the detectors for measurements in this thesis in red.

The measurements in this thesis (red) are performed with out the pre-heating process.

A disadvantage compared to the film dosemeter is that the LiF:Mg,Ti material shows thermal fading, as described above. However, there are several techniques to overcome the effect of fading, see Section 2.3. In addition this phenomenon can be used to estimate the date of an irradiation, which is the main focus in this thesis. Furthermore, the glow curve can be analyzed to get additional information to the irradiation dose.

2.4.1 Detectors

The detectors of the TL-DOS system are developed, produced and tested at the MPA NRW. There are several detectors sizes for different dosemeters types, which are very similar in composition.
The composition of a detector as used in the whole body dosemeter, is shown in Figure 2.7. The sensitive TL material is placed together with a reflective layer and ceramics on a carrier plate consisting of aluminum. The carrier is then placed inside a holder frame, the so-called code ring.

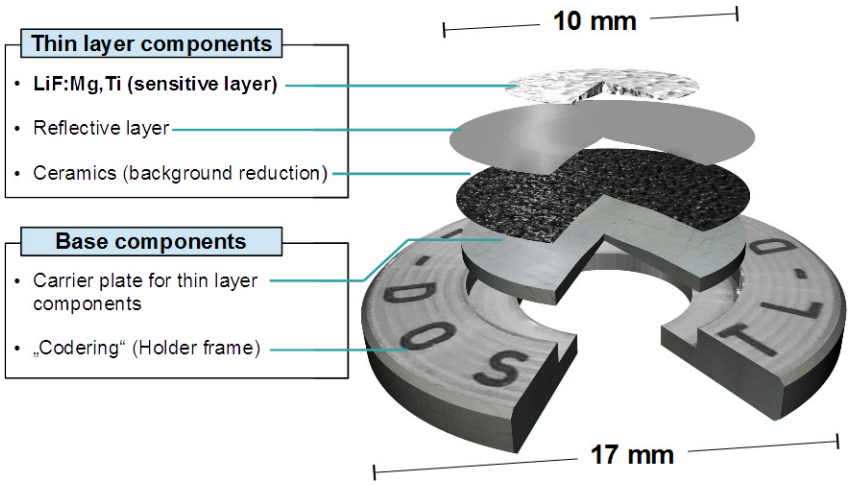

Figure 2.7: The detector of the TL-DOS whole body dosemeter consists of thin layer components, including the sensitive material LiF:Mg,Ti, and components such as a carrier plate and a code ring. [3]

During production of the detector, first the ceramics is deposited on an aluminum plate using flame spraying method. The ceramics reduces black body radiation of the aluminum during the readout and thus, the non-radiation induced signal is reduced, which increases the sensitivity.
The reflective layer was added in an early development stage to amplify the TL signal and to increase the sensitivity. However, investigations, presented in Chapter 5.1.2, show no significant effect of the reflective layer for the newer detectors anymore and as a

consequence it is omitted. By omitting the additional step during the production process, the production time of the detector can be reduced.

The sensitive TL material is MT-N. It is manufactured by Radcard [19] and has a natural composition of ^{6}LiF:Mg,Ti (∼5%) and ^{7}LiF:Mg,Ti (∼95%). The LiF:Mg,Ti powder is hot-sintered on the ceramics of the aluminum carrier plate. The amount of LiF:Mg,Ti can be adjusted between 1 mg and 35 mg. For the standard detector of the TL-DOS whole body dosemeter 15 mg are used, whereas the amount of LiF:Mg,Ti on a detector for partial body dosemeters ranges from 1 mg to 5 mg to adjust the sensitivity of the detector to the different required irradiation dose ranges.

The size of the aluminum carrier plate itself depends on the detector type as well. The carrier plate of a standard detector is 10 mm in diameter and the smaller detectors, used mainly for partial body dosemeters, have a diameter of 7 mm. On the bottom side of the detector a data matrix, containing the detector identification number, is engraved with a laser.

The aluminum code ring provides protection of the inner core and includes the detector identification number in a human readable form. However, it is only used for the 10 mm detectors. To read out the smaller 7 mm detectors with the same reader, an adapter similar to the code ring is used.

More information about the detectors used for the studies in this thesis, can be found in Chapter 5.1.

2.4.2 Dosemeter system

The badge for the dosemeter of the TL-DOS system was mainly developed in Refs. [24, 25] and is shown in Figure 2.8. The dosemeter consists of two detectors, one measures the personal dose equivalent $H_{\mathrm{p}}(10)$ and one the $H_{\mathrm{p}}(0.07)$ quality according to the international standards [9]. For the routine monitoring at the MPA NRW only the $H_{\mathrm{p}}(10)$ value is used, whereas the $H_{\mathrm{p}}(0.07)$ detector works as a backup. The badge has a size of 65 mm × 40 mm × 4 mm.

A filter is placed in front of one detector to measure the personal dose equivalent $H_{\mathrm{p}}(10)$. To estimate a suitable filter material as well as thickness, several combinations are investigated in Refs. [24, 25].
It was found that a polytetrafluoroethylene (PTFE) filter with a thickness of 4 mm provides the best results. However, the filter was optimized in Ref. [26] with respect to convenience and the current version of the filter in the badge is 2 mm thick. Even with the thinner filter it can be guaranteed that the $H_{\mathrm{p}}(10)$ detector does not measure more

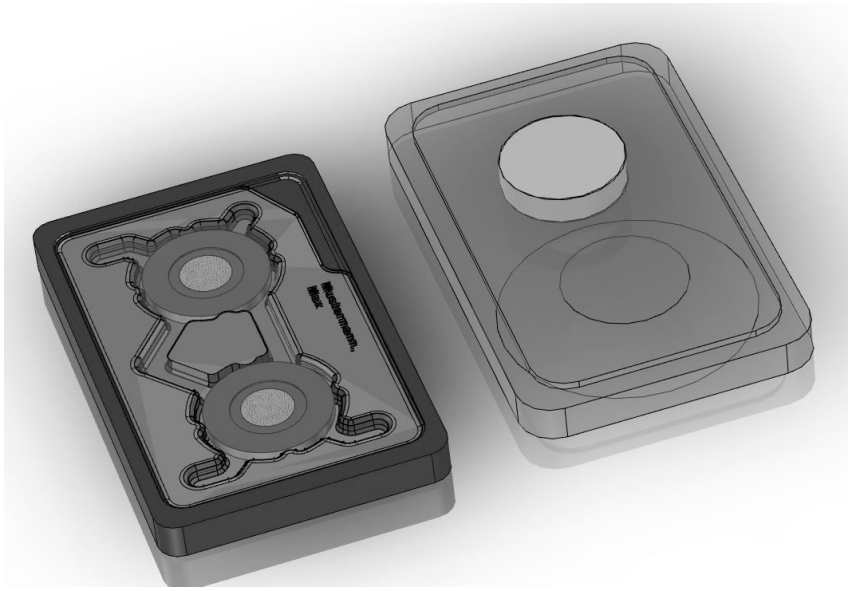

Figure 2.8: Drawing of the dosemeter badge with two TL detectors, one measures the $H_p(10)$ irradiation dose quality and one the $H_p(0.07)$ quality. Left: Blister pack containing the two detectors. Right: Enclosure with the PTFE filter (top) in front of the $H_p(10)$ detector and a cone shaped gap (bottom) in front of the $H_p(0.07)$ detector. [25]

than 10% of the irradiated dose from a beta irradiation and the beta-criteria is fulfilled. In addition the filter flattens the dependency of dosemeter on the irradiation energy and the irradiation.
In front of the other detector no additional filter is positioned and only the thin plastic layer of the badge material provides filtering to measure the $H_p(0.07)$ quality. A cone shaped recess with an opening angle of 60° in front of the $H_p(0.07)$ detector guarantees a flat angle response for it as well.

In addition to the whole body dosemeter with two detectors, several other dosemeters are investigated. A finger ring dosemeter to measure the partial skin dose $H_p(0.07)$ using the small detector elements was developed in Refs. [27, 28]. The smaller detectors were also used to design an $H_p(3)$ eye lens dosemeters and demonstrate its practicability [29]. Furthermore, in Refs. [30, 31] first studies for the development of a neutron dosemeter based on the TL-DOS system are performed. For this purpose detectors with pure ^{6}LiF:Mg,Ti and others with pure ^{7}LiF:Mg,Ti are produced and combined in one dosemeter.

2.4.3 TL reader

The measurements presented in Chapter 4 are performed with the so-called Prototype II TL reader [22]. It is designed for application in routine dosimetry and consists of different

independent modules. Since these measurements, a new TL reader has been delivered. It is design to be used in large-scale routine dosimetry and have a higher throughput compared to the Prototype II. However, it is not used for measurements performed in this thesis and thus, it is not introduced here, but details and first investigations on the new reader can be found in Ref. [26].

Figure 2.9 shows the Prototype II of the TL-DOS reader with its different modules (A-F) for pre-heating, readout and annealing arranged in a circle around the transportation unit.

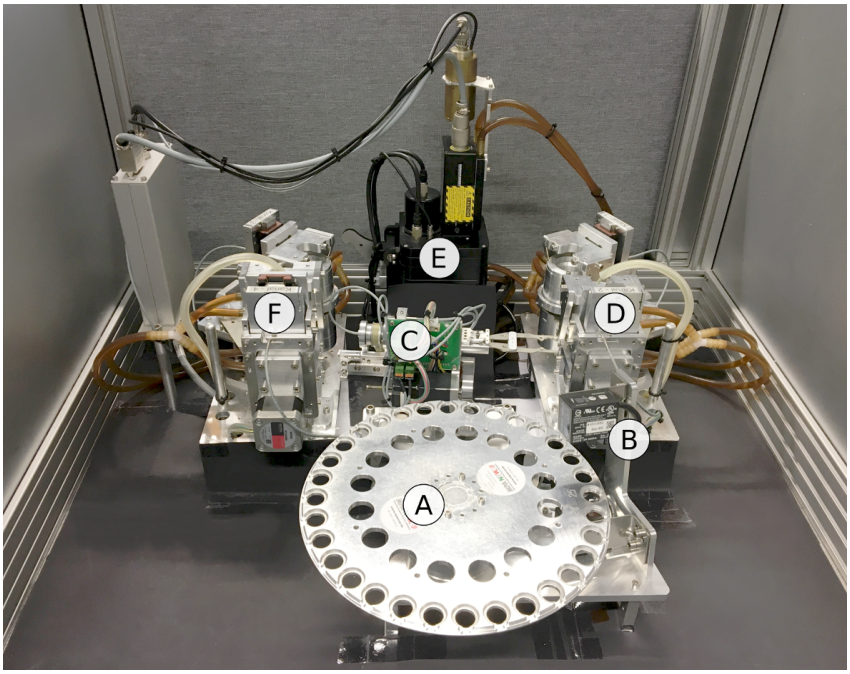

Figure 2.9: Prototype II of the TL reader for the TL-DOS system. A: Holder for 32 detectors, B: Scanner to read data matrix, C: Transportation unit, D: Pre-heating station, E: Measurement chamber with PMT, F: Annealing station.

Detectors can be placed in a holder wheel with 32 slots (A). The scanner (B), which is mounted next to the holder, reads the data matrix with the detector identification number to guarantee an accurate and fast identification of the placed detectors. The transportation unit (C) is arranged in the middle to effectively handle the detectors between the three heating stations and the holder wheel.

To overcome the effect of fading, the detectors can be pre-heated before the readout [22, 23]. In the pre-heat station (D), the detectors are placed on a constant-temperature cartridge and are heated up for 10 s to 428 K. Afterwards, they are cooled down to room-temperature for 3 s and read out subsequently. Since the fading time is analyzed in this thesis and pre-heating erases nearly all information about it, the pre-heating device is not

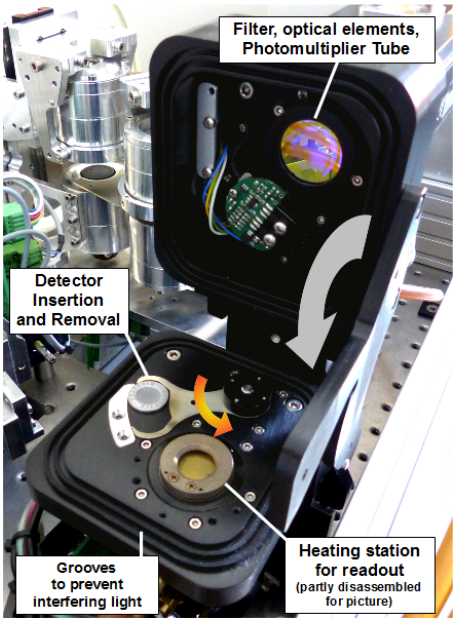

Figure 2.10: Readout unit with measurement chamber consisting of a constant-temperature cartridge and a PMT. Adapted from Ref. [22].

used here. However, it is very important for routine dosimetry because it allows a much easier calibration. If the detectors are pre-heated, the calibration measurements can be read out directly after their irradiation. Otherwise they would have to be stored until they show a similar fading as the monitoring measurements from the received detectors.

The key component of the reader is the readout unit (E) which is also shown in Figure 2.10. The measurement chamber consists of a constant-temperature cartridge and a photo multiplier tube (PMT). The heating plate has a constant temperature of 573 K and the resulting exponential heating of the detector allows to obtain a glow curve in about 10 s. For application in routine dosimetry, the TL signal is recorded for 12 s to 15 s. The PMT has a sampling frequency of 10 ms and is able to count single photon and simultaneously measure the photo current. The single photon mode yields accurate glow curves for low irradiation dose, which are typical for routine dosimetry. For irradiation doses higher than approximately 100 mSv the single photon mode is not reliable due to an overflow of photons and the information from the photon current mode has to be used for analysis. The exact threshold is investigated in Ref. [32].

During the development of the reader, the main focus was on reaching high sensitivity to low irradiation doses. Therefore, the PMT is placed very closed to the detector which leaves no space to include a sensor to measure the temperature of the detector during heating.
The sensitivity is also increased by reducing the non-radiation induced signal. This background stems from three different sources, namely thermal radiation, radiation related to chemiluminescence effects and the instrumental background [33].
The instrumental background is e.g. induced by the dark current of the PMT. It is

minimized by cooling the PMT and optimizing the threshold of PMT which was done by manufacturer of the reader. The thermal radiation is emitted by the detector during heating and the heating plate itself. Using appropriate optical filters can reduce the amount of black body radiation detected by the PMT.
The signal related to chemiluminescence effects can be suppressed by flushing the measurement chamber with nitrogen. With these arrangements the non-radiation induced signal can be significantly reduced but not completely canceled and thus, it is considered in the glow curve deconvolution (GCD) of the glow curve as described in Chapter 3.

The annealing station (F) is identical in construction to the pre-heat station. However, the heating element for annealing of the detectors has a constant temperature of 673 K. The detector is heated up to this temperature for 15 s and is then cooled down to room-temperature in another 15 s. The high temperature gradient results in a high sensitivity of the LiF:Mg,Ti material [34]. During this process all traps get depleted and the detector is reset to its initial state and thus, it can be reused for dosimetry purpose.

The TL reader is designed to reach a very low detection limit and to have a high throughput. All stations for pre-heating, readout and annealing are in one device and no time-consuming transportation between different devices has to be realized. In addition, all heating stations use constant-temperature cartridges resulting in a fast exponential heating of the detectors and thus, the reader has a high throughput. The lower detection limit of 100 µSv, requested by the PTB [8], can easily be reached as calculations show in Ref. [35].

2.4.4 Evaluation and analysis software

For the analysis presented in this thesis, multiple custom-made software packages are written in Python using several open-source packages. Most algorithms and calculations in the temperature reconstruction and GCD, described in Chapter 3, including the fitting procedures are implemented by using functions from the SciPy library [36].

With the custom-made software package, glow curves are automatically imported, the temperature is reconstruction and a GCD is performed. The results are saved in *DataFrames* of the pandas library [37], which can be exported to many different types of output files. This software package allows to perform a complete analysis including calibration and irradiation dose estimation. Furthermore, all corrections presented in Chapter 5 are included as well and can be applied during an analysis.

The machine learning which is presented in Chapter 7 is also included in the software package and uses the scikit-learn library [38]. For visualization and plotting the open-source packages Matplotlib [39] and Seaborn [40] are used.

Chapter 3

Glow curve modeling and fitting

A thermoluminescence (TL) glow curve typically consists of several glow peaks. Ref. [2] introduced the first-oder kinetics model of Equation (2.4) which describes the TL intensity I of a single glow peak, as presented above. By assuming a linear heating profile, $T(t) = T_0 + \beta t$, and integrating the TL intensity with respect to the temperature T, Equation (2.4) becomes

$$I(T) = s \cdot n_0 \cdot \mathrm{e}^{-\frac{E}{kT}} \cdot \exp\left(-\frac{s}{\beta}\int_{T_0}^{T} \mathrm{e}^{-\frac{E}{kT'}}\,\mathrm{d}T'\right). \tag{3.1}$$

E represents the activation energy of the glow peak, s is the so-called frequency factor, n_0 is the initial concentration of trapped charge carriers and k is the Boltzmann constant. The heating of the TL material from an initial temperature T_0 is described by the heating rate β.

3.1 Transformation from time to temperature scale

The emitted TL intensity of the heated sample depends on the temperature T, as described in Equation (3.1). Due to sensitivity issues, the current TL-DOS reader does not allow to measure the temperature T and instead the glow curve is recorded as a function of time t during the readout. Thus, a transformation from time to temperature scale is used to offer the possibility of a glow curve deconvolution (GCD). Since this technique was describe in Ref. [3, 4], some improvements have been made.

To read out the detectors, they are placed on a constant-temperature cartridge with a heating temperature T_{heat} of 573 K, as described in Chapter 2.4.3. This results in an exponential heating of the detector $T(t)$, see e.g. Ref. [41],

$$T(t) = T_{\mathrm{heat}} - (T_{\mathrm{heat}} - T_{\mathrm{start}}) \cdot \mathrm{e}^{-\alpha t}, \tag{3.2}$$

where T_{start} is the temperature of the detector at the beginning of the measurement and α is the exponential heating parameter which depends on the heat transfer between the heating cartridge and the detector.

The model shown in Equation (3.2) does not consider additional effects like radiative cooling or the temporary temperature decrease of the heating plates directly at the beginning of the measurement due to the placing of a cold detector on the contact heating supply.
The influences of several cooling effects are investigated for example in Refs. [42, 43]. Both developed a generalized model by adding additional terms of cooling and heat transfer inside the detector to describe the real heating as accurately as possible. The information about the exact heating profile is either used to fine-tune the gas temperature of their reader or to adjust the set heating profile.

However, the heating profile is only used to convert the glow curves from time to temperature domain, thus the basic detector temperature model is sufficient. A more sophisticated heating function with additional parameters would even result in an under-estimated fit-procedure, which is described below.

Due to slightly different heat transfer between heating plate, detector and the sensitive material, the exact temperature profile differs for each readout. These differences arise from fabrication tolerances and the usage of contact heating, resulting in glow curves with variable length in the time domain, see the left part of Figure 3.2. Therefore, it is not possible to use one global function to transform the glow curves from the time to the temperature domain. Instead, a transformation is calculated for every single glow curve, based on their individual heating function, as describe in the following.

The reconstruction can be done with the custom-made software package introduced in Chapter 2.4.4. First, the region of the total recorded glow curve, where the glow peaks arise, is estimated, the so-called region of interest (RoI). In dosimetry this region is sometimes called region of dosimetric interest. The glow curve is highly smoothed with a Savitzky-Golay filter [44] so that the single glow peaks are combined in one broad peak. From the maximum of this one peak the boarders of the RoI are estimated by searching for a given threshold on the TL intensity.

For the transformation from time to temperature domain, the number of individual glow peaks have to be known. If the number is known, e.g. due to known fading time, it can be used directly for the estimation of the peak positions. Otherwise, the number of peaks have to be estimated. This can be done by calculating the second derivative of the glow curve using the Savitzky-Golay filter and count the number of zero-crossings or rather the number of inflection points to determine the number of peaks.This method works quit well for typical glow curves. However, it is difficult to estimate the number of peaks for

glow curves shorter than 6 s via the second derivative because the single peaks can not be distinguished anymore. This could be circumvented if a PMT with a higher sampling rate would be used.

Once the number of peaks is known, the positions of the individual glow peaks are estimated by fitting a superposition of multiple Gaussian functions to the glow curve, see Figure 3.1. The number of Gaussian functions corresponds to the number of peaks in the glow curve. Indeed, the glow peaks are no Gaussian function, but their shapes are similar and the mean values of the Gaussian functions correspond to the peak positions. Furthermore, the approximation is only used to describe the position of the four peaks in time and not to investigate the single peak contents. The temperatures at which the

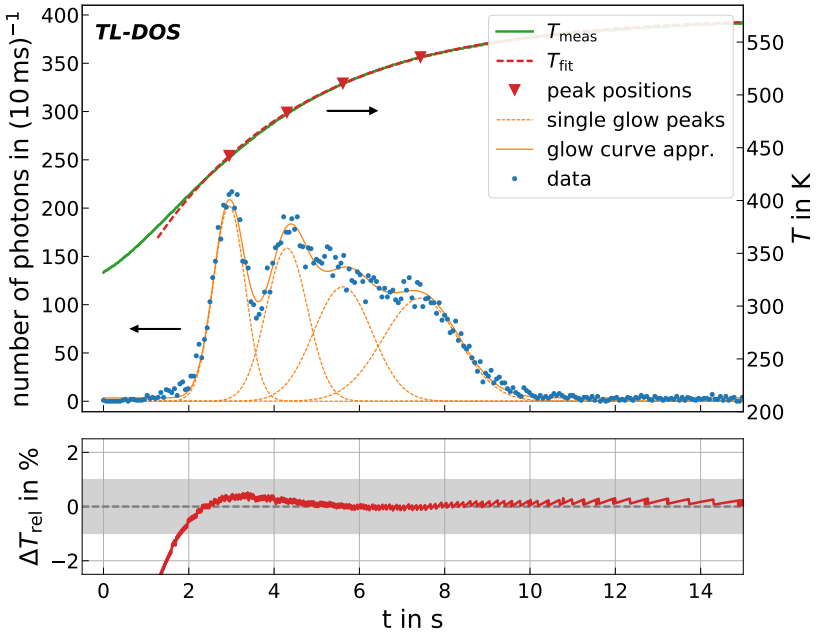

Figure 3.1: Top: Estimation technique of the individual heating function for a given glow curve. The peak positions are estimated by the mean values of Gaussian functions. Afterwards the estimated peak positions in time are plotted versus the known positions in temperature domain and the heating function is adapted to the points. Bottom: Difference between the estimated heating function and the measured heating profile.

individual glow peaks occur are estimated from measurements performed in a previous study with a temperature sensitive setup [45]. This allows to plot the positions of the individual glow peaks in time t_{peak} versus the known peak temperatures T_{meas} and adapt the heating function of Equation (3.2) to the points (t_{peak}, T_{meas}), see upper part of Figure 3.1. The heating temperature T_{heat} is 573 K, whereas T_{start} and α are free parameters to fit.

The deviations between the real and the reconstructed heating function are shown in the

bottom part of Figure 3.1. Due to the aforementioned initial decrease of the temperature of the heating plate due to the cold detector which is not described by the ideal heating profile of Equation (3.2), it may happen that T_{start} is lower than actual room-temperature. However, this apparent deviation between the real and the reconstructed heating function only occurs at the beginning of heating before the start of the RoI.

By using the individually fitted heating functions, every glow curve can be transformed with its own heating profile from time to temperature scale. While the different glow curves have variable length in the time domain due to small fabrication tolerances and the usage of contact heating (left part of Fig. 3.2), the converted glow curves lie on top each other in the temperature domain (right part of Fig. 3.2).

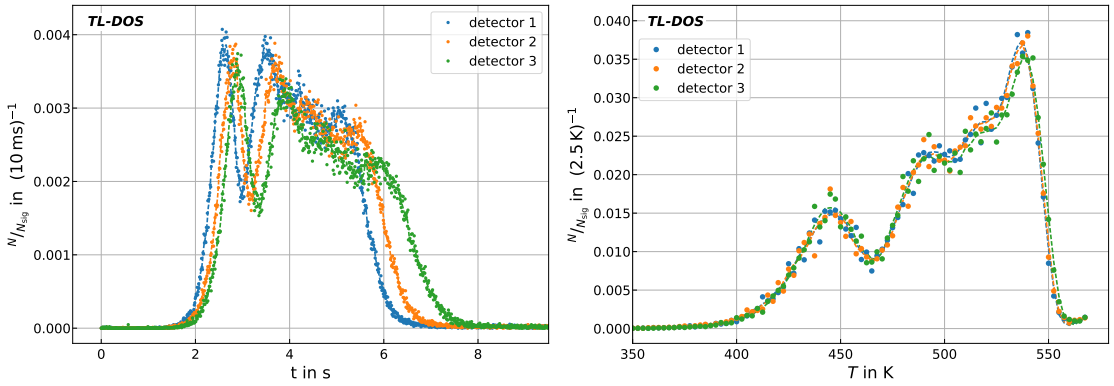

Figure 3.2: Glow curves of different detectors in the time (left) and temperature domain (right). The glow curves in the time domain have a variable length and differ from each other, whereas the same glow curves lie on top of each other after the transformation to the temperature scale. The dashed lines are inserted to guide the eye.

Since the detectors show slightly different responses, for explanation see Chapter 5.1, the shown glow curves are normalized to their total number of photon counts to be able to compare the shapes more easily.

As shown in the bottom part of Figure 3.1, the deviation between the real and the reconstructed heating function is less than 1% in the region of the occurring glow peaks, see bottom part of Figure 3.1. Thus, the deviations can be neglected and the transformed glow curve can be used for further analysis.

3.2 Models used for glow curve deconvolution

After the transformation of the measured glow curve to the temperature domain, a glow curve deconvolution (GCD) can be applied to separate the individual glow peaks. A

superposition of four peaks and a theoretically motivated empirical background function is adapted to the glow curve to obtain information about the individual peaks.

3.2.1 Glow curve model

The glow curve model of Equation (3.1) contains an exponential integral $\int_{T_0}^{T} \mathrm{e}^{-\frac{E}{kT'}} \mathrm{d}T'$ that has no analytic solution (see e.g. Ref. [46]).

To calculate the TL intensity, the exponential integral can be computed numerically. However, a numerical integration is time consuming, especially during a minimization procedure. Therefore, different approximations were developed and described over time. An intercomparison of different models in Refs. [47, 48] reveals partly large deviations between Equation (3.1) and some of theses approximations, resulting in an ineffective GCD. An alternative to these not so suitable approximations is presented in Ref. [46], which describes the glow curve very well and provides a reliable GCD.
Furthermore, it was also tried to use well-established statistic functions like the Weibull distribution or the Logistic asymmetric distribution to describe a single TL glow peak [49, 50]. However, both distributions have an additional parameter with respect to the other functions and are thus more difficult to minimize during the GCD fit.

In contrast to the linear heating assumed in Equation (3.1), the current TL-DOS reader has a constant-temperature cartridge resulting in an exponential heating of the detectors. The heating rate β of an exponential heating profile can be described as

$$\beta = \frac{\mathrm{d}T}{\mathrm{d}t} = \alpha(T_{\mathrm{heat}} - T), \tag{3.3}$$

where α is the exponential heating factor and T_{heat} the constant temperature of the heating plates. With Equation (3.3), the Equation (3.1) can be transformed to

$$I(T) = s \cdot n_0 \cdot \mathrm{e}^{-\frac{E}{kT}} \cdot \exp\left(-\frac{s}{\alpha}\int_{T_0}^{T} \frac{\mathrm{e}^{-\frac{E}{kT'}}}{T_{\mathrm{heat}} - T'}\mathrm{d}T'\right). \tag{3.4}$$

By using the approximation presented in Refs. [51, 52], the TL intensity I in Equation (3.4) can be transformed from $I(T, n_0, s, E)$ to $I(T, I_{\mathrm{m}}, T_{\mathrm{m}}, E)$ to guarantee an effective GCD. The parameter I_{m} describes the intensity of glow peak maximum and T_{m} its position in the temperature domain, comparable to the same parameters in Ref. [46].
The shape of a glow peak is described by three parameters I_{m}, T_{m} and E, which has the advantage that it is possible to directly estimate I_{m} and T_{m} experimentally for a single glow peak before the actual GCD fit. However, it should be noted that E now represents an effective trap depth and no longer the actual activation energy of the glow peak.

In Refs. [51, 52] the exponential integral in Equation (3.4) is approximated by asymptotic series as well as convergent series. A comparison between the numerical integral of Equation (3.4) and the integral of the approximation in Refs. [51, 52] shows a deviation less than 0.001%.

Both, Equation (3.1) and Equation (3.4) describe the TL intensity $I(T)$ of one single glow peak as a function of temperature. However, the glow curves of common TL materials e.g. LiF:Mg,Ti contain multiple glow peaks, see Chapter 2.2 and thus, a superposition of four times Equation (3.4) is used to describe the TL intensity of a complete glow curve.

3.2.2 Background model

In addition to the different glow peaks, the measured glow curve contains non-radiation induced signal. This background stems from three different sources which can be divided into a temperature independent and a temperature dependent part, see e.g. Ref. [42, 33]. The instrumental background is temperature independent and is mostly induced by the dark current of the PMT. The thermal radiation can be divided in a temperature independent part which is caused by the constant-temperature heating element and the warm walls of the measurement chamber and a temperature dependent fraction which is emitted by the detector during heating. The third part of the background contribution is the temperature dependent radiation related to chemiluminescence effects.

During the conceptual design of the reader, different arrangements, which are explained in Chapter 2.4.3, were made to reduce the background effects. However, the non-radiation induced signal can not be completely canceled and thus, it has to be considered in a GCD.

The background can be approximated by a constant plus an exponential term, $I_{\mathrm{bg;\,lit}}$, as e.g. in Refs. [53, 54] for a readout with linear heating or e.g. in Ref. [55] for a readout with an exponential heating. The constant describes the temperature independent part of the background and the exponential term combines all temperature dependent contributions.

Compared to the references, a linear term is added to improve the agreement with the measured background. These empirical investigations lead to a background model of

$$I_{\mathrm{bg;\,lin}} = a + b \cdot T + c \cdot \mathrm{e}^{d \cdot T}, \tag{3.5}$$

where a, b, c and d are free fit parameters and T the temperature of the detector during readout. Equation (3.5) describes background for most parts of the glow curve very well and thus, it is used for the analysis presented in Section 6 to model the background of

the TL-DOS system.
However, a small deviation between the measured glow curve and the fitted function is visible at higher temperatures after the glow peak P_5, at about 560 K. Since the deviation is similar for every glow curve, the influence of the difference at higher temperatures is marginal as long as the GCD is used for peak separation to get information about the single peak contents and no evaluation of kinetic parameters is done.

Equation (3.5) is optimized to improve the consistency between the measured glow curve and the fitted function at higher temperatures as well. The glow curve is recorded as a function of time and thus, the temperature independent part of the background, like the noise of the PMT during readout, is constant in the recorded glow curve. This constant term is transformed to $\propto 1/T$ during the conversion from time to temperature scale.
The temperature, and thus time, dependent part of the background is related to the Planck equation which describes the spectral radiance of a body as a function of the temperature T and the wavelength λ

$$B_\lambda(\lambda, T) = \frac{2hc^2}{\lambda^5} \frac{1}{\mathrm{e}^{hc/(\lambda k_\mathrm{B} T)} - 1}, \tag{3.6}$$

where k is the Boltzmann constant, h is the Planck constant, and c is the speed of light in the medium. The equation to describe the black body radiation is integrated over all occurring wavelengths resulting in a term $\propto T^3 \cdot \mathrm{e}^{1/T}$, see Ref. [42]. Since the emitted intensity is binned in temperature, empirical investigations show that the temperature dependent part of the background can be approximated by an exponential function $\propto \mathrm{e}^T$ [56] as shown in Figure 3.3.

The function to describe the non-radiation induced signal, I_bg, is a superposition of the temperature independent and the temperature dependent part of the background and can be parameterized as

$$I_{\mathrm{bg;\ reci}} = \frac{a}{b - T} + c \cdot \mathrm{e}^{d \cdot T}, \tag{3.7}$$

where a, b, c and d are free fit parameters and T the temperature of the detector during readout.

Figure 3.3 shows the comparison between the different background models as well as the deviation of those to a simulated background, $I_{\mathrm{bg;\ sim}}$. The number of photons are normalized to the maximum value of the simulated data, because the shapes of the different models are compared.
To estimate the simulated background the Planck equation is integrated with respect to the wavelength sensitivity of the reader and a constant background, which is transformed from time to temperature domain, is added. It is clearly visible that $I_{\mathrm{bg;\ lin}}$ shows smaller

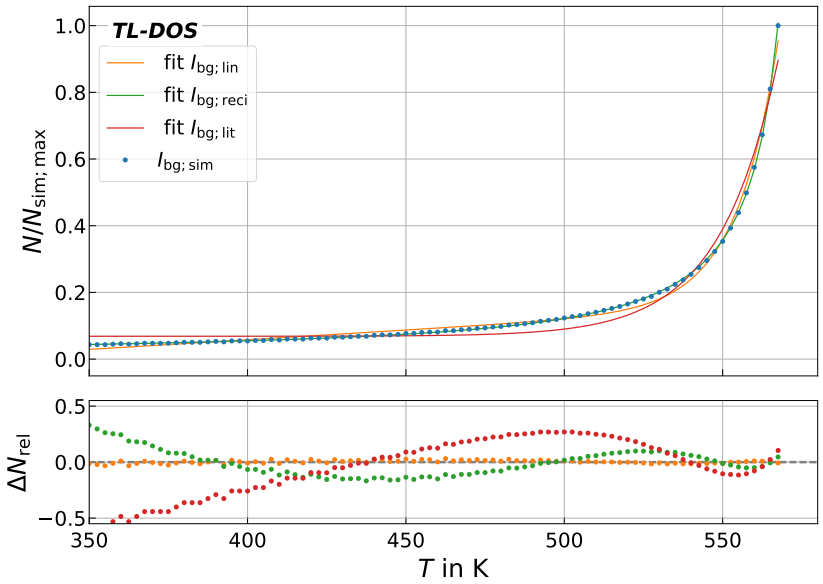

Figure 3.3: Comparison between different background models. Top: Three different background models and the simulated background. The number of photons is normalized to the maximum counts. Bottom: Deviation between the three background models and the simulated background.

deviation to the simulated background compared to the background model $I_{\mathrm{bg;\,lit}}$. The smallest deviations occur between $I_{\mathrm{bg;\,reci}}$ and $I_{\mathrm{bg;\,sim}}$. Thus, this model is used in the GCD which is the basis for analysis in Chapter 5 and Chapter 7.

The background model does not consider a contribution of high-temperature glow peaks above 573 K. For the analysis presented in this thesis, such a contribution arising e.g. from previous irradiations can be neglected due to the high annealing temperature of 673 K. Furthermore, only gamma-sources or x-rays are used to irradiate the detectors which are not expected to excite glow peaks at temperatures higher than 573 K significantly.
However, it appears that for an irradiation with a beta-source, which has a maximum energy of about 2.3 MeV, and especially for alpha- and neutron-irradiations one or more high-temperature glow peaks contributes to the glow curve [57, 31], and have to be considered in the GCD.

3.3 Application of glow curve deconvolution

The fully automated application of GCD to every glow curve is realized by a custom-made software package, see Chapter (2.4.4), which is described in parts in Ref. [4] and is developed in cooperation with Ref. [56].

To separate the single glow peaks, the recorded glow curve is transformed to the temperature domain first by using three or four peaks depending on the glow curve as described in Section 3.1.
Afterwards a superposition of four glow peaks, described by the approximation of Equation (3.4) and the background model, described by Equation (3.7) is adapted to the glow curve. The fit function consists of 16 parameters, three for each of the four glow peaks and four additional ones to describe the background.

In many publications I_m and T_m are estimated before the actual fitting procedure. If the glow curve consists of only a single glow peak the estimation of the peak height and position is easily possible. However, for a multi-peak glow curve with overlapping glow peaks such an estimation does not provide reliable results and thus, those are left free to vary in the fit procedure.
To stabilize the fit with 16 free parameters, a pre-fit is performed using the simplified model of Ref. [46] to estimate start-values for I_m, T_m and E. This approximation assumes a linear heating profile, but it is a fast and very effective possibility to estimate approximate start-values for the GCD. The pre-fit itself uses the previously measured peak temperatures as initial values.

Figure 3.4 shows a measured glow curve with its GCD. The deviations between the measured glow curve and the fitted function are shown in the lower part of the figure. The gray $\pm 5\%$ band is plotted to give an estimate of the deviation between the fit and the measured data. Between 400 K and 550 K no systematic deviations are visible. For temperatures lower than 400 K the fit lies below the measured data and for temperatures higher than 550 K the deviation shows also a systematic. Both imply that the background is not yet described completely with Equation (3.7). However, compared to the total number of measured photons the deviations can be neglected.

The GCD is performed on all glow curve used in this thesis. The main data set, containing the fading, reference and calibration measurements, consists of more than 2700 glow curves and is described in the following chapter.

To assess the agreement of the entire fit function to the data points, the χ^2 is calculated and normalized to the degrees of freedom dof, which is the so-called reduced χ^2. Fits which find no best parameters and do not convergent as well as GCDs with a reduced χ^2 of higher than 10 clearly failed and thus, are not considered in further analysis.
However, based only on reduced χ^2, it is difficult to assess the peak separation strength because no conclusion about the individual peaks can be made. For example, by fitting more peaks to a glow curve than it actually contains, a good agreement between the entire fitted function and the measured data can be achieved, although the fit provides incorrect results about the single peak contents.

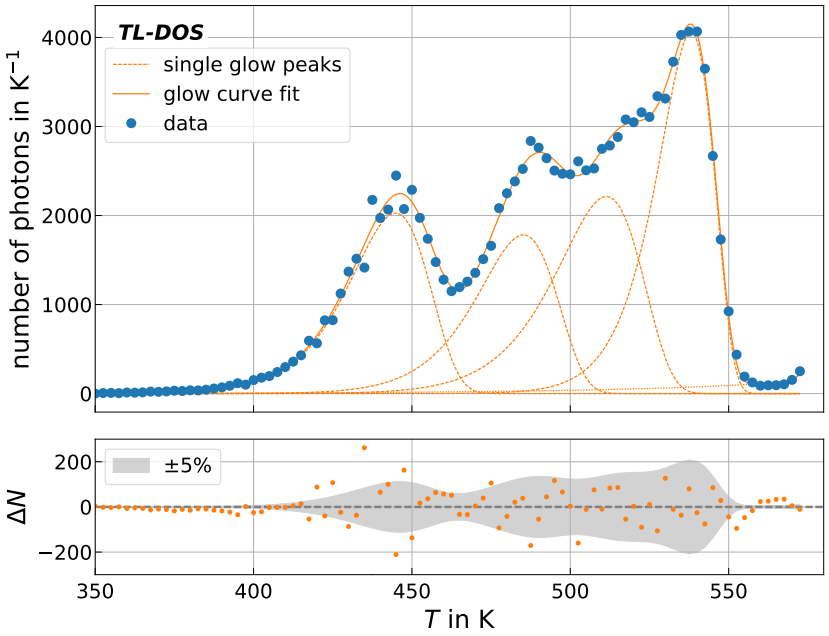

Figure 3.4: Measured glow curve (blue) with the separation in the individual glow peaks (orange). The deviations between the measured data and the GCD are shown at the bottom. The gray ±5% band is plotted to guide the eye and give an estimate of the deviation between the fit and the measured data.

To nevertheless identify failed peak separations, an inter quartile range (IQR) outlier detection is used. It is assumed that the majority of the fits provides a correct peak separation and that only a few peak separations fail. The IQR is the distance between the 25th percentile, Q_1, and the 75th percentile, Q_3. It is assumed that the parameters resulting from the GCD are normally distributed and show no skewness for the same irradiation and readout scenario.
In an IQR outlier detection, usually values which are lower than $Q_1 - 1.5 \cdot \text{IQR}$ and those which are higher than $Q_3 + 1.5 \cdot \text{IQR}$ are determined as outliers. For the studies in this thesis, an outlier criterion of $\pm 3 \cdot \text{IQR}$ is used to only identify extreme outliers. Only the results from reliable peak separation are used for further investigations.

Overall it is noted that the GCD provides reliable results for glow curves which are longer than 5 s. For shorter glow curves a peak separation is challenging and more fits fail or provide no reliable results.

Chapter 4

Measurements and data sets

The majority of investigations presented in this thesis are based on the same data sets as described in Ref. [4]. For the fading studies and the calibration measurements 800 newly produced detectors are used. Furthermore, a set of 22 detectors is provided as a reference sample, as recommended in Ref. [58]. These reference detectors have already been uses many times and have a well known response.

To study the influence of fading time detectors are irradiated and then stored for different lengths of time. The measurements are all performed with the TL reader which is described in Chapter 2.4.3.
Before the irradiation all detectors are annealed to reset them to the same initial state. Within a maximal time of 2 h after their annealing, the detectors are irradiated once using a ^{137}Cs source. Unless otherwise noted, the irradiation doses correspond to $H_{\mathrm{p}}(10)$ doses. After the irradiation the detectors are stored in an isolated box to guarantee constant environmental conditions particularly with regard to temperature and humidity. The box is also lightproof to avoid influences like optical annealing or stimulation.
The annealing and irradiation of the detectors were planned in such a way that all detectors could be read out within about two weeks to guarantee similar conditions during read out. After the detector is placed on the heating plate, the TL signal is recorded for 20 s. This measurement duration was chosen to include both the whole glow curve with about 10 s and the background for additional 10 s and thus, a robust GCD can be performed afterwards.

For the fading studies a total of 1600 measurements were performed. The detectors were divided into groups of 40. For every fading time four sets of detectors were irradiated, each with one of four different doses, see Table 4.1. Every time directly before an irradiation the corresponding detectors were annealed.

For calibration of the irradiation 450 measurements were performed. The detectors were grouped in batches of 50 and were irradiated with nine different irradiation doses ranging

Table 4.1: Parameters during the measurements for fading studies.

fading times	30 min, 4 h, 1 d, 2 d, 4 d, 10 d, 16 d, 22 d, 32 d and 41 d
irradiation doses	0.5 mSv, 1 mSv, 5 mSv and 10 mSv

from 0.05 mSv to 15 mSv. The fading time of each measurement lies between 25 min and 50 min and the detectors were irradiated directly after their annealing so that the pre-irradiation fading time is 1 h at most.

With the reference detectors more than 700 measurements were performed. For each measurement the detectors were irradiated with 5 mSv directly after their annealing. One part of the detectors were read out with a maximal fading time of 50 min and the other part were read out after the pre-heating process is applied. The reference sample was consistently measured between the different sets of the fading and calibration measurements to investigate possible sensitivity changes of the TL reader.

To investigate the influence of natural radiation, especially on the fading measurements, 200 measurements were performed. The detectors were divided into groups of 20. After their annealing they were immediately stored in the isolated and lightproof box for different time periods ranging from 1 d to 52 d. During this time the detectors were not irradiated with an irradiation source. However, they accumulated the natural radiation. Afterwards the detectors were read out.
Five detectors of each group were annealed after their readout and irradiated with 5 mSv to calibrate all detectors of the group and to compensate possible sensitivity changes of the reader.

The presented data sets are used for all analyses described in the following chapters.

Chapter 5

Preparatory study

The measurements, described in the previous chapter, are used to investigate detector properties, sensitivity changes of the whole readout system and environmental influences on the measurements. These preparatory studies are performed in order to estimate their impact on the fading and calibration measurements and to develop appropriate corrections.

Investigations concerning the detector response include the impact of different amounts of LiF:Mg,Ti as well as the impact of a reflective layer on the detectors. In addition, the individual response of different detector series is compared. The reference measurements are used to estimate sensitivity changes of the readout system. Furthermore, the impact of natural radiation on the fading measurements is studied.

5.1 Impact of production methods on the detector response

During the development of the production process for the TL detectors, different production methods have been adapted to simplify the production process and physically motivated changes are made to improve the detectors.

With the data taken for this thesis (see Chapter 4), it is possible for the first time to study the impact of those changes based on high statistics and to review the previous results.

5.1.1 Amount of LiF

During the production process a small amount of LiF:Mg,Ti powder is deposited on the pretreated aluminum carrier plate, see Chapter 2.4. The exact quantity deviates slightly between the different detector series and the individual detectors.

The reference detectors, as described in Chapter 4, belong to the so-called *R14* series. The amount of LiF:Mg,Ti for this series ranges from approximately 15 mg to 21 mg with a mean value and standard deviation of (17.76 ± 2.49) mg. The 800 detectors, that were produced for this thesis and are used for the calibration and fading measurements, belong to the *R16* series and have (15.15 ± 0.56) mg of LiF:Mg,Ti powder.

The more LiF:Mg,Ti is applied on the detectors the more TL signal is expected for the same irradiation dose. The influence of the different amounts can be investigated because the weight of the LiF:Mg,Ti powder is noted during the production process in the prototyping phase for every single detector.

In Figure 5.1 the number of signal photons normalized to the mean value for the respective series and irradiation dose is plotted versus the LiF:Mg,Ti mass. It is clearly visible that a higher amount of LiF:Mg,Ti results in a higher TL signal.
The detectors of the *R14* series can be divided in two groups, one with approximately 15.5 mg and one with about 20.5 mg Each data point of the *R14* series contains between 29 and 95 measurements and thus, the standard mean errors are smaller compared to the measurements with the *R16* detectors which contain only 2 and 38 measurements per point.

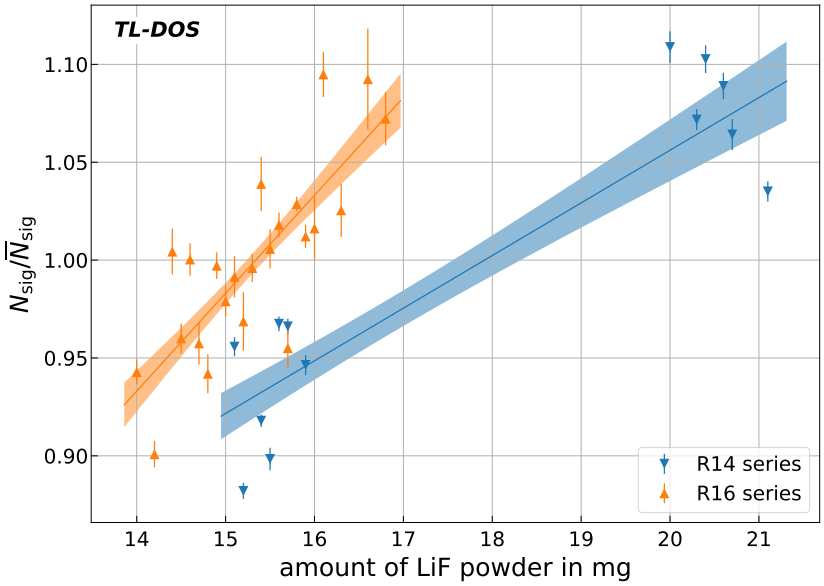

Figure 5.1: The normalized measured number of signal photons are shown as a function of the amount of LiF:Mg,Ti. The means are plotted together with their standard mean errors. A linear function is adapted to each detector series and its uncertainty is plotted as well.

For both detector series a linear relationship can be determined by fitting a straight line to each series. Such a linear dependency was found in Ref. [27] as well during the

investigation of small detector elements for $H_p(0.07)$ dosemeters.

As evident in Figure 5.1, the two adapted lines provide different slopes. This observation can be explained by different production techniques between the two series. Especially, the way to deposit the LiF:Mg,Ti power on the aluminum carrier plate and thus the shape of the powder heap changed between the series. An influence of the different application of the powder on the amount of TL light was also observed in Ref. [27].
Although it is time consuming to note the weight of LiF:Mg,Ti of every single detector during the production process, the knowledge of the LiF:Mg,Ti weights together with the estimated slopes of the adapted functions offers the possibility to correct the measured number of signal photons for the different amounts of LiF:Mg,Ti.

To give an assessment of such a correction the variation of the response ($N_{sig}/\overline{N}_{sig}$) from measurements with and without an applied LiF:Mg,Ti mass correction are compared. Figure 5.2 shows a boxplot (dashed lines) for each of the distributions of the response as well as its respective mean value and standard deviation (solid lines). In addition a ±5% interval is plotted to guide the eye. It is motivated by the maximal allowed variation of detector sensitivities according to Ref. [8]. By applying the LiF:Mg,Ti mass correction on

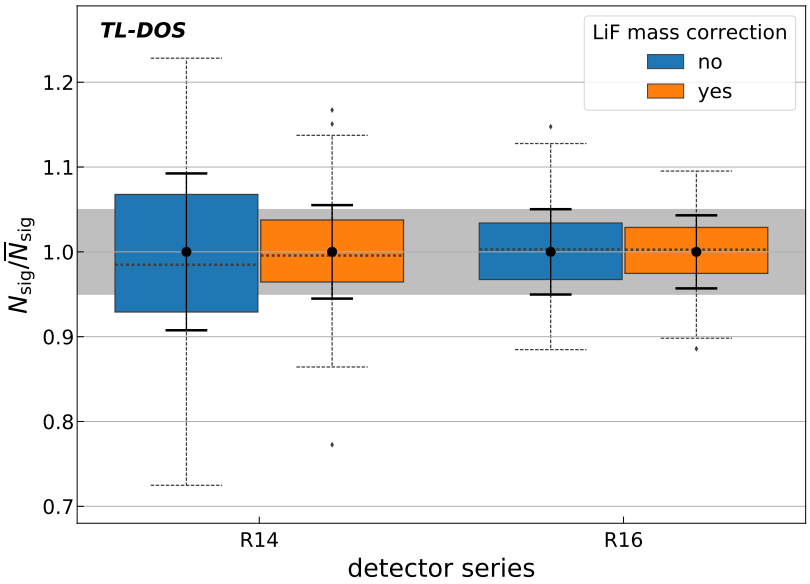

Figure 5.2: Variation of the detector response grouped by the different detector series. The distribution of the responses without a correction (blue) and with the applied LiF:Mg,Ti correction (orange) are shown as boxplots (dashed lines) as well as its respective mean and standard deviation (solid lines).

the *R14* detector series the variation of the response is reduced significantly. The standard deviation of the response is with 5.6% slightly above the ±5% interval. In comparison, the variation of the *R16* series response is even without an applied correction is within

the 5% interval and thus smaller than the response of the *R14* detector series with a correction. The application of the correction for the LiF:Mg,Ti weight on the *R16* series reduces the standard deviation of the response to about 4.3%.

The smaller spread for detectors from the *R16* series shows a more homogeneous production technique, which results in a smaller variation of the detector response.
Consequently, with such a correction, a batch calibration with small deviations can be done (see Chapter 6).

5.1.2 Reflective layer

In addition to slightly different amounts of LiF:Mg,Ti on the detectors, the used detectors differ in the existence of a reflective layer. The detectors of the *R14* series have a reflective layer as well as detectors of the *R16* series up to the production number *R1605xx*, whereas for newer detector with a higher production number the reflective layer is left out.
The motivation to do so was a change of the ceramics on the aluminum substrate. While the first detectors had a thick ceramic layer due to the production process, it is now possible to apply thinner ceramics on the aluminum substrate. Currently, the ceramic layer is so thin that the aluminum layer itself acts as a reflective layer. First investigations presented in Ref. [27] show no difference between the current detectors with a reflective layer and without one.

Although, these investigations are only based on few measurements the reflective layer is left out to omit one additional production step. With the data of the calibration measurements, presented in Chapter 4, an intensive study with high statistic is performed to review the previous results.

Figure 5.3 show the number of signal photons normalized to the irradiation dose for the two detector groups. The plotted data is corrected based on the weight of the LiF:Mg,Ti as described before. The normalized TL signal of detectors with a reflective layer features a slightly higher mean value in comparison to the measurements without a reflective layer. However, the difference is so small that the two mean values are within their standard deviation.
To conclude, no significant difference between detectors with a reflective layer and detectors without one is visible and the previous results can be confirmed based on higher statistics.

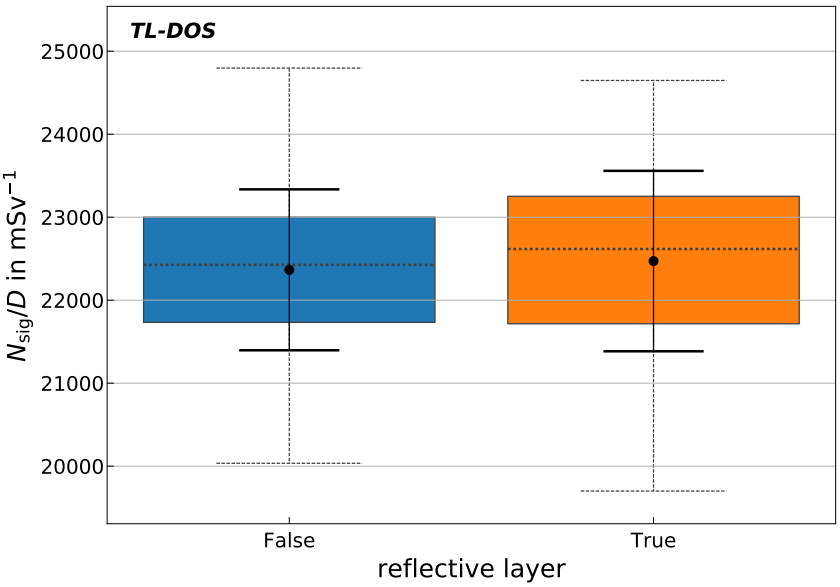

Figure 5.3: Comparison of normalized signal between detectors with (orange) and without (blue) a reflection layer. The distributions are shown as boxplots (dashed lines) as well as their respective mean values and standard deviation (solid lines).

5.2 Sensitivity changes of the readout system

As recommended in Ref. [58], several reference detectors are measured many times between the fading and calibration measurements to identify possible sensitivity changes of the readout system. The detectors of the reference sample are already used many times and have a well known response. They are repeatedly irradiated with the same dose as described in Chapter 4.

The number of signal photon count N_{sig} is normalized to the signal photon counts of the first measurement and plotted versus the time t_{past} since the first measurement. The left part of Figure 5.4 shows the development of the response for the reference measurements during the fading and calibration measurements over a period of 55 d. The individual reference measurements are grouped in one hour intervals.
Some extra detectors are used to test whether the decrease originates from the reader or from the detectors themselves because they are measured so many times. The extra detectors are treated like the other reference detectors with the exception that they are only measured at the beginning of the whole measurement series and at the end. In between they are stored under constant conditions.

It is clearly visible that the response decreases by about 15% between the first and the last measurement. The response of the extra detectors shows a similar decrease and thus, it can be concluded that the reader loses its sensitivity and not the detectors itself. The

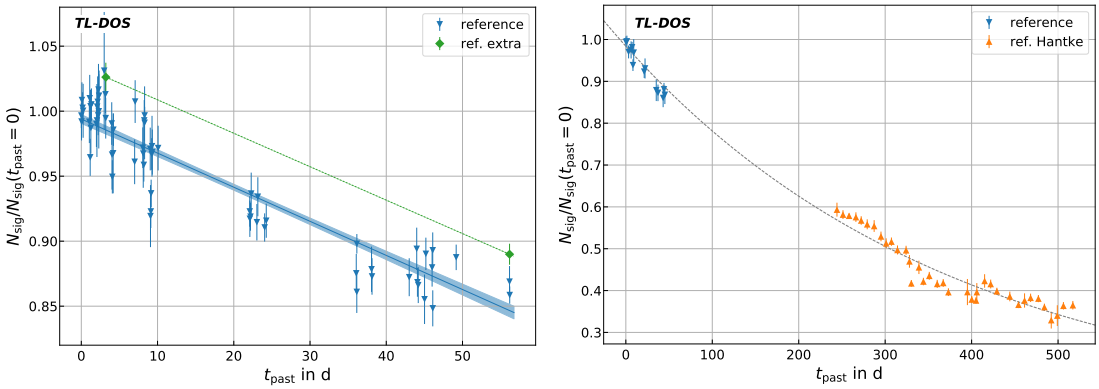

Figure 5.4: Decrease of the normalized number of signal photon counts as a function of the past time. The mean values and standard mean error of the reference measurement are shown in blue and of the extra detectors in green. Left: Sensitivity decrease during the measurements performed for this thesis. Right: Comparison of the reference measurements with those from Ref. [26] (orange) for the last year. The individual measurements are grouped in intervals of one day.

slightly higher response of the extra detectors compared to the other reference detectors can be explained by individual detector sensitivities arising from slightly different production process, see Section 5.1.

The observed decrease is approximated by a straight line and a linear function is adapted to the data. With this fitted function it is possible to correct the measurements for this sensitivity decrease of the reader to make the individual measurements comparable.

Since the reason for this decrease is unknown, other dependencies of the response are investigated such as the accumulated photon counts or the measurement number. However, no dependency could be identified in the measured data and the adapted functions. Thus, the time dependency is chosen for the calculation of a correction, because for the accumulated photon counts or the measurement number every measurement needs to be taken into account, which can be challenging if the reader is used by different people for different studies.

After the decrease of the sensitivity was observed during the measurements in this thesis, the investigations are continued with the same reference detectors within a Master's thesis [26]. A part of the further data is shown in the right part of Figure 5.4.
Including all reference measurements, the decay of the sensitivity can be described with an exponential decrease. The difference between the exponential decay and the linear function, which is chosen for the sensitivity corrections in this thesis, can be neglected for the data used in this theses.

As a possible source for the sensitivity decrease of the reader, the PMT can be considered.

For example, the vacuum quality could decreases or the release of electrons could cause an aging of the PMT. However, none of these reasons can be clearly identified from the data.

To conclude, a sensitivity decrease of the TL reader is found, but it is not yet finally understood and have to be investigated in more detail. Either way, the reference measurements allow to correct for the sensitivity decrease and make the individual measurements comparable.

5.3 Contribution of the natural radiation

For the fading measurements the detectors are stored after the irradiation until readout for different times. During this time the detectors are permanently exposed to the natural radiation. The influence of the natural radiation on a measurement depends on the irradiated dose as well as on the elapsed time between annealing and readout.
For most measurements, e.g. the calibration measurements described in Chapter 4, the contribution of the natural radiation to the glow curve can be neglected since the accumulated natural radiation dose is negligible compared to the dose from the irradiation. However, the influence of the natural radiation has to be considered for the fading measurements, especially for the 0.5 mSv measurements.

The left part of Figure 5.5 shows the impact of the natural radiation on the relative decrease of the number of signal counts as a function of the fading time for two different doses. In addition, the expected signal decrease due to thermal fading without contribution of natural radiation is plotted as a comparison.
It is expected that the number of signal counts decreases as a function of the fading time, see dashed green line. However, the presence of natural radiation changes the shape of the decrease and leads even to an increase of the relative number of signal counts for an irradiation dose of 0.5 mSv. Whereas, the contribution of the natural radiation to an irradiation of 10 mSv is nearly negligible.
To generate the plot the information of the fading time analysis of Chapter 6 and the measured amount of natural radiation as a function of time, which is shown in Figure 5.6, are used. The right part of Figure 5.5 shows the contribution of the natural radiation to the number of measured photons as a function of the irradiation dose as well as the time between annealing and readout. The brighter the color the less the measured counts are influenced by the natural radiation. It is clearly visible that for irradiation doses smaller than 1 mSv the contribution is higher than 10% for 40 d of fading. Therefore, it is important to take the contribution of the natural radiation into account for the analysis of the fading measurements.

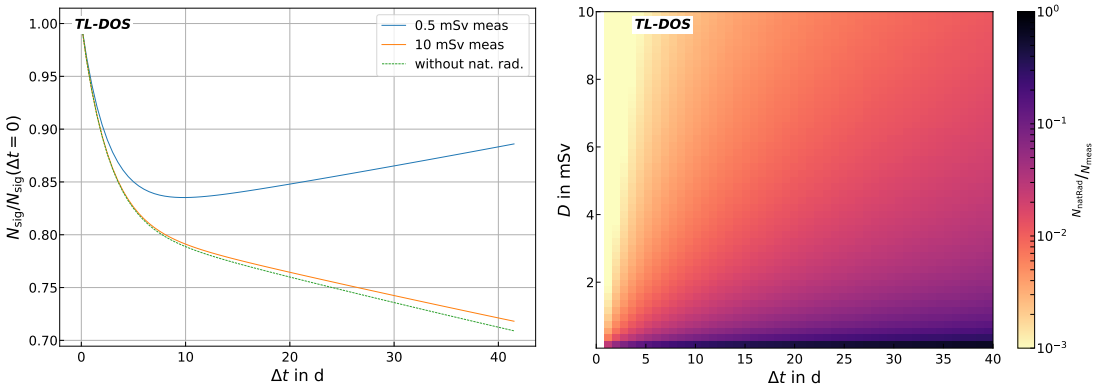

Figure 5.5: Left: Influence of the natural radiation on the fading characteristics after irradiation with different doses (blue: 0.5 mSv, orange: 10 mSv) in comparison to a theoretical characteristic without the presence of natural radiation (dashed green). Right: Contribution of the natural radiation to the number of measured photons as a function of the irradiation dose and the time of storage.

For this reason, the natural radiation is investigated in two additional measurements. After the annealing of the detectors, they are stored and an accumulation of the number of signal photon counts in combination with thermal signal fading are expected. The calibration measurements, as described in Chapter 4, after each readout are used to compensate for the sensitivity decrease of the reader between the single measurements.

The measured number of signal photon counts inside the RoI, N_{RoI}, are shown in the left part of Figure 5.6 as a function of the time t between annealing and readout. N_{RoI} is taken instead of N_{sig} because the fit of the glow curve is prone to errors for low statistics, e.g. the first two measurements of the second measurement series, whereas the calculation of N_{RoI} while not as precise, is more resistant to errors even for very low statistics.

Both measurements have the same y-axis intercept due to the reader background which arises from the black body radiation of the detector during heating. In contrast, the slope of the two measurement series is different. The second measurement series shows a less steep increase of the number of signal photons compared to the first one. The reason for this may be different environmental conditions during storage. The detectors are indeed stored in an isolated box to reduce the influence of fast changing temperature, but it is not cooled to hold it on a constant temperature. Thus, temperature changes on a longer time scale effect the temperature inside the storage box. A higher temperature during storage implies a higher fading rate and therefore less signal and a lower indicated irradiation dose.

The box for storage of the detectors is located inside a building directly behind a window on the window ledge and therefore, the temperature inside the box may be influenced by outside temperature and sunshine. The first measurement series was performed from

2017-04-27 till 2017-06-07 and the second between 2017-08-01 and 2017-09-22.
Assuming that the average temperature inside the box during the second measurement series are higher than during the first one, the difference of the slopes in the left part of Figure 5.6 can be explained. To test this hypotheses, a new measurement series is currently performed in which the storage of the detectors is cooled to keep them under a constant temperature of 17 °C, which is definitely lower than during the previous measurements.
If the slope of the resulting measurement is steeper than the others, which means that less signal is faded, the hypotheses can be verified. Otherwise, a different explanation has to be found. However, the first measurement series of the natural radiation is closer to the fading measurements and thus, only the first one is taken for further investigations and calculation in this thesis.

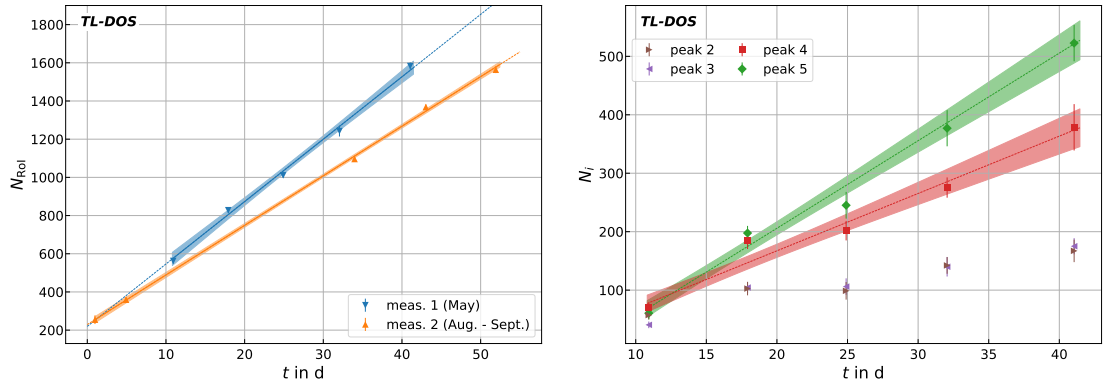

Figure 5.6: Left: The number of photons inside the RoI as a function of the storage time. The two measurements were performed at different times. Right: Peak-resolved increase of the number of photon counts due to natural radiation.

The right part of Figure 5.6 shows the individual integrals of the single peaks as a function of the elapsed time t_{past} between annihilation and readout.

As described in Chapter 2.3, low-temperature peaks show higher fading rates than the high-temperature peaks. Consequently, a saturation of the measured photon counts is expected over time for the low-temperature peaks due to an equilibrium of signal accumulation and signal fading. However, neither peak P_2 nor P_3 show an equilibrium and for this reason, it can be concluded that a saturation of the measured number of photons in the first two peaks is not observed within 40 d of storage.

Peaks at higher temperatures are expected to show a higher increase over time with only a low amount of fading and a linear increase can be assumed. The peaks P_4 and P_5 as well as the number of signal photon counts are used for the analysis presented in the next Chapter 6. By fitting a linear function to these three attributes, their increase over time can be modeled and with this the fading measurements can be corrected to remove

the influence of the natural radiation for the fading time analysis. In contrast, for the analysis in Chapter 7 no correction is applied to the data.

A further investigation of the natural radiation as a function of time can provide knowledge about the irradiation dose accumulation during permanent irradiation and the behavior of the individual peaks, e.g. a possible saturation effect.

Chapter 6

Glow curve analysis with glow curve deconvolution

The main quality of interest in dosimetry is to estimate the irradiation dose and thus, the calibration process is investigated including an estimation of the uncertainties. If using thermoluminescence (TL) dosemeters, the estimated irradiation dose depends on the time between irradiation and the readout. Therefore, these fading influences on a glow curve are investigated and a technique to estimate the fading time and correct the irradiation dose for the fading is developed. Furthermore, the uncertainties on the fading time as well as on the irradiation dose estimation from a faded glow curve are estimated.

The irradiation dose and its uncertainty estimation, based on a data set which was measured during a Master's thesis [45], were already described in Ref. [3]. The fading time and irradiation dose estimation of a faded glow curve were described in Ref. [4].

6.1 Calibration of the detectors

In this section a calibration function is determined with which an irradiation dose can be estimated based on the number of measured photons. In addition, the uncertainties of such a calibration are investigated as a function of the irradiation dose.

6.1.1 Determination of the calibration function

The nominal range of use for whole body dosemeters in personal routine dosimetry ranges from 0.1 mSv to 1 Sv [8]. In this range the linear correlation between the measured photon counts and an irradiated dose, see Chapter 2.2, is used to give an estimate of the irradiation dose.
To determine a calibration function and its uncertainties, measurements with different

irradiation doses ranging from 0.05 mSv to 15 mSv and no fading are performed as described in Chapter 4. There are so much measurements so that it is not practical to apply an individual calibration on each of them. Hence, one calibration function is determined to calibrate the fading measurements in the following sections.

The measured signal photon counts N_{sig} are averaged over all detectors irradiated with the same dose and plotted versus the irradiation dose D. The mean values and the corresponding standard mean errors are shown in the top part of Figure 6.1. A linear

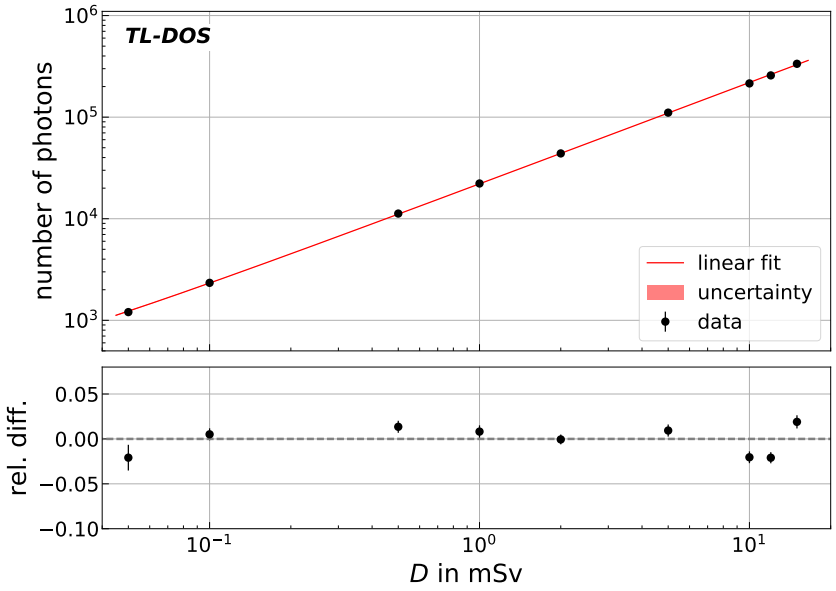

Figure 6.1: Top: Linear correlation between the measured signal photon counts and the irradiation dose. The standard mean errors are mostly smaller than the marker size. Bottom: Relative difference between the adapted linear function and the data. Adapted from Ref. [3].

function ($N = a + b \cdot D$) is adapted to the data in order to estimate the fit parameter a and b. The bottom part of Figure 6.1 shows the relative difference between the data and the fit function. By inverting the function, a calibrated irradiation dose D_{calib} can be estimated from the measured number of signal photon counts N.

$$D_{calib} = -\frac{a}{b} + \frac{1}{b} \cdot N = A + B \cdot N \tag{6.1}$$

This calibration function is used in the following to convert the measured photon counts to an irradiation dose.

6.1.2 Uncertainties of the calibration

As described above, the individual sensitivities of the detectors are ignored for now, instead the variation of the different detector sensitivities and the uncertainty of the calibration itself are investigated in the following. The different sources of uncertainties are shown in Figure 6.1.

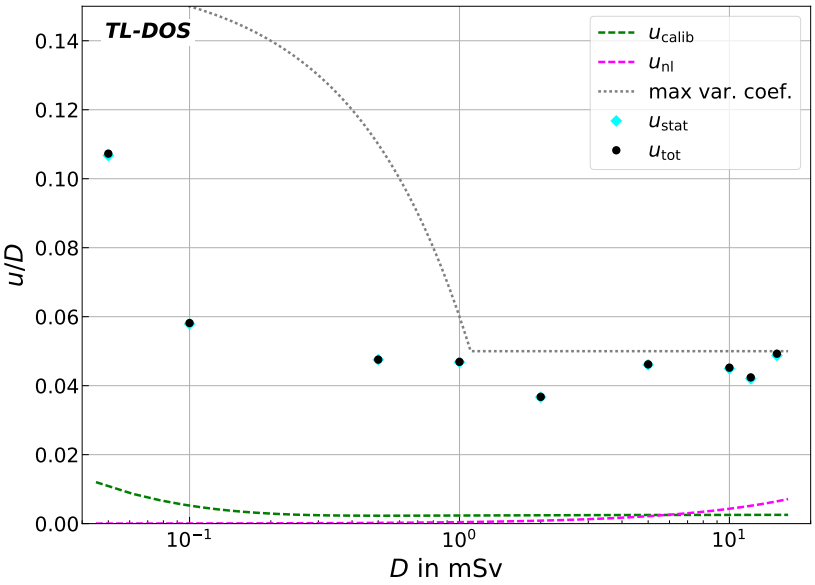

Figure 6.2: Composition of the total uncertainty of a calibration as a function of the irradiation dose. The maximal variation coefficient (max var. coef.), defined by the PTB, is plotted to guide the eye. Adapted from Ref. [3].

The uncertainty of the fit function itself, u_{calib}, is calculated by the uncertainty propagation of the fit parameter a and b. It decreases from about 1.3% for an irradiation dose of 0.05 mSv to less than 0.5% for 2 mSv and remains approximately constant for higher irradiation doses.
u_{nl} gives an estimate of the uncertainty induced by a non-linearity of the calibration. Since no evident systematic deviation between the linear fit function and the data is observed in the bottom part of Figure 6.1, a quadratic component is used to model a possible non-linearity. u_{nl} is calculated by adapting a parabola to the the systematic deviations as a function of the irradiation dose,

$$D_{\text{calib}} - D = u_{\text{nl}} \cdot D^2. \tag{6.2}$$

The uncertainty increases slowly from zero to about 1% for an irradiation dose of 15 mSv. Both uncertainties, u_{calib} and u_{nl} are very small and can be neglected.

The variation of the different detector sensitivities is represented by the statistical uncertainty u_{stat}, which is estimated by the standard deviation σ_N of a sample of detectors for each irradiation dose. The measured signal photon counts show a higher variation for lower doses, about 11% for an irradiation dose of 0.05 mSv, due to less statistics. For higher irradiation doses the statistical deviation decreases to a bit less than 5%.

The total uncertainty u_{tot} is the quadratic sum of the three contributions u_{calib}, u_{nl} and u_{stat}. It is clearly visible that u_{stat} has the highest contribution to total uncertainty u_{tot}, but nevertheless it is lower than the maximal variation coefficient for whole body dosemeters in personal routine, specified by the PTB [8].

It should be mentioned that an individual calibration of each detector, as performed in individual dosimetry, should lower u_{stat}, whereas u_{nl} and u_{calib} are unaffected.

6.2 Fading time estimation

The measured irradiation dose by a dosemeter is influenced by the effect of fading. If the fading characteristics of the used material and the fading time are known, the estimated irradiation dose can be corrected for the signal decrease due to fading [59, 60].

In routine dosimetry a possible irradiation date and, consequently, the fading time are usually unknown. However, to be able to estimate an accurate irradiation dose, the estimation can be derived from the high-temperature peaks. For this purpose there are two approaches.
On the one hand, by applying a pre-heating technique as described in Chapter 2.4.3 the highly fading time dependent low-temperature peaks are erased and the remaining TL signal is mostly independent of the elapsed time between irradiation and readout [23, 22].
On the other hand, if the whole glow curve is read out, a GCD can be applied or a suitable RoI can be set as in Ref. [61] to limit the irradiation dose estimation to the high-temperature peaks, which makes the estimated irradiation dose independent of any fading time influences.

All these methods have in common that they reduce the overall signal strength and remove possible information about the irradiation itself. In the following an alternative approach is presented to estimate the fading time directly from the glow curve.

6.2.1 A possible estimator for the fading time

The estimation of the fading time takes the different impact of the fading on the individual glow peaks into account. Due to the different half-lifes of the peaks, described in

Chapter 2.3, the ratio of two peak contents changes during the time between irradiation and readout and therefore, it can be used as an estimator. The single peak contents are obtained from the GCD.

Peak ratios were already used in the past to estimate the fading time, e.g. the ratio P_3/P_5 is used for the fading time investigation of a LiF:Mg,Ti detector [62]. In addition, peak ratios are also used for the fading time analysis of $CaSO_4$:Dy and LiF:Mg,Cu,P detectors [63, 64].

In comparison to the commonly used linear heating rates, the heating rates during exponential heating are very high and therefore, it is difficult to separate especially the glow peaks P_4 and P_5 in a GCD, because they are highly overlapping. Furthermore, both glow peaks show a similar fading rate over the investigated fading time range. Consequently, the sum of both peaks ($N_4 + N_5$) is used in the following analysis to avoid the influence of peak overlap in GCD.

To estimate the fading time the fading ratio F is defined as the sum of the photon counts in the fourth and fifths glow peaks divided by the number signal photon counts N_{sig}. As shown in Figure 6.3, the fading ratio F is a non-linear function of the fading time Δt. In the figure the data of the four different investigated irradiation doses, 0.5 mSv, 1 mSv, 5 mSv and 10 mSv, is averaged over certain fading time intervals and the means are plotted together with their standard mean errors. F increases from 0.60, directly after the irradiation ($\Delta t = 0$), up to 0.87 for more than 40 d of fading. For higher fading times the increase becomes more gently inclined compared to the steep increase at the beginning.

Equation (6.3) is a simple empiric parameterization to describe the trend of the non-linear correlation between F and Δt.

$$F(\Delta t) = A \cdot \sqrt{\Delta t} + B \cdot \Delta t + C \tag{6.3}$$

The fit parameter A, B and C depend on the used detectors as well as on the environmental conditions during the storage. The presented parameterization has less parameter compared to Ref. [63] and only one quantity is needed to describe the fading in contrast to Ref. [62] where two quantities (one for short- and one for long-time fading) are used.

By computing F and solving Equation (6.3) for Δt the fading time can be estimated up to at least five weeks. For longer fading time F diverges and the parameterization deviates from the data.

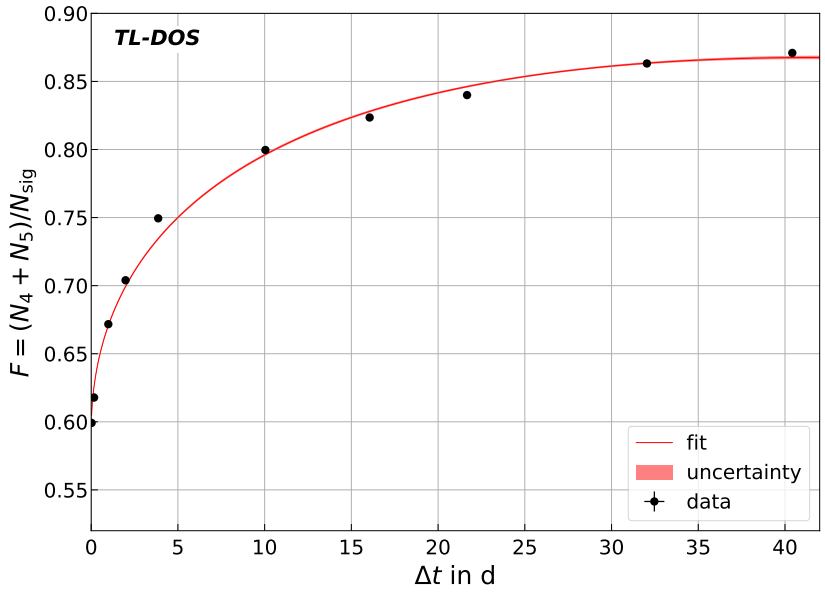

Figure 6.3: Non-linear correlation between the fading ratio F and the fading time Δt. The data points are combinations of the investigated irradiation doses. Equation (6.3) is used to fit the data and error propagation is used to calculate the uncertainty (red). The standard mean errors are mostly smaller than the marker size. Adapted from Ref. [4].

6.2.2 Robustness of the estimator F

In the following the dependence of the fading ratio on the irradiation dose and the irradiation energy is investigated to draw conclusions on the stability and robustness of the quantity F.

To investigate the dependency on the irradiation dose, the fading ratio for different doses, ranging from 0.05 mSv to 15 mSv, and different fading times is measured. For irradiation doses above 0.1 mSv the fading ratios are consistent within their standard uncertainties, as shown in the top part of Figure 6.4. Whereas F decreases for irradiation doses of and below 0.1 mSv. Furthermore, the figure shows that the fading ratios have similar values within the same fading time. Table 6.1 shows the best fit parameter values of Equation (6.3) for different irradiation doses.
Although the values differ slightly, no dependence of the estimator F on irradiation dose is observed for doses higher than 0.1 mSv, which is the lower detection limit defined by the PTB, see Ref. [8].
In contrast, the irradiation dose has only an impact on the uncertainties as shown in the bottom part of Figure 6.4. A higher irradiation dose results in a lower relative standard deviation σ_F/F. The uncertainty decreases from 15% at 0.05 mSv to 4% at 15 mSv. For irradiation doses larger than 2 mSv the uncertainty is less than 5%.

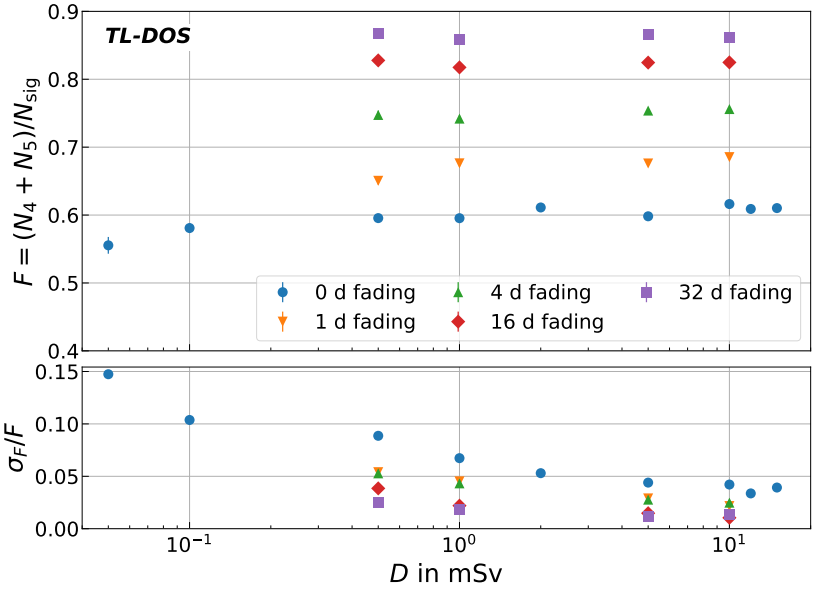

Figure 6.4: Top: Fading ratios and their standard mean error measured at different irradiation doses and fading times. The standard mean errors are mostly smaller than the marker size. Bottom: The relative standard deviation of the measured fading ratios as a function of the irradiation dose. Adapted from Ref. [4].

Table 6.1: Calculated best fit parameter values of Equation (6.3) for different irradiation doses. The combined data and the adapted fit function are shown in Figure 6.3. [4]

irrad dose	A	B	C
all	0.085(1)	−0.0066(2)	0.593(2)
0.5 mSv	0.097(3)	−0.0080(5)	0.570(5)
1 mSv	0.079(3)	−0.0060(4)	0.601(4)
5 mSv	0.081(2)	−0.0059(2)	0.600(3)
10 mSv	0.079(1)	−0.0059(2)	0.607(2)

It is well known, that the irradiation energy influences the total amount of TL signal from LiF:Mg,Ti detectors. The response of bare TL-DOS detectors as a function of the irradiation energy was already studied in Ref. [25]. However, the shape of the glow curve does not change with irradiation energy, and thus, the fading ratio should be independent of the energy. This behavior is studied in an energy range from 15 keV to 662 keV with 16 different x-ray qualities (15 keV to 118 keV) and a ^{137}Cs gamma source (662 keV).

The measured fading ratios are plotted as a function of the irradiation energy, which is shown in Figure 6.5. A constant function, which is adapted to the data, describes the data very well and the relative uncertainty, provided by the fit, is lower than 0.5% on the fitted constant.

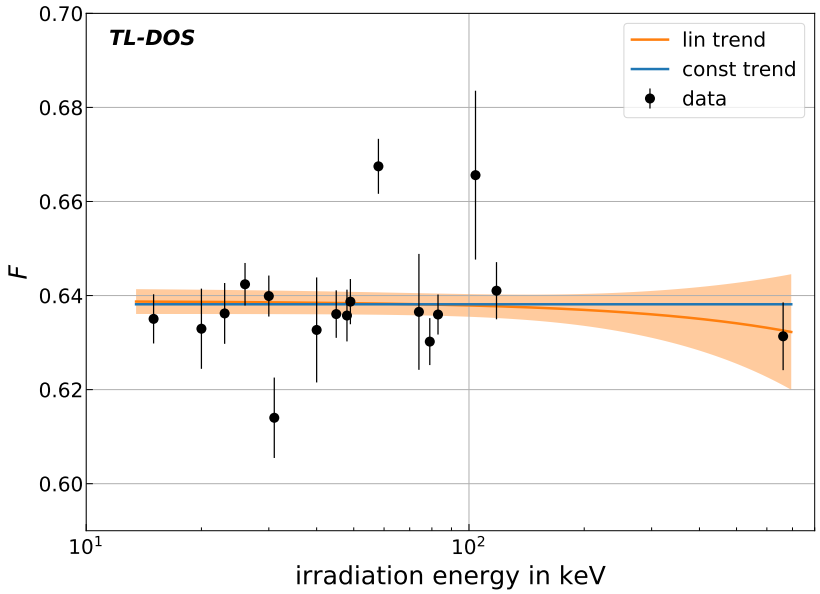

Figure 6.5: Fading ratio and their standard mean error as a function of the irradiation energy. A constant and a linear function are adapted to the data in oder to investigate an irradiation energy dependency of the fading ratio.

To evaluate a potential linear dependence of the fading ratio on the irradiation energy, a straight line is adapted to the data. The uncertainty of the fitted function ranges from 0.5% at 15 keV to a bit less than 2% at 662 keV and includes the constant function over the whole energy range. Hence, the linear model is compatible with the constant assumption.
Consequently, it can be concluded that the estimator F is independent of the irradiation energy, as expected.

To summarize, no dependency of the fading ratio F on the irradiation dose (for irradiation doses higher than 0.1 mSv) and on the irradiation energy (from 15 keV to 662 keV) is observed. Therefore, the fading ratio F is a robust estimator of the fading time.

6.2.3 Uncertainties of the fading time

Different sources of uncertainties have to be considered to give an assessment on the reliability of the estimated fading time.
One uncertainty, $u_{\Delta t;\mathrm{func}}$, arises from the fit function (6.3) itself and can be calculated by uncertainty propagation of the fit parameter.
$u_{\Delta t;\mathrm{devi}}$ gives an estimate of the systematic deviation between the fit function and the data points. To model the uncertainty, the deviations are plotted versus the fading time

and a quadratic function is adapted to the data. Both uncertainties, $u_{\Delta t;\mathrm{func}}$ and $u_{\Delta t;\mathrm{devi}}$, are considered as systematic uncertainties.

The statistical uncertainty, $u_{\Delta t;\mathrm{stat}}$, is induced by the standard deviations σ_F. It is observed that σ_F decreases for longer fading times and can be approximated by a simple exponential decrease. The fading ratios at a dose of 0.5 mSv shows the highest variations of the three investigated irradiation doses, as seen in the bottom part of Figure 6.4. Thus, the adapted exponential decrease to the standard deviation at 0.5 mSv is taken as an estimate for the maximal statistical uncertainty.

By considering these three uncertainties, the maximal total uncertainty $u_{\Delta t}$ on the estimated fading time can be calculated as the quadratic sum of $u_{\Delta t;\mathrm{func}}$, $u_{\Delta t;\mathrm{devi}}$ and $u_{\Delta t;\mathrm{stat}}$. Figure 6.6 shows the total uncertainty as well as the three contributing uncertainties as a function of fading time.

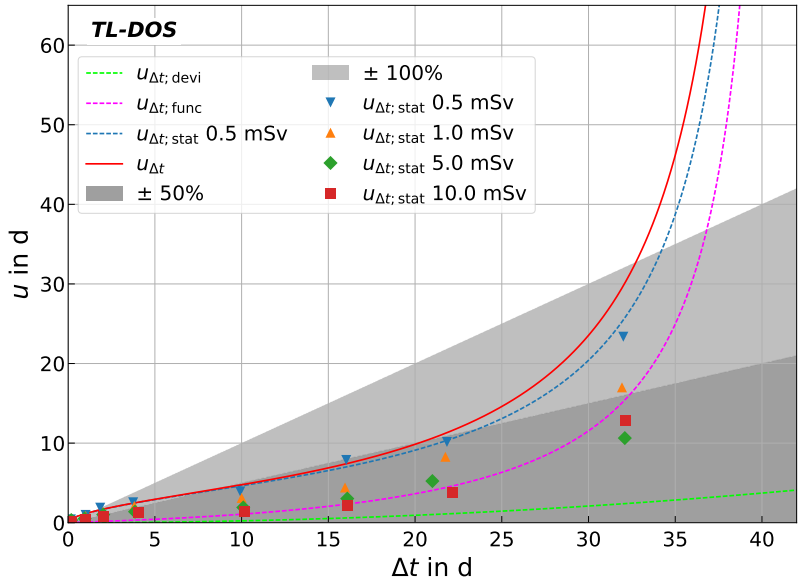

Figure 6.6: Contribution of the three considered uncertainties to the total uncertainty on the estimated fading time. To guide the eye, a 50% and a 100% range is plotted. Adapted from Ref. [4].

The statistical uncertainty shows the highest contribution to the total uncertainty over the complete investigated fading time. It increases from 0 d with no fading up to 39 d after 35 d of fading. In between, the relative statistical uncertainty $u_{\Delta t;\mathrm{stat}}/\Delta t$ is about 50% in a time interval from approximately 5 d to 24 d before it increases dramatically for higher fading times. The uncertainty of fit function $u_{\Delta t;\mathrm{func}}$ shows a slow increase ranging from 0 d directly after irradiation to 5 d after 25 d. Afterwards it increases rapidly to 25 d after 35 d followed by a dramatic increase due to the divergence of the fit function. The

contribution of the systematic deviation $u_{\Delta t;\mathrm{devi}}$ can be neglected, it increases from 0 d to just about 3.5 d after 40 d.

As seen in Subsection 6.2.1 the estimator F diverges for longer fading times resulting in a large uncertainty for fading time higher than 34 d. This dramatic increase of the uncertainty for longer fading time is mostly driven by $u_{\Delta t;\mathrm{stat}}$ and $u_{\Delta t;\mathrm{func}}$, whereas the systematic deviation is not affected by the divergence of the parameterization.

In spite of the dramatic increase, the total uncertainty is about 50% for fading times between 5 d and 25 d and smaller than 100% for fading times up to 34 d. Afterwards no reliable prediction can be made. Therefore, the presented estimator can be used to estimate the fading time to 34 d, which is a sufficient time interval in individual routine dose monitoring.

6.3 Irradiation dose estimation with fading influences

In individual dose monitoring, the knowledge about the time of irradiation is a useful additional information, but it is much more important to know the irradiation dose itself.

Due to the loss of TL signal during fading it is difficult to estimate an unbiased irradiation dose. However, the additional information of the elapsed time since irradiation, as described in the previous section, can be used to correct the measured signal photon counts and estimate a fading time independent irradiation dose. Such a technique is presented in the following.

6.3.1 Initial photon counts estimation

The relative decrease of the signal strength is irradiation dose independent and can be described by

$$f_{\mathrm{rel}} = \frac{N_{\mathrm{t}}(\Delta t)}{N_0}, \tag{6.4}$$

where N_0 is the number of signal photon counts directly after the irradiation and $N_{\mathrm{t}}(\Delta t)$ the fading time dependent number of signal photons.

Figure 6.7 shows the development of signal strength as a function of the fading time. The relative number of signal photons decreases from 1 to 0.7 within 40 d after irradiation. After a rapid loss of TL signal at the beginning, the decrease becomes smaller for longer

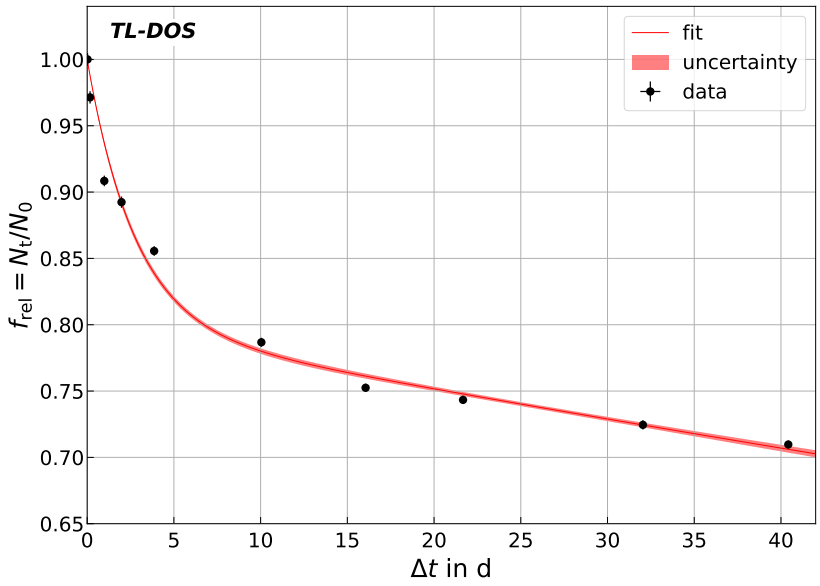

Figure 6.7: Averaged relative number of signal photons as a function of the fading time. The standard mean errors are mostly smaller than the marker size. The data is adapted with the denominator of Eqn. (6.5). Adapted from Ref. [4].

fading times. The sum of two exponential function (denominator of Eqn. (6.5)) is used to empirically model the loss of signal, see Ref. [65].

By solving Equation (6.4) for the initial photon counts N_0:

$$N_0 = \frac{N_\mathrm{t}(\Delta t)}{f_\mathrm{rel}(\Delta t)} = \frac{N_\mathrm{t}(\Delta t)}{A \cdot \mathrm{e}^{-B \cdot \Delta t} + (1 - A) \cdot \mathrm{e}^{-C \cdot \Delta t}}. \tag{6.5}$$

A, B and C are free parameter which are estimated during the fit of f_rel to the data. Since the amount of fading depends on the environmental conditions during storage as well as on the used detectors, the fit parameter are not independent of them.

6.3.2 Uncertainties of the initial photon counts estimation

Similar to Section 6.2.3, the systematic uncertainties arising from the fit function itself and from the systematic deviation between the data and the fit, as well as the statistical uncertainty contribute to the total uncertainty of the initial number of signal photons u_{N_0}. In addition, the uncertainty of the estimated fading time $u_{\Delta t}$ is taken into account. The total uncertainty u_{N_0} is calculated by the quadratic summation of the four different uncertainties. All uncertainties are shown in Figure 6.8.

$u_{f\mathrm{rel;func}}$ is the uncertainty from the fit function itself and is calculated by propagating the uncertainties of the fit parameter A, B and C. The systematic deviation $u_{f\mathrm{rel;devi}}$

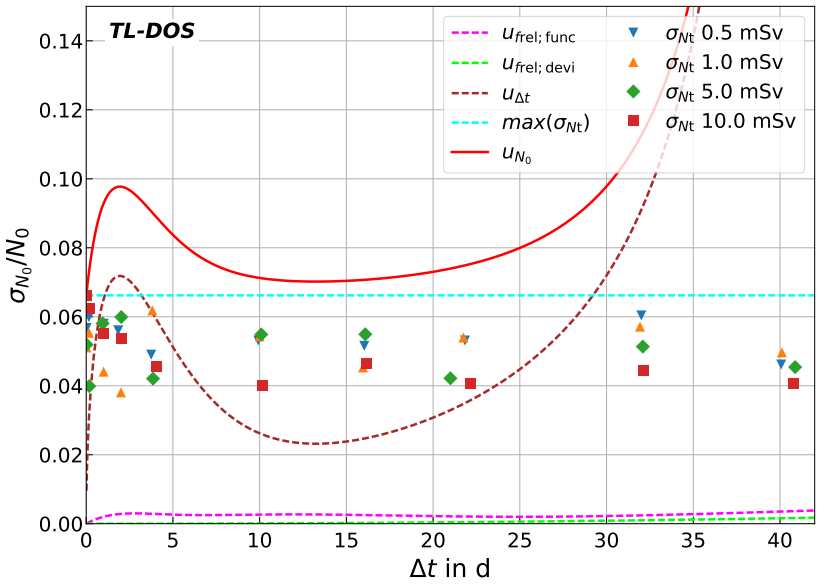

Figure 6.8: Total uncertainty of the initial number of signal photons. The four uncertainty contributions are summed up quadratically to the total uncertainty u_{N_0}. Adapted from Ref. [4].

between the fit function and the data is modeled by adapting a quadratic function to the absolute deviations like in Section 6.2.3. Both systematic uncertainties are smaller than 0.5% over the complete investigated fading time range and thus, their contribution to the total uncertainty can be neglected.

A much higher contribution is induced by the variation of measured number of photons $\sigma_{N\mathrm{t}}$. This statistical uncertainty seems to be independent of the fading time as well as of the irradiation dose and therefore, the maximal value of 6.8% of all variation for all irradiation doses is taken as a constant estimate.

Furthermore, the uncertainty of the estimated fading time $u_{\Delta t}$, calculated in the previous section, is considered as a source of uncertainty. It increases up to a local maximum of 7% after approximately 2 d between irradiation and readout, before decreasing to about 2% for fading times up to 12 d. Afterwards, it increases strongly to above 15% for a fading time of 35 d.
Compared to the large uncertainty of the estimated fading time $u_{\Delta t}$, its contribution to the total uncertainty of the initial number of signal photons u_{N_0} is relatively small due the contrary trend of the two functions $F(\Delta t)$ and $f_{\mathrm{rel}}(\Delta t)$.

However, $\sigma_{N\mathrm{t}}$ and $u_{\Delta t}$ dominate the uncertainty budget of the estimation of the initial number of signal photons.

6.3.3 Irradiation dose estimation and its uncertainties

The estimated number of initial signal photons N_0 is a fading time independent quantity which allows to estimate an also fading time independent irradiation dose D_{reco}. For this purpose the calibration shown in Section 6.1 is applied to the quantity N_0. This calibration is done on glow curves which are read out directly after irradiation and thus, the calibration can be used to estimate D_{reco}.
The uncertainties of the calibration include the propagated uncertainty of the fit parameter as well as the systematic deviation as described. In contrast to the previous section, the total uncertainty of the number of initial signal photons u_{N_0} is taken as the variation of the dosemeters, corresponding to σ_{stat} in the uncertainty consideration of the calibration.

Figure 6.9 shows the relative deviation between estimated and real irradiation dose as a function of the fading time. A ±15% interval is plotted to guide the eye. This range is motivated by international terms of reference for allowed deviations in the estimation of the irradiation dose, e.g. as defined by the PTB (-13%;+18%) [8].

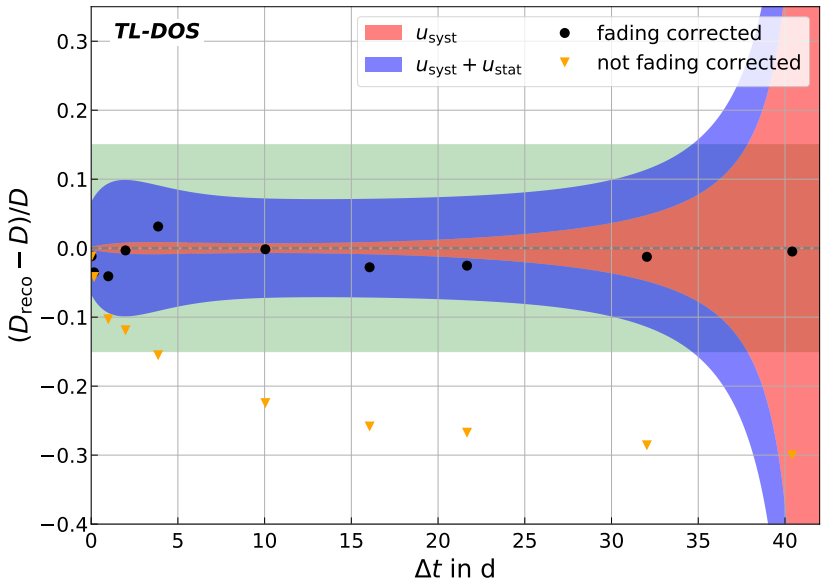

Figure 6.9: The relative deviations between the estimated and the real irradiation dose are shown for methods with (black) and without (orange) fading time correction. The systematic uncertainty is shown in red and the quadratic summation of the systematic and statistical uncertainties in blue. Both are plotted as a confidence interval around zero. Adapted from Ref. [4].

The irradiation dose estimation without any fading time consideration is compared to the technique presented in this chapter, which includes the fading time into the estimation.

Without any fading time correction, the deviations between the estimated and the real irradiation dose are already higher than 10% after 3 d and after 5 d they are outside the specified ±15% range. Whereas the relative deviations of the estimation considering the fading time are smaller than 5% over the whole investigated fading time and thus, they are clearly inside ±15% range.

The systematic deviation is about 1% for fading times up to 15 d. Afterwards it rises slowly, followed by a dramatical increase after 35 d. The statistical uncertainty dominates the total uncertainty up to about 25 d of fading. For longer fading time the systematic uncertainty contributes very considerably to the total uncertainty of the estimated irradiation dose. Including all investigated uncertainties, the uncertainty of the estimated irradiation dose is within the defined range up to approximately 34 d and for fading times shorter than 30 d it is even smaller than 10%.

Due to the dramatic increase for longer fading times it is not possible to give a reliable estimation for fading times longer than approximately 34 d with the presented functions. However, an estimation of an upper limit of the irradiation dose is always possible, due to the known time between annealing and readout, the maximal possible fading time. In this way the point at approximately 40 d is reconstructed.

It can be concluded that the presented technique, including all investigated uncertainties, guarantees a reliable irradiation dose estimation inside a ±15% range for fading times up to five weeks which is a very likely time span for routine dosimetry. Furthermore, it is clearly visible that the total uncertainty on the irradiation dose is mostly driven by the systematic uncertainty of the estimator F which is induced by its divergence for longer fading times and thus, a non diverging method is desirable. A possible approach to reduce the systematic uncertainty is a multivariate analysis, which is investigated in the next chapter.
In addition, scenarios with multiple irradiations are investigated [66, 56]. Furthermore, the influence of the time between annealing and irradiation is investigated in Ref. [67].

Chapter 7

Glow curve analysis with machine learning

As shown in Chapter 6, it is possible to estimate the fading time and the irradiation dose of a faded glow curve. However, the constructed fading ratio F diverged for longer fading times resulting in a large uncertainty, see Figure 6.6. This makes predictions not reliable for fading times greater than 34 d.

In order to reduce the uncertainty of the prediction for even longer fading times, more information is needed. The additional information is provided by other characteristics of the glow curve, also referred to as features.
The idea of a multivariate analysis (MVA) is to combine multiple features to calculate the prediction output. For this calculation a multitude of machine learning algorithms are available.

In this chapter the capability of a shallow neural network to predict the fading time as well as the irradiation dose of a faded glow curve is investigated.

7.1 Basics of machine learning

In machine learning, tasks can be distinguished into three categories, namely supervised, unsupervised and reinforcement learning. In all tasks the inputs of a learner are called features, independent variables or predictors.

The prediction of a known quantity, e.g. the fading time, belongs to the category of *supervised learning*. During the supervised learning, a predictive model is trained on data samples with known output, also referred to as targets or dependent variables. The model is then used to predict the target for an unknown data set. The other two categories are discussed for example in Refs. [68, 69, 70].
In supervised learning, a distinction is drawn between classification and regression. Applications, in which the input samples are divided into different classes are referred to

as *classification* tasks. These include for example the discrimination between different types of irradiation. Compared to a classification, in which the outcome is categorical, a *regression* is used to estimate a continuous target, e.g. the fading time.

The estimation of the fading time and the irradiation dose from faded glow curves are both nonlinear tasks. There are several learners which are used for a nonlinear regression, e.g. trees, support vector machines or neural networks (NNs). Using a NN has several advantages, which are discussed in Section 7.3.

7.1.1 Shallow neural network

The general idea of a NN is inspired by the information storage and organization in the brain. The simplest model is the perceptron which was introduced in Ref. [71]. These nonlinear statistic models are universal approximators, because arbitrary complex NN are capable to model any function [72].

One very simple NN is the single layer perceptron also known as a *shallow neural network*. A diagram of it is shown in Figure 7.1. It consists of an input layer with the input features

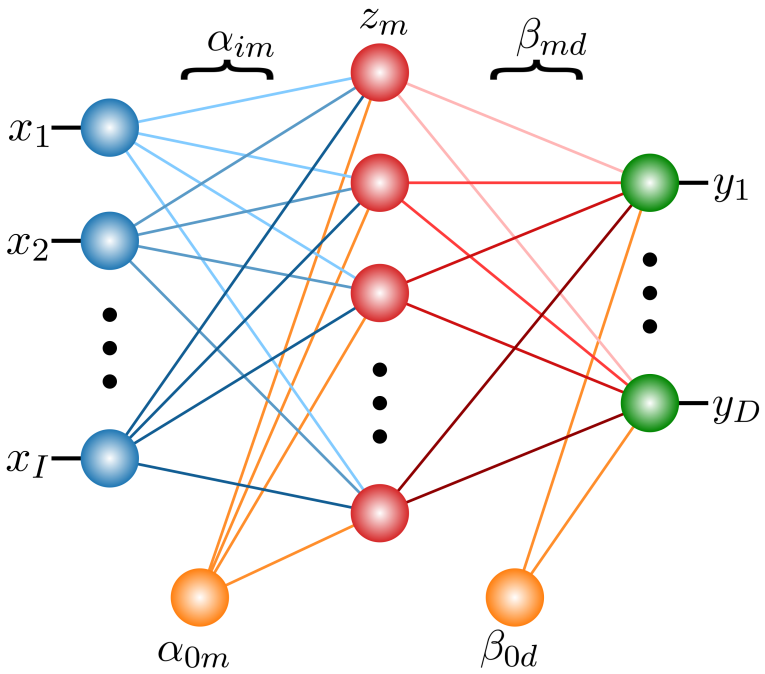

Figure 7.1: Schematic of a fully connected shallow NN. The inputs x_i (left; blue) are connected via the weights α_{im} to the hidden units z_m (middle; red). The hidden units are connected via the weight β_{md} to the targets y_d (right; green). The weights α_{0m} and β_{0d} (bottom; orange) represents the bias units feeding into every layer.

x_i ($i \in [1, I]$), one hidden layer with the hidden units z_m ($m \in [1, M]$) and an output

layer with the targets y_d ($d \in [1, D]$).
Generally, it is possible to have more than one hidden layer in a NN. In this example, each input unit is connected to every hidden unit and each hidden unit is connected to every output target. It is therefore a so-called *fully-connected neural network*. This two-stage model can be used for classification as well as for regression. In the first stage, M new features, the so-called hidden units z_m, are calculated as linear combinations of the input features x_i. The z_m have the form

$$z_m = h\left(\alpha_{0m} + \sum_{i=1}^{I} \alpha_{im} x_i\right), \tag{7.1}$$

where I is the number of input feature and h is an activation function, e.g. sigmoid or hyperbolic tangent function.
To estimate the D different targets y_d, linear combination of the hidden units z_m are used. This can be done with Equation (7.2), where σ is also an activation function which may be another than h:

$$y_d = \sigma\left(\beta_{0d} + \sum_{m=1}^{M} \beta_{md} z_m\right). \tag{7.2}$$

The weights α_{im} and β_{md} as well as the bias units α_{0m} and β_{0d} are calculated during the training process, which is done by minimizing a loss or error function.

The activation functions belong to the so-called hyperparameter which define the model of a machine learning algorithm. Other examples of hyperparameter of a shallow NN are the solver, which optimizes the weights during the fit process, or the number of hidden units M.

7.1.2 Model selection and assessment

The accuracy in future predictions is one of the major assessment criteria for a machine learning algorithm. To estimate the prediction performance, the learner is trained first and afterwards the prediction performance is tested. Using the same data set for training and testing, no generalization error can be estimated.
To avoid a wrong assessment and to get access to a good estimate of the predictive performance on unseen data, the data set can be split in a training and a test data set. The training data set is used, as the name suggests, to train the estimator and the test data set is used to estimate the learners generalization performance. As a consequence, the prediction performance, also referred to as score s, is estimated on data, which the learner does not see during the training process and accordingly does not know.

If the prediction performance on the test set is much lower than on the training set, the generalization performance is low, which is an indication for over-training. To reduce the effect of over-training and achieve a higher generalization performance, many learners use regularization.
One way to gain more generalization strength is to add a penalty term, e.g. L2 regularization, to the loss function of a regression function.

$$Loss(y_{\text{pred}}, y_{\text{true}}, \omega) = \frac{1}{2}||y_{\text{pred}} - y_{\text{true}}||_2^2 + \frac{\alpha}{2}||\omega||_2^2, \tag{7.3}$$

where y_{pred} is the predicted target, y_{true} the true target, α the regularization strength and ω the weights in the NN.

In addition to the *model assessment*, one of the main goals in machine learning is the *model selection*. Finding the best performing model includes the search for the best set of hyperparameter of a learner, as well as the comparison of different learners. Figure 7.2 shows the used approach to estimate the set of hyperparameter, for which the learner achieves the best prediction performance.

During the so-called *grid-search*, the performance of a learner with different parameter combinations (set 1 to set j) is estimated in order to find the best set. To avoid the influence of over-training on the selection of the best set, the training data is split again in a validation and a training set. With sufficient data statistics, the additional splitting has no impact on the performance, but for data sets with low statistics the validation set might be very small, which results in a relatively noisy estimate of the performance.

To counter this and still give a good estimate of the generalization performance, a *cross-validation* is performed. In a cross-validation the validation set is much smaller compared to the training set and the model is trained and validated multiple times on different parts of the data set so that more than one part of the data is used for validation.
In a K-fold cross-validation, the data is split in K equally parts, also referred to as folds. The model is trained on $K-1$ folds of the data and the remaining part is used to predict the learners performance. By altering the different folds which are used for training and validation, K scores can be estimated. The average score s_{mean} of all single validation scores s_j gives a good estimate of the learners performance.

By comparing the validation and training scores, an estimate about over-training can be made as well. The less both scores differ the more reliable is the performance estimate of the learner to unseen data. In the reality, often a trade-off between a high score and a low bias between both scores has to be found.

The major drawback of a cross-validation is that the number of fitting and predicting processes increases by a factor of K and thus, the computing time increases also with a

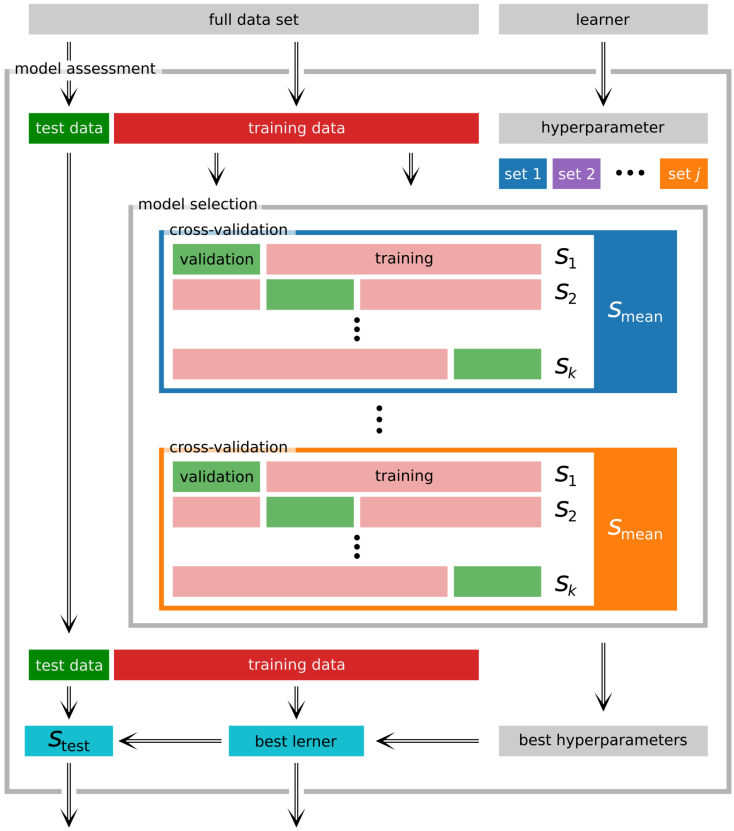

Figure 7.2: Schematic of model selection and performance assessment of a learner. To find the best set of hyperparameter, a cross-validation is performed for different combinations of hyperparameter. Afterwards the learner with the best hyperparameter set is trained on the full training data and evaluated on test data to get an estimate of the prediction error of the chosen model.

factor of K. Additionally, during a grid-search the combination of multiple parameter has to be varied, which increases the number of model evaluations and consequently, the computing time exponentially.

If the data is split in only a few folds, the validation error might have a bias and might be overestimated. In contrast, more folds result in a lower bias but the resulting scores have a higher variance due to their higher correlation. Hence, a bias-variance trade-off has to be found. The lower the statistic in the data set, the more splits should be used.

By using a cross-validation for the evaluation of every hyperparameter set during the grid-search, the best parameter combination is found reliable. With the best set of hyperparameter, the achieved score s_{test} is estimated as an estimate of the predictive performance on unseen data. Furthermore, the test data set is used to investigate the uncertainties on the predictions of the best estimator.

7.2 Application of machine learning

After the fading time as well as the irradiation dose with fading influence are estimated in Chapter 6 via the fading ratio F, a machine learning approach is investigated. By taking more features for the estimation into account, the uncertainties can be reduced.

7.2.1 Algorithms and tool boxes

Since the fading time and the irradiation dose affected by fading are continuous variables, their estimation belong to the regression tasks in machine learning, as discussed in Section 7.1. The learning is performed with the open-source software package SCIKIT-LEARN [38]. The implemented multi-layer perceptron (MLP) for regression, MLPREGRESSOR, trains with backpropagation and uses the identity function as activation function in the output layer. The mean squared error (MSE) is used as loss function and for model regularization a L2 regularization is implemented.

For the MVA presented in the following, a shallow NN with one hidden unit more than input features ($M = I + 1$) is used to estimate one output ($D = 1$) via a regression.

Different solvers are tested during the hyperparameter search, described in the next section. One of them, which is found to perform best on all feature sets, is the Limited-memory Broyden–Fletcher–Goldfarb–Shanno (L-BFGS) solver [73]. The L-BFGS is optimized for a limited amount of computer memory. The algorithm is a quasi-Newton method, which approximates the inverse Hessian matrix to optimize parameter. It is often used if the data set is small, because then it converge very fast with a high performance. The MLPREGRESSOR of SCIKIT-LEARN uses the L-BFGS implementation in SCIPY [36].

7.2.2 Calculation of input features

The input features x_i of the learner are derived from two different sources, the glow curves in time scale and the glow curve deconvolution (GCD) in temperature scale, respectively. The calculation of the features in the two domains is independent of each other. In the following, an overview of different features and their calculation is given, whereas the most important ones of both categories are discussed in more detail in the sections afterwards.

Features from glow curve in time scale

For the estimation of the features in the time domain, a region of interest (RoI), where the glow curve is significantly larger than the background, is necessary. Its length l_{RoI} is calculated by subtracting the lower edge $t_{\mathrm{RoI;low}}$ from the upper one $t_{\mathrm{RoI;up}}$.

To estimate the number of signal photons inside the RoI, $N_{\mathrm{sig;RoI}}$, the background photon counts, approximated by a linear function through the averaged photon counts before ($t < t_{\mathrm{RoI;low}}$) and after ($t > t_{\mathrm{RoI;up}}$) the RoI, are subtracted from the total number of photon counts. $N_{\mathrm{mean;RoI}}$ represents the averaged number of photons per bin inside the RoI.

The 0.25, 0.5 and 0.75 quantiles as well as their respective signal strength are estimated within the RoI, $(t_{(1/4)N}, I_{(1/4)N})$, $(t_{(2/4)N}, I_{(2/4)N})$ and $(t_{(3/4)N}, I_{(3/4)N})$, respectively. The quantiles $t_{(i/4)N}$ are normalized to l_{RoI} and the heights $I_{(i/4)N}$) to $N_{\mathrm{sig;RoI}}$. In addition, the point of maximal number of photon counts $(t_{\mathrm{max}}, I_{\mathrm{max}})$ is estimated, where t_{max} is normalized to l_{RoI} and I_{max} to $N_{\mathrm{mean;RoI}}$.

The estimation of the features derived from the glow curve in time scale are shown in the left part of Figure 7.3. As an example, the distributions of four of these features and the scatter plots are shown in Figure 7.4.

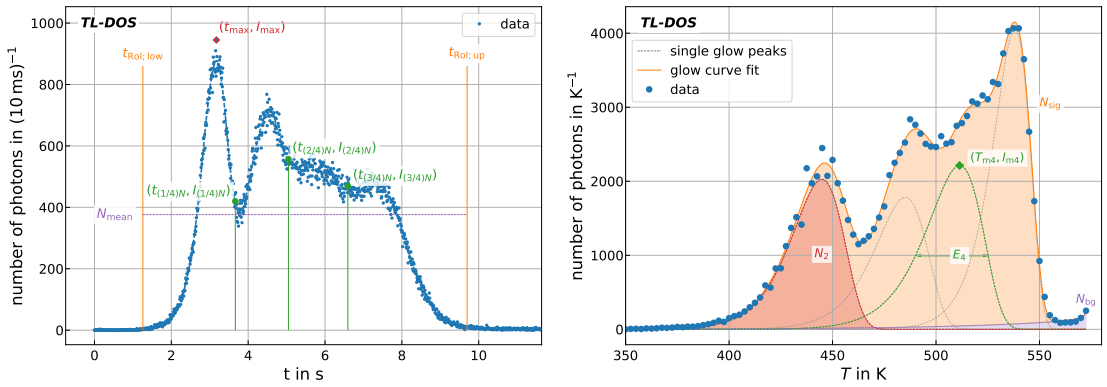

Figure 7.3: Left: Input features for MVA estimated in the time domain from the glow curve itself. Right: Features given by the fit parameter of the GCD in temperature scale.

Features from glow curve deconvolution

The GCD of the glow curve in the temperature domain provides $T_{\mathrm{m}i}$, $I_{\mathrm{m}i}$ and E_i for the four glow peaks $i \in [2, 5]$. The right part of Figure 7.3 shows some of the parameter, which are used to calculate the input features.

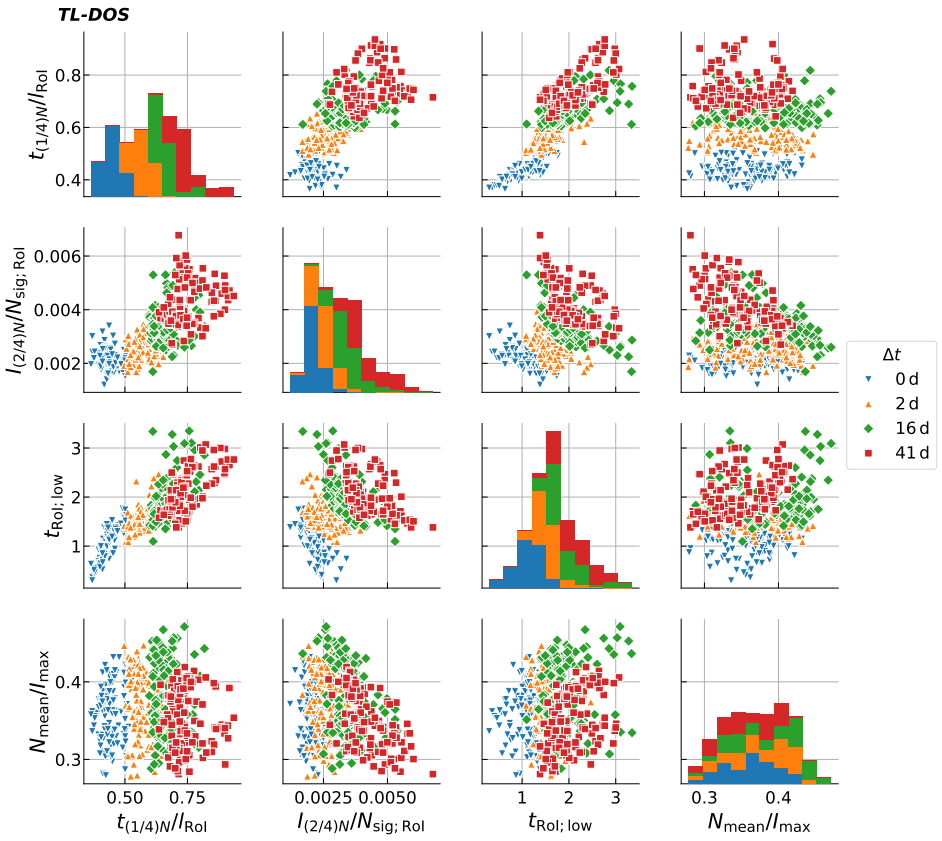

Figure 7.4: Distribution of four of the features derived from a glow curve in time scale and their correlation between each other. For simplicity, only a selection of fading times are shown.

The peak temperatures $T_{\mathrm{m}i}$ are almost independent of the fading time as well as on the irradiation dose and thus, they are not considered in an MVA, whereas the peak heights $I_{\mathrm{m}i}$ highly depend on both. For the fading time analysis different ratios of the peak heights, $I_{\mathrm{m}i}/I_{\mathrm{m}j}$ with $i \neq j$, are calculated to be independent of the irradiation dose and only sensitive to the fading time, see previous section for comparison.

The activation energy of the glow peak should actually not depend on the fading time. However, the fit parameter E_i represents an effective activation energy and since a dependency on the fading time is seen, the E_i are used as input features. E_2 is not taken into account because for longer fading times, P_2 is decreased completely and thus a reliable estimate of E_2 is difficult.

With the known $T_{\mathrm{m}i}$, $I_{\mathrm{m}i}$ and E_i of the single glow peaks, it is possible to calculate the contents of the single peaks N_i as well as the number of signal photons N_{sig}. To be independent of the irradiation dose during a fading time analysis, several peak ratios are calculated as input features N_i for the MVA, similar to the peak heights $I_{\mathrm{m}i}$. In addition,

the normalized single peak contents N_i/N_{sig}, as well as the fading ratio F from Chapter 6, $(N_4 + N_5)/N_{\mathrm{sig}}$, are used to describe the fading time behavior.

The distributions of four of these features as well as the scatter plots are shown in Figure 7.5.

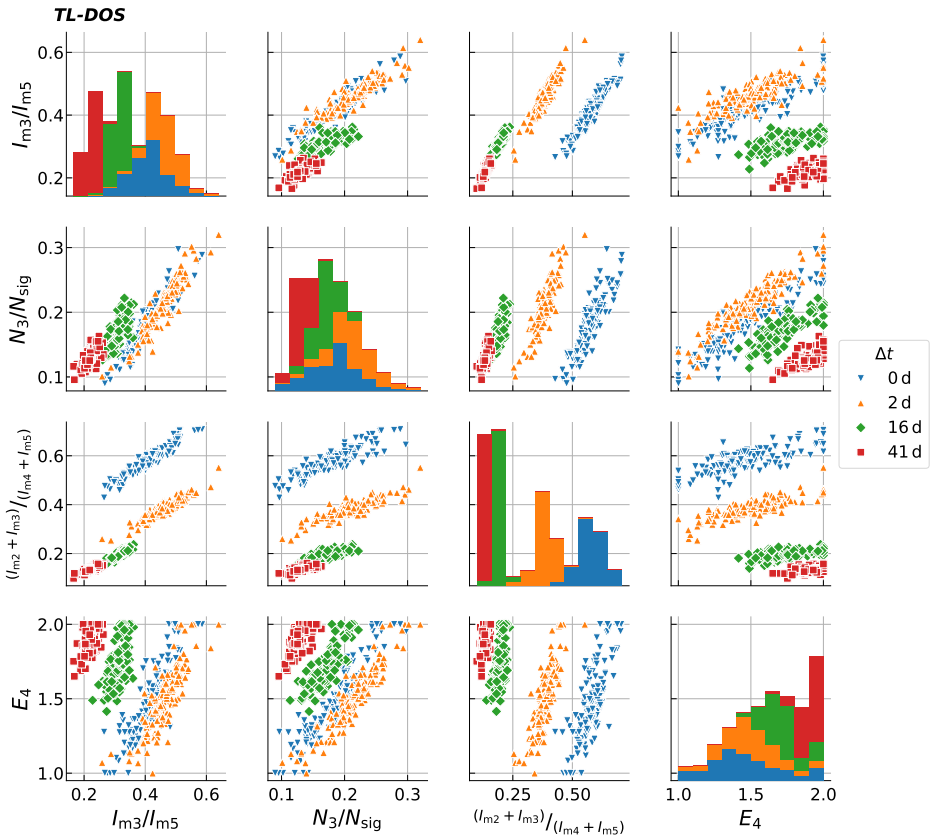

Figure 7.5: Distribution of four of the features derived from a glow curve in temperature domain and their correlation between each other. For simplicity, only a selection of fading times are shown.

7.2.3 Data preprocessing

A NN is sensitive to the scale of the input features. A feature with large values is considered more in the calculation of the output. In order to treat all features equally, all input features are standardized, which means they are scaled to mean value of zero and standard deviation of one. Since some features are highly correlated, a principal component analysis (PCA) is used to create uncorrelated features afterwards.

The PCA is an orthogonal projection of the data on a linear lower dimensional space, which maximizes the variance of projected data. Or alternatively described, it is a ro-

tation of the coordinate system, where the new coordinate axis minimizes the distance between data points and new axis. Both definitions lead to the same result. The estimated new features are called principal components and are unique with the exception of the sign. They are linearly uncorrelated, i.e. they have a unit covariance matrix, and are sorted by decreasing variance.

The explained variance ratio is measure of how much percentage of the total variance is caused by a the single component. By taking only the components with the highest explained variance ratio into account, the dimension of the data can be reduces without losing too much information. Thus, a PCA is not only used for feature decorrelation, but also for dimensionality reduction or feature extraction. However, as the projection is unsupervised the first principal components are not necessarily the most important features for a certain target. This needs to be considered if components are neglected in supervised learning.

7.2.4 Hyperparameter search

For the studies in the following sections, a grid-search is performed each time in order to find the best hyperparameter of a learner. The different hyperparameter sets are evaluated by calculating the averaged negative MSE (score) of the validation set in an 8-fold cross-validation.

The hyperparameter of the shallow NN which are varied during the grid-search is the activation function h, the strength of regularization L2 and the solver. Four activation functions are tested: the identity function ($h(x) = x$), the sigmoid function ($h(x) = 1/(1 + \exp(-x))$), the hyperbolic tangent function ($h(x) = \tanh(x)$) and the rectified linear unit function ($h(x) = \max(0, x)$). The relative strength of the penalty term of the L2 regularization is varied in a wide range between 10^{-6} and 10^{2}.
Finally, the performances of the L-BFGS, the stochastic gradient decent (SGD) and an ADAM solver are compared. ADAM stands for adaptive moment estimation and the solver is an expansion of a stochastic gradient-based optimizer [74]. Individual adaptive learning rates are used for the parameter optimization, which is done by estimating the first and second moments of the gradients. The ADAM solver performs well on large data sets with regard to time and score. Each of the solvers has several individual parameter, which define the specific update process of the weights and are varied in the grid-search as well.

In total, more than 39 000 different hyperparameter sets are tested in order to find the best learner.

7.3 Fading time estimation

For the estimation of the fading time Δt with an NN, the same data set is used as for the estimation in Chapter 6.2.1 in order to make a fair comparison. As shown in Table 4.1, the fading data set consists of four different irradiation doses with ten fading times. However, the data is not corrected for the natural radiation as in Chapter 6, because it is not possible to correct all input features for this. In addition, it is expected that a machine learning algorithm is less prone to such influences.

The test set is obtained by splitting 10% of the total data, using stratified sampling, which results in equally distributed fading time and irradiation dose combination in the data sets. The test set is used to evaluate the performance and estimate the uncertainties of the final learner.
The remaining 90% of the total data set are used to select a feature set, find the best hyperparameter and to study the over-training and robustness of the final learner. In each of the validation steps, the learner is thus trained on 79% and validated on about 11% of the total data set.

7.3.1 Feature selection

Four different feature sets are tested in order to compare their performances and find a robust set to estimate the fading time. Since the number of features differs between the single sets, the corresponding NNs differ in their complexity, because the number of units in the hidden layer ($M = I + 1$) is one more than the number of input features I.

For each feature set a grid-search is performed. A NN with a L-BFGS solver using a hyperbolic tangent as the activation function in the hidden nodes achieves the best performance on each of the four feature sets.

The first feature set contains only features that can be extracted from the glow curve without any fit or transformation. This feature set is independent of a GCD and contains 11 different features. It is not expected that this feature set performs as good as feature sets which contain features extracted by GCD, but it is taken into account to assess the performance of a NN which is independent of a previous fit or transformation.

The features of the second set are all obtained from the GCD of the glow curve after transforming it to the temperature domain. It contains 25 features which include different combinations of peak height ratios and peak integral ratios, as described in Section 7.2.2. In addition E_i is also included in the feature set. The feature set is tested to estimate the performance gain of the learner by using information from the separated glow peaks instead of the total curve.

The third feature set combines all features from the first and second feature set. With its 36 features, it contains all information obtained from the glow curve in time domain and from the GCD in the temperature domain. A learner, which used all available information, is expected to provide the best performance. However, such a high number of features results in a large number of weights in a fully connected NN. If the number of events in the data set is in the same order of magnitude as the number of weights, an over-training of the learner is more likely.

The fourth feature set is a subset of all features. The selection includes the most important features of four feature groups, namely the first feature set, all peak height ratios, all peak integral ratios and E_i, respectively. If two features within one feature group are highly correlated among each other, only one of them is used.
For longer fading times, peak P_2 is almost completely decreased and neither E_2 nor N_2 can be estimated reliable. Consequently, the integral of the second peak is not considered. In contrast to E_2, the height of the peak at a given temperature can be estimated more reliable and thus, I_2 is taken into account.
Following this procedure, seven features are selected. Since the features come from different types of group, the fourth feature set is expected to result in a good performance.

The MSE of the training as well as of the validation set using an 8-fold cross-validation are shown in Figure 7.6 for each of the four feature sets. The MSEs are calculated with the best hyperparameter set resulting from the grid-search.

With the first feature set a training and validation score using the MSE of $s = -0.024(1)$ and $s = -0.042(8)$, respectively is achieved. The offset between both scores indicates that there is a slight over-training. Furthermore, the validation score shows a high variation between the different splits of the cross-validation. Both, the offset and the high variation suggest that the information of the glow curve without any fit or transformation is insufficient for a reliable fading time estimation.

Although, the grid-search results in a much higher regularization ($\alpha = 1$) for the second feature set compared to the first one ($\alpha = 0.0001$), the training and validation score of the second set are higher than those of the first one. Since the scores agree with each other within their uncertainties, $s = -0.018(1)$ and $s = -0.020(2)$, there are no hints for an over-training. Hence, it can be concluded that the features obtained from the GCD are better to predict the fading time than those of the glow curve in the time domain.

As expected, the third feature set achieves the highest training score, $s = -0.013(1)$, of all tested feature sets. However, the validation score of $s = -0.018(3)$ is similar to that of the second feature set. Furthermore, the training process with more than thirty features takes twice as long as for the second feature set.

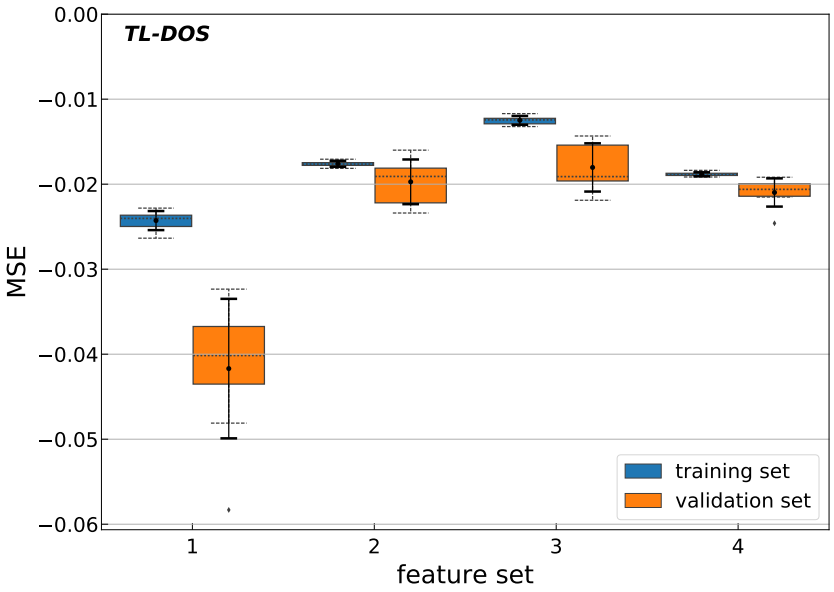

Figure 7.6: Comparison of the NN performance achieved with different feature sets. The training MSEs (blue) and the validation MSEs (orange) are estimated for each feature set with the best estimator. The distributions are shown as boxplots (dashed lines) as well as their respective mean values and standard deviation (solid lines) of an 8-fold cross-validation.

The training of the NN using the fourth feature set is about ten times faster than using the third set and five times faster using the second set. The obtained validation score of $s = -0.021(2)$ is only slightly worse than the validation score of the feature set two and three. The training score is $-0.019(1)$. Finally, the fourth feature set results in the smallest variation of the validation score, which suggest that the learner is more robust.

In conclusion, the comparison of the four feature sets shows that the third set provides the best score. However, the training is very slow and the training and validation score differ from each other. The fourth feature set is only a small subset of the third, but a similar score can be achieved with it. Therefore, it can be concluded that the contained information is sufficient to estimate the fading time. Another benefit is, that the training of the NN takes much less time compared to the other feature sets. Thus, the analysis will be performed with the forth feature set in the following.

The best performing learner on the fourth feature set is a shallow NN with eight units in one hidden layer. It uses the L-BFGS solver for parameter optimization, a hyperbolic tangent as activation function in the hidden nodes and with a regularization strength of 0.01. The seven input features are individually scaled to a mean of zero and a standard deviation of one. Afterwards they are transformed via a PCA before they are fed into the NN.

Feature importance

To estimate the importances of the seven features of the fourth set, the linear correlations between the input features and the predicted fading time are investigated.

First, the training data set is used to calculate the weights of the NN. Second, the fading times of the validation data are predicted and the correlations between the input features and the predicted fading time are calculated. Although this method only assesses the linear Pearson correlation, it is a good estimation of an estimation which features are important for the prediction.

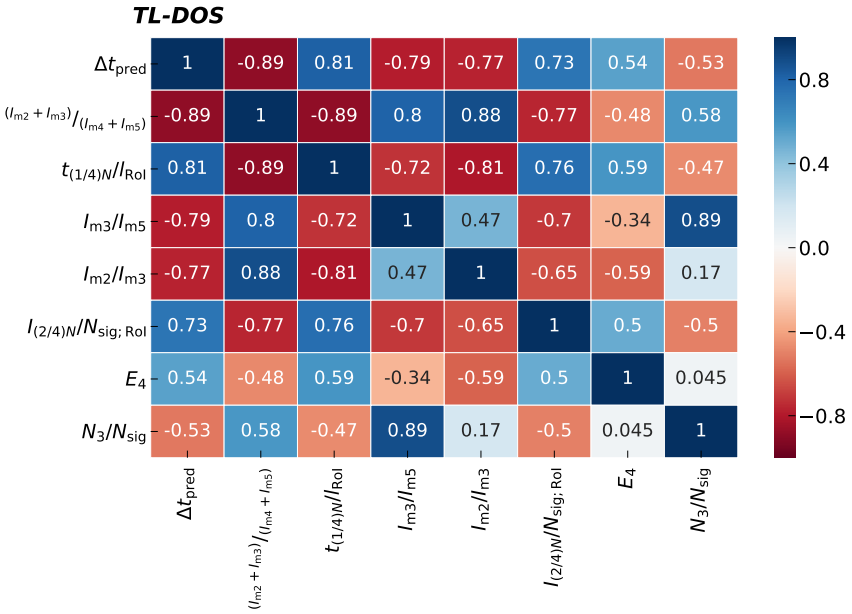

Figure 7.7: Pearson correlation between the input feature and the predicted fading time for the validation data set. The correlations are listed in descending order of the absolute correlation to the predicted fading time.

Figure 7.7 shows the correlations between the input features before the PCA and the predicted fading time. The features are listed in descending order of the absolute correlation to the predicted fading time. It turns out, that the peak height ratio $(I_{\mathrm{m2}} + I_{\mathrm{m3}})/(I_{\mathrm{m4}} + I_{\mathrm{m5}})$ has the highest correlation to the predicted fading time. The 0.25 quantile normalized to the length of the RoI, $t_{(1/4)N}/l_{\mathrm{RoI}}$, is in second place. Consequently, both a feature derived from the GCD and one from the time domain are important. The two features are also highly correlated among each other. This correlation is not caused by the calculation of both features, because one is calculated from the results of the GCD and the other is calculated from the raw glow curve.
The high correlation between $(I_{\mathrm{m2}} + I_{\mathrm{m3}})/(I_{\mathrm{m4}} + I_{\mathrm{m5}})$ and $I_{\mathrm{m2}}/I_{\mathrm{m3}}$ as well as between $I_{\mathrm{m3}}/I_{\mathrm{m5}}$ and N_3/N_{sig} is explained by the calculation of these features.

Compared to the other features, E_4 and the ratio N_3/N_{sig} show less correlation to the predicted fading time. However, E_4 is not expected to have a fading time dependence. Most information, containing in the ratio N_3/N_{sig} is already given by the peak height ratio $I_{\text{m3}}/I_{\text{m5}}$ as seen in the high correlation of both features to each other.

The scatter plots and the distributions of the three most important features are shown in Figure 7.8 together with the fading time.

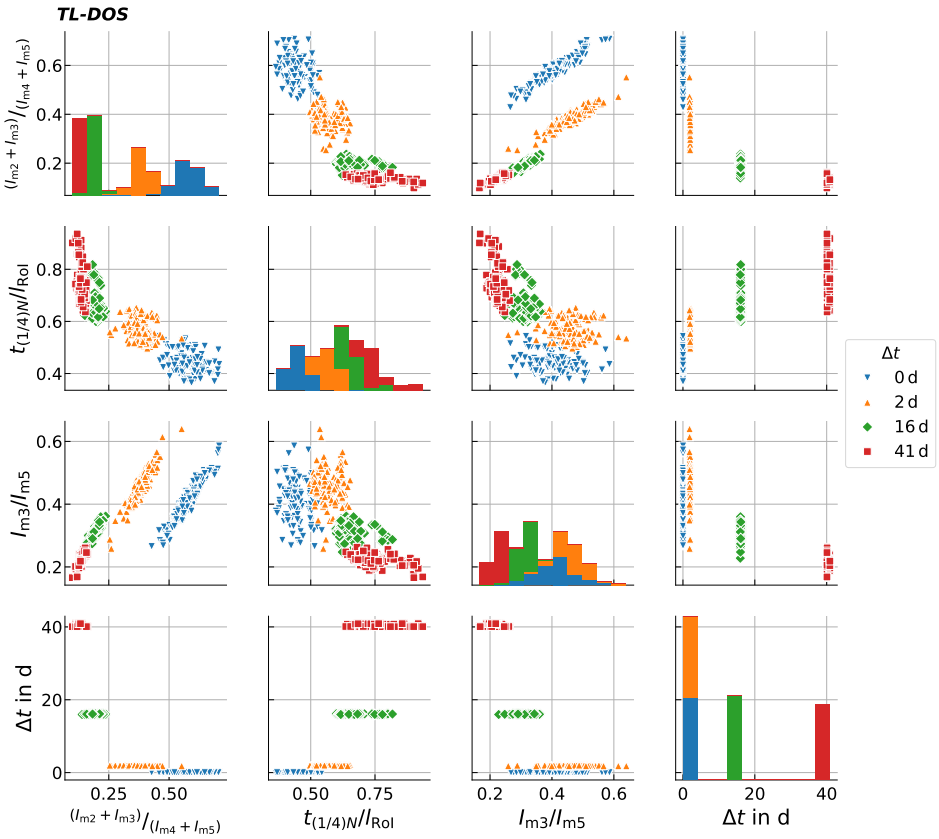

Figure 7.8: Scatter plot of the three input features, which have the highest correlation to the predicted fading time. The distribution of the fading time is also shown. For simplicity, only a selection of fading times are shown.

7.3.2 Robustness of the learner

The achieved validation score of an estimator is only one aspect of its performance assessment. Therefore, the learner is tested against over-training as well as on its robustness and linearity.

As seen in the previous section, the training and validation score of the forth feature set are slightly different. To investigate the prediction bias, the training and validation

predictions are compared to each other as a function of the fading time. The upper part of Figure 7.9 shows the predicted fading time of the training and validation data sets versus the true fading time. For each fading time, the means and its standard deviations are plotted. No deviations between the training and validation predictions of the fading

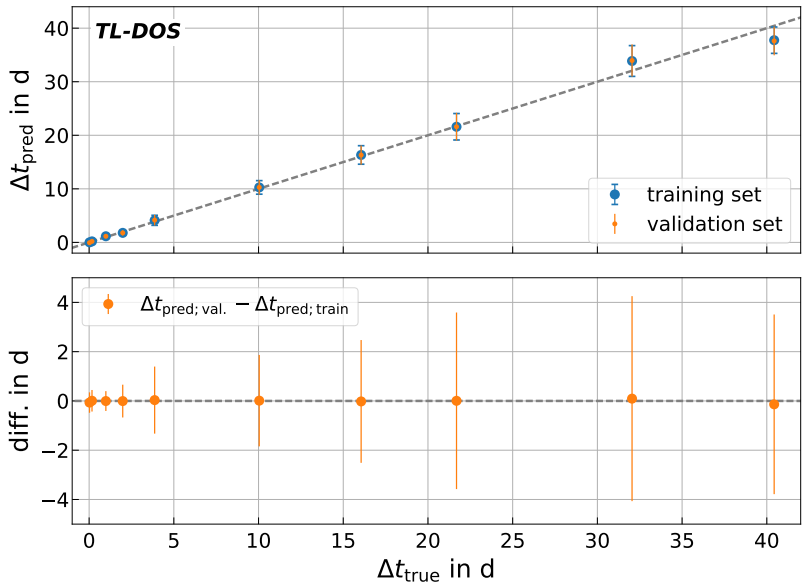

Figure 7.9: Top: Correlation between the true and the predicted fading time for the training (blue) and the validation (orange) set. The mean values and their standard deviations are calculated in an 8-fold cross-validation. Bottom: Difference between training and validation prediction as a function of the fading time.

time are visible within their uncertainties. Thus, it can be concluded that no evidence of over-training is visible.
Furthermore, it can clearly be noticed that the predictions of both sets agree to the true fading times, indicated by the dashed line in the upper part, within their uncertainties.

Due to the very discrete fading times in the data set, it is possible that the learner only memorizes the fading times of the events in the training set and then assigns the events of the validation set only to one learned fading time group. The linearity of the learner is assessed with a *leave-one-group-out* cross-validation. During this validation, the learner is trained on all fading times, except for one, and is then validated on the omitted group. Thus, the performance of the learner on fading times, which are not contained in the training data, is estimated and the interpolation strength of the learner is accessed. If the estimator has a good interpolation strength, no significant deviations between the predicted and the true fading times are expected. The deviations are shown in Figure 7.10 for the different true fading times.
By comparing the deviations of the leave-one-group-out cross-validation with those of an 8-fold cross-validation. No significant differences is seen. Only the fading times for 32 d

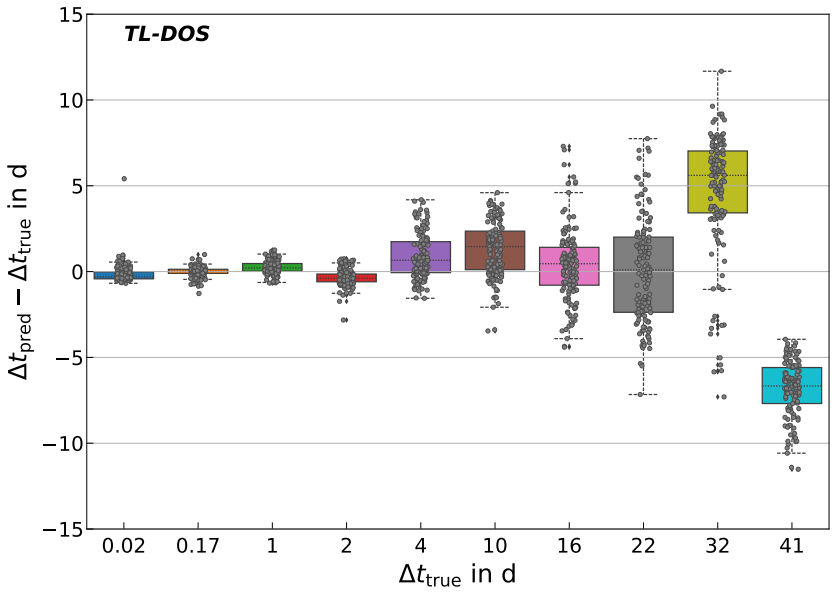

Figure 7.10: Difference between the predicted and the true fading time for a leave-one-group-out cross-validation as a function of the fading time. In addition to the boxplots of each fading time, the distributions of the differences are plotted in gray to guide the eye.

and 41 d deviate notably from the truth. However, no clustering to other fading times is seen. For a detailed study of the linearity of the learner, continuously distributed data is needed. This data is obtained by simulation as described in Ref. [56].

7.3.3 Uncertainty investigation

The uncertainty of the predicted fading time with a machine learning algorithm is calculated similarly to the uncertainty of the estimated fading time in Chapter 6.2. The total uncertainty is estimated by considering two uncertainties, the systematic and the statistic uncertainty. To estimate the uncertainties, the learner is first trained on the complete training data set and then predictions are made using the test data set.

The systematic uncertainty is defined by the systematic deviation, $u_{\Delta t;\mathrm{devi}}$, between the predicted and the true fading times. It is calculated similar to the uncertainty in Chapter 6.2. The deviations between the predicted and the true fading times are plotted as a function of the true fading times. The non-linearity is modeled by a quadratic function, which is adapted to the deviations. The uncertainty $u_{\Delta t;\mathrm{devi}}$ increase from zero to roughly half a day for a fading time of 41 d.
The uncertainty estimation of the fading time prediction with the fading ratio F also considers the systematic uncertainty of the fit-function itself. A systematic uncertainty of the learner itself is not taken into account, because as shown in the previous section,

systematic uncertainties caused by over-training can be neglected. Thus, in contrast to the fading time estimation with the fading ratio F, the systematic uncertainty does not diverge for longer fading times.

The standard deviations of the estimated fading times are used as the statistical uncertainty, $u_{\Delta t;\mathrm{stat}}$. The variations of the predicted fading times are investigated for each irradiation dose individually. It is observed, that the predicted fading times for an irradiation dose of 0.5 mSv show the highest variations compared to the other three doses. The standard deviations increase for a longer fading time to up to about 4 d after 41 d of fading. A linear function is used to approximate the fading time dependence of the variation. This function represents the maximal variation of the predicted fading times as a function of the fading time.

Figure 7.11 shows the total uncertainty, $u_{\Delta t}$, as the quadratic sum of the systematic and the statistical uncertainty. The total uncertainty of the fading time, $u_{\Delta t;F}$, estimated with the fading ratio F, is shown as well. The total uncertainty increases from about 8 h to approximately 4 d after 41 d.

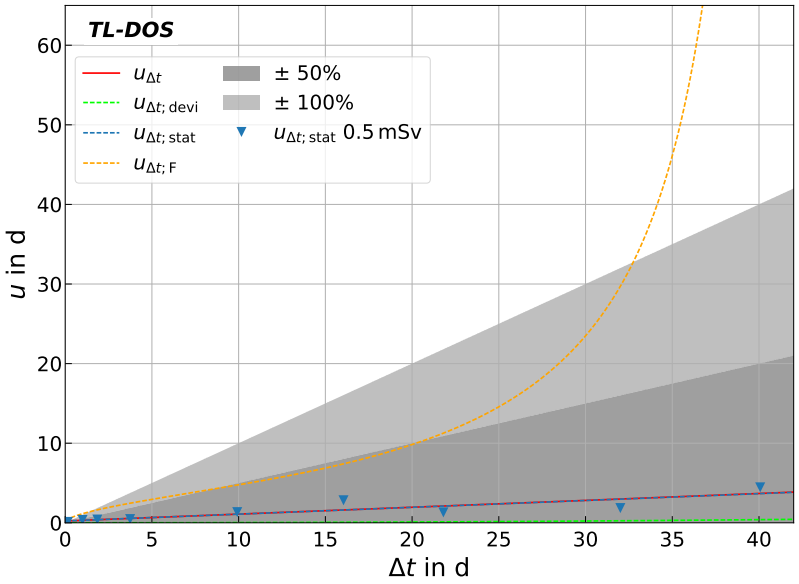

Figure 7.11: Contribution of the systematic (green) and statistical (blue) uncertainty uncertainties to the total uncertainty (red) on the estimated fading time. To guide the eye, the total uncertainty on the fading time estimated with the fading ratio (orange) is plotted as well as a 50% and a 100% range.

The statistical uncertainty dominates the total uncertainty of the predicted fading time. The non-linear systematic deviations are negligible and the estimator does not diverge for longer fading times. As a result the total uncertainty is much lower and the estimate of the fading time is more reliable for longer fading times.

7.3.4 Alternative estimator for fading time prediction

Alternatives to using a NN are decision trees or random forests, respectively. An advantage of a tree is that it is easy to interpret compared to a NN.

A decision tree divides the data set in subsets based on a threshold on one input feature, which maximizes the score of the leaves, which are the outcome of each split. The splitting is recursively repeated on each subset and is stopped if a stopping criterion is fulfilled, e.g. only one sample is left in a leaf or the score can not be increased by an additional split. In a classification task, each leaf is assigned a class label, whereas during regression a leaf represents the mean value of the output.
Another advantage of a tree based learner is that there is no need of preprocessing the data like for a NN. A tree is invariant on feature scale and theoretically non-numeric values can also be used as input features. However, a decision tree is very sensitive to details of the input data and trees, which are grown very deep, often suffer from over-training in form of large bias between training and validation score.

A *random forest* is a possible way to reduce over-training. It is an ensemble learner, which consists of multiple decision trees, whose outputs are averaged. The single decision trees are grown on various subsets of the data. The subsets are equal in size to the whole data, but are drawn from it with replacement. The best feature in a leaf is chosen from a random drawn subset of the input features, which makes the random forests more robust than a decision tree.

To get a better assessment on the prediction capability of the NN, the performance of a random forest is studied on the forth feature set and compared to the NN performance. The hyperparameter of the random forest are found by performing a grid-search. The best performing random forest uses 100 individual decision trees, which are all grown until all leaves are pure or just contain two samples. The criterion used for the estimation of the best feature is the MSE as for the NNs.

The training and validation scores of an 8-fold cross-validation compared to those of the NN are shown in the left part of Figure 7.12. The random forest provides a significantly higher training score than the NN ($-0.006(6)$ compared to $-0.019(1)$). However, a large bias is clearly visible between the training and validation score of the random forest, which indicates that the random forest suffers from over-training. In addition, the validation score of the random forest of $-0.024(3)$ is slightly lower than the one of the NN ($-0.021(2)$), but within their uncertainties both learners perform similar. Training the random forest is about four times faster than training the corresponding NN with the same feature set.

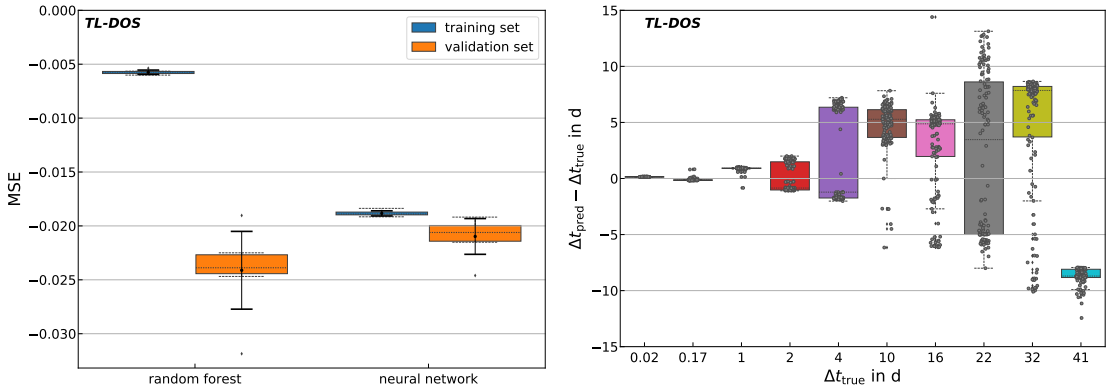

Figure 7.12: Left: Comparison of the training and validation scores of a random forest and the NN. The distributions are shown as boxplots (dashed lines) as well as their respective mean values and standard deviation (solid lines) which are estimated by an 8-fold cross-validation. Right: Difference between the predicted and true fading times of the random forest calculated with a leave-one-out-group-out cross-validation.

The linearity of the random forest is tested the same way as it was done previously for the NN. The results of the leave-one-group-out cross-validation are shown in the right part of Figure 7.12. For fading times longer than one day, the learner shows a splitting of the predicted fading times into two groups. The predicted fading times are either lower or higher than to the correct one. For example, the fading times of 4 d are either predicted two days too short (assigned to 2 d) or about six days too long (assigned to 10 d). Hence, the prediction of the random forest is more like a classification, which sorts the data in groups and does not predict a continuous fading time.
However, based on the existing data set with such low and discrete statistic, the tested random forest is not able to predict a continuous fading time.

7.4 Irradiation dose estimation with fading influences

The estimation of the fading time is only one aspect from a routine dosimetric perspective. The main quality of interest is the knowledge of the irradiation dose.

To estimate the irradiation dose the same technique as previously described in Chapter 6 is used, except that the fading time is estimated with the NN. Afterwards the initial counts and the irradiation dose are estimated. Figure 7.13 shows the systematical and statistical uncertainties of the irradiation dose. They are calculated similarly to the previously presented approach. Compared to the uncertainty of the irradiation dose, calculated with the fading ratio $u_{D;F}$, the uncertainties using the NN do not diverged for longer fading times. The uncertainty of the predicted irradiation dose is within the defined range of ±15%. For fading times up to about 25 d, both total uncertainties are

similar to each other within 8%.
The high statistical uncertainty, u_{stat}, arises from the variation of the measured number of signal photon counts in the estimation of the initial counts, see Figure 6.8, and does not come from the calculation of the fading time with the NN.

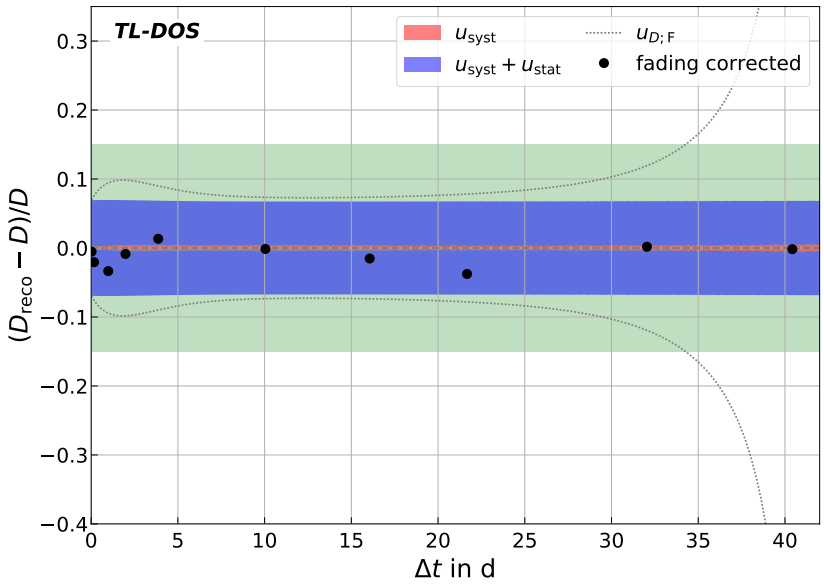

Figure 7.13: The relative deviations between the predicted and the real irradiation dose using a NN to calculate the fading time are shown. The systematic uncertainty is shown in red and the quadratic summation of the systematic and statistical uncertainties in blue. Both are plotted as a confidence interval around zero. For comparison, the total uncertainty of the estimation with the fading ratio is plotted.

The estimation of the initial counts can be circumvented, if the irradiation dose is predicted directly from the data using a machine learner. To test this approach, a NN is trained to predict the irradiation dose on the fading time data set. The forth feature set and the individual peak integrals N_2, N_3, N_4 and N_5 are used as input features. The purpose of the additional input is to give the learner the information about both, the fading time and the number of faded photon counts, to estimate an accurate irradiation dose. In order to find the best hyperparameter for the learner, a grid-search is performed.

The left part of Figure 7.14 shows the deviation between the predicted and the true irradiation dose as a function of the true irradiation dose for the training and the validation sample in an 8-fold cross-validation. No systematic deviation between the two samples, as well as between the predicted and true irradiation dose, are observed.

To test the linearity and the capability of the NN to predict unseen irradiation doses, a leave-one-group-out cross-validation is performed. The learner is trained on three of the four irradiation doses and the fourth dose is predicted. The results are shown in the right

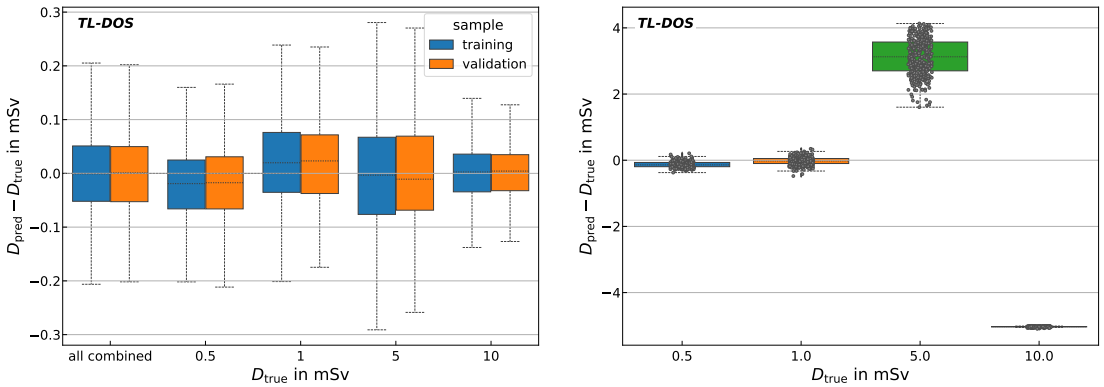

Figure 7.14: Robustness test of the NN predicting the irradiation dose. Left: Difference between the training and validation prediction as a function of the irradiation dose by using an 8-fold cross-validation. Right: Difference between the predicted and true irradiation doses of the NN calculated with a leave-one-out-group-out cross-validation.

part of Figure 7.14. The NN learns the different classes irradiation doses but learns no correlation between them. For example the data with 5 mSv are predicted about 3 mSv to high which correspond to an approximate dose of 10 mSv.

Thus, the NN is able to predict the irradiation doses, which are in the training sample, very precisely, but fails to predict unseen irradiation doses. A similar problem is seen for the random forest in the previous section. The statistic of the data is too low and too discrete for a reliable prediction. One possible solution is to use data with a continuously distributed irradiation and fading time. The easiest way to obtain this data are simulations, which are investigated in Ref. [56].

7.5 Further applications of a machine learning approach

As presented above, machine learning provides a great capability to estimate the fading time. For this reason, further applications of an MVA in the field of glow curve analysis are tested.

In Ref. [57] it was shown that it is possible to distinguish between different types of radiation based on the shape of the glow curve. The detector were irradiated with an ^{241}Am alpha-source, a ^{90}Sr/^{90}Y beta-source and a ^{137}Cs, which mainly emits gammas. For this classification task, two NNs were trained and optimized. One to distinguish between irradiations with the ^{241}Am source and the other two sources and the second NN to discriminate between the ^{90}Sr/^{90}Y and the ^{137}Cs irradiations.
Figure 7.15 shows the prediction output of both NNs for one fold of an 8-fold cross validation. The differentiation between the ^{241}Am source and the other two (left) yields

an averaged accuracy of 0.994(1). The classification between the ^{90}Sr/^{90}Y source and the

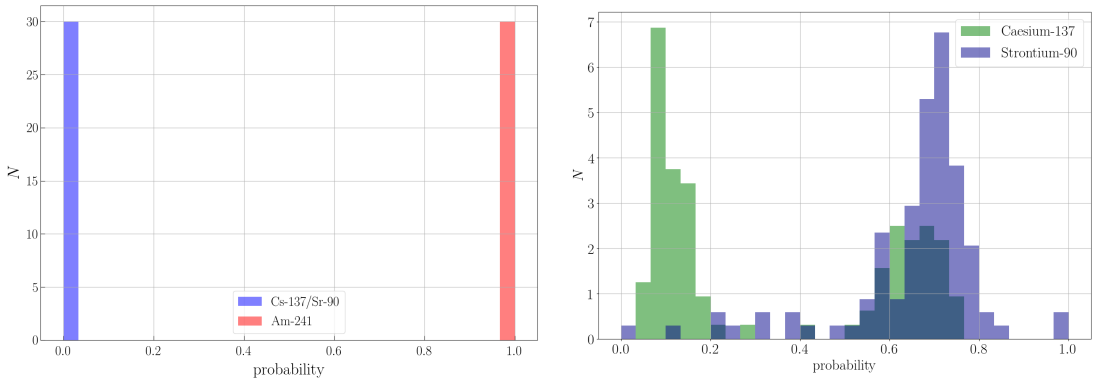

Figure 7.15: Prediction output of the NN for one fold of an 8-fold cross validation. Left: classification between the ^{241}Am source and the other two sources. Right: differentiation between the ^{90}Sr/^{90}Y source and the ^{137}Cs source. Adapted from Ref. [57].

^{137}Cs source (right) achieves a lower accuracy of 0.77(5), because it is more complicated.

A further application of machine learning is to distinguish between single- and multi-irradiations. A discrimination between both irradiations would allow to estimate whether the fading time estimation, as described in Chapter 6.2 and Chapter 7.3, can be applied or not. Several irradiation scenarios with different time spans between the multi-irradiations are measured in Ref. [66].
A trained NN has the ability to classify single- and multi-irradiations with a score of about 0.85(1). However, the NN determines the classes on the basis of the characteristics of the given irradiation scenarios and is incapable of predicting another irradiation scenario. Similar to the NN, which estimated the irradiation dose in the previous section, the statistic of the data is too low and too discrete for a reliable prediction of unseen irradiation scenarios.

One possible solution is to use simulations to generate more training data. This can be done for example with empirical simulations. In this approach, the dependency of the parameter $I_{\mathrm{m}i}$, $T_{\mathrm{m}i}$ and E_i on the fading time as well as on the irradiation dose is modeled with an empirical estimated function. The parameter itself are simulated independent of each other [56]. Thus, glow curves for different fading time and irradiation dose can be simulated with great success.
However, the parameter are correlated to each other. To include the correlations in the simulation an MVA approach is investigated [75].

As presented in the previous section, the fading time and irradiation dose estimation with a NN provides good results. The idea of a simulation approach with an MVA techniques is to revert the application and estimate parameter like $I_{\mathrm{m}i}$, $T_{\mathrm{m}i}$ and E_i from the fading

time and irradiation dose as inputs.
First results using a NN are shown in Figure 7.16. On the left figure, the correlation between the predicted parameter I_{m3} and the true one plotted. An agreement between the predictions and the true values is visible. In the right figure, a measured glow curve and a simulated one with the same dose and fading time are compared. Both curves agree well with each other.

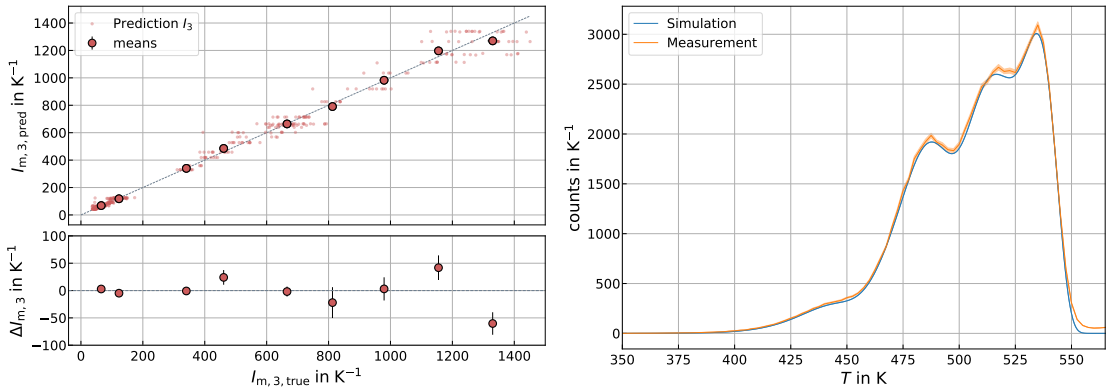

Figure 7.16: Left: Correlation between the predicted and the true I_{m3}. The bottom part shows the difference between both. Right: Comparison of a measured glow curve and glow curve simulated by using a NN. Adapted from Ref. [75].

The comparison shows, that it is possible to estimate the parameter $I_{\mathrm{m}i}$, $T_{\mathrm{m}i}$ and E_i just from the irradiation dose and the fading time and simulate a glow curve with these parameter. However, ongoing studies indicate, that the trained NN is incapable of estimating parameters for irradiation doses and fading times other than features in the training data [75].

Chapter 8

Summary and outlook

As shown it is possible to estimate the irradiation dose independent of the fading time as well as the fading time itself directly from the glow curve. Two different approaches were presented, one based on just one variable and one based on multiple variables.

The fading ratio allows for a robust estimation of the fading time independent of the irradiation dose and energy. The uncertainty on the fading time is about 50% for fading times between 5 d and 25 d and less than 100% for fading times up to 34 d. For longer fading times the systematical uncertainty increases dramatically and no reliable estimation of the fading ratio can be made.
When the fading time is known the measured signal photon counts are corrected and a fading time independent irradiation dose is estimated with an uncertainty in the given range of ±15% for fading times lower than 34 d, which is a common time interval in individual routine dose monitoring.

The uncertainties of the fading time estimation with the univariate analysis were significantly lowered by using a machine learning approach. A neural network (NN) was trained to estimate the fading time from multiple input features. The performance of NN using different feature sets was investigated and a subset of all features was identified, which optimizes the overall performance. The systematic uncertainty of the predicted fading time does not diverge for longer fading times and the total uncertainty is reduced to approximately 4 d for a fading time of 41 d. A comparison between two different types of machine learning algorithms showed that a NN performs better than a random forest on the data set which has a discrete distribution and low statistics.

To estimate the irradiation dose two approaches were studied. In the first approach the predicted fading time of the NN is used to correct the measured signal photon counts and estimate a fading time independent irradiation dose. Compared to the irradiation dose estimation using the univariate method, the total uncertainty on the irradiation dose is dominated by the statistical uncertainty and does not increase for longer fading times.

The irradiation dose can be predicted with an uncertainty of about 8% for fading times up to 41 d.
The second approach uses a NN to directly estimate the irradiation. However, due to low and very discrete statistic the learner is not able to predict unseen irradiation doses reliable. By using continuously distributed simulated data, the estimation of the irradiation dose with a NN can be improved.

The glow curves are recorded as a function of time and due to sensitivity issues the reader is not able to measure the temperature. However, both the uni- and the multivariate obtain information from the glow curve as a function of the temperature. Therefore, a method was developed to transform glow curves from the time into the temperature domain even without measuring the temperature. By estimating the peak positions in the time domain, the individual heating profile is reconstructed and the glow curve is transformed from time into temperature space.

Using the measured data, several detector and reader characteristics were studied resulting in a better understanding of the TL-DOS dosemeters. It was confirmed that the reflective layer has no visible effect on the measured TL signal and thus can be omitted. Furthermore, it has been shown that detectors from a later batch have a smaller variation in their response.
A significant decrease of the PMT's sensitivity over time was observed during the measurements. Although the reason for this loss is unknown, the data can be corrected due to reference measurements performed between them.

By using information of the individual glow peaks, the fading time of a dosemeter is estimated directly from the glow curve. With the known fading time, the estimation of the irradiation dose of TL dosemeters in the TL-DOS project is significantly improved. The results of this thesis can be applied in the field of routine dosimetry to improve the analysis.

Acronyms

EURADOS European Radiation Dosimetry Group

GCD glow curve deconvolution

$H_p(0.07)$ skin dose

$H_p(3)$ eye lens dose

$H_p(10)$ whole body dose

ICRP International Commission on Radiological Protection

IQR inter quartile range

LiF:Mg,Ti Lithium Fluorine doped with Magnesium and Titanium

MLP multi-layer perceptron

MPA NRW Materialprüfungsamt North Rhine-Westphalia

MSE mean squared error

MVA multivariate analysis

NN neural network

OSL optically stimulated luminescence

OTOR one trap one recombination center

PCA principal component analysis

PMT photo multiplier tube

PTB Physikalisch-Technische Bundesanstalt

PTFE polytetrafluoroethylene

RoeV "Röntgenverordnung", X-ray Protection Ordinance

RoI region of interest

StrlSchV "Strahlenschutzverordnung", Radiation Protection Ordinance

TL thermoluminescence

TL-DOS thermoluminescence dosemeter system

Bibliography

[1] R. Boyle. *Register of the Royal Society*, 1663:213, 1663.

[2] J. T. Randall and M. H. F. Wilkins. Phosphorescence and Electron Traps. I. The Study of Trap Distributions. *Proceedings of the Royal Society of London A: Mathematical, Physical and Engineering Sciences*, 184(999):365–389, 1945.

[3] R. Theinert et al. Computational analysis of thermoluminescence glow curves from thin layer dosemeters. *Radiation Measurements*, 106:252–256, 2017. Proceedings of the 18th International Conference on Solid State Dosimetry (SSD18), Munich, Germany, 3 – 8 July 2016.

[4] R. Theinert et al. Fading time and irradiation dose estimation from thermoluminescent dosemeters using glow curve deconvolution. *Radiation Measurements*, 108:20–25, 2018.

[5] Verordnung über den Schutz vor Schäden durch ionisierende Strahlen (Strahlenschutzverordnung - StrlSchV) , 2001. Last changed according to para. 10 persuant to para. 6 G v. 27.1.2017 I 114, 1222.

[6] Verordnung über den Schutz vor Schäden durch Röntgenstrahlen (Röntgenverordnung - RöV) . 2003. Last changed pursuant to para. 6 V v. 11.12.2014 I 2010.

[7] The 2007 Recommendations of the International Commission on Radiological Protection. *Annals of the ICRP*, 37(2-4), 2007. ICRP Publication 103.

[8] Physikalisch-Technische Bundesanstalt. PTB-Anforderungen PTB-A 23.2 "Strahlenschutzmessgeräte; Personendosimeter zur Messung der Tiefen- und Oberflächen-Personendosis", November 2013.

[9] IEC 62387: Radiation protection instrumentation - Passive integrating dosimetry systems for personal and environmental monitoring of photon and beta radiation, 2007.

[10] K.-H. Ritzenhoff et al. A new film badge for the measurement of the personal dose equivalent $H_{\mathrm{p}}(10)$ using the gliding-shadow method. In *Proceedings of the 9. International Congress on Radiation Protection, Wien 1996*, volume 4, pages 266–268. 1996.

[11] G. F. J. Garlick and A. F. Gibson. The Electron Trap Mechanism of Luminescence in Sulphide and Silicate Phosphors. *Proceedings of the Physical Society*, 60(6):574, 1948.

[12] C. E. May and J. A. Partridge. Thermoluminescent Kinetics of Alpha-Irradiated Alkali Halides. *The Journal of Chemical Physics*, 40(5):1401–1409, 1964.

[13] V. Pagonis, G. Kitis and C. Furetta. *Numerical and Practical Exercises in Thermoluminescence*. Springer-Verlag New York, 1 edition, 2006.

[14] R. Chen and V. Pagonis. *Thermally and Optically Stimulated Luminescence: A Simulation Approach*. John Wiley & Sons, Ltd, 2011.

[15] C. M. Sunta. *Unraveling Thermoluminescence*. Springer India, 1 edition, 2015.

[16] Y. S. Horowitz and M. Moscovitch. Highlights and pitfalls of 20 years of application of computerised glow curve analysis to thermoluminescence research and dosimetry. *Radiation Protection Dosimetry*, 153(1):1–22, 2013.

[17] Y. Horowitz. Thermoluminescence dosimetry: State-of-the-art and frontiers of future research. *Radiation Measurements*, 71:2–7, 2014. Proceedings of the 17th Solid State Dosimetry Conference (SSD17).

[18] J. A. Harvey, N. P. Haverland and K. J. Kearfott. Characterization of the glow-peak fading properties of six common thermoluminescent materials. *Applied Radiation and Isotopes*, 68(10):1988–2000, 2010.

[19] Radcard - TLD Dosemeters. URL `http://www.radcard.pl/index.html`, [Online; accessed 2018-06-04].

[20] B. Marczewska et al. Imaging of proton bragg peaks in LiF. *Radiation Protection Dosimetry*, 178(3):333–336, 2018.

[21] P. Bilski et al. Lithium fluoride cryatals as fluorescent nuclear track detectors. *Radiation Protection Dosimetry*, 178(3):337–340, 2018.

[22] J. Walbersloh and F. Busch. A thin-layer LiF thermoluminescence dosemeter system with fast readout for the use in personal dosimetry services. *Radiation Protection Dosimetry*, 170(1-4):191–194, 2016.

[23] Y. Lee, Y. Won and K. Kang. A method to minimise the fading effects of LiF:Mg,Ti (TLD-600 and TLD-700) using a pre-heat technique. *Radiation Protection Dosimetry*, 164(3):449–455, 2015.

[24] M. Piepenbrock. *Entwicklung einert Dosimetersonde zur Bestimmung der Tiefenpersonendosis $H_p(10)$ und der Oberflächendosis $H_p(0.07)$ mit dem Thermolumineszenz-Dünnschichtdosimeter-System TL-DOS*. Master's thesis, TU Dortmund, 2016.

[25] M. Piepenbrock et al. Development of a badge for the thin-layer thermoluminescence dosemeter system TL-DOS to measure the personal dose equivalent Hp(10) and Hp(0.07). *Radiation Measurements*, 106:543–545, 2017. Proceedings of the 18th International Conference on Solid State Dosimetry (SSD18), Munich, Germany, 3 – 8 July 2016.

[26] W. Hantke. *Labortests zur Überprüfung des routinemäßigen Einsatzes von TL-DOS Ganzkörperdosimetern*. Master's thesis, TU Dortmund, 2018.

[27] M. Heiny. *Design und Prototypen-Entwicklung eines Fingerringdosimeters zur Bestimmung der Teilkörperpersonendosis $H_p(0.07)$*. Master's thesis, TU Dortmund, 2016.

[28] K. Höner. *Untersuchung geometrischer Einflussfaktoren auf das Ansprechvermögen eines Beta-Fingerringdosimeters bei Bestrahlungen mit einem Beta-Sekundärnormal.* Master's thesis, TU Dortmund, 2017.

[29] M. Schidlowski. *Entwicklung, Charakterisierung und klinische Erprobung eines $H_p(3)$-TL-Augenlinsendosimeters.* Master's thesis, TU Dortmund, 2017.

[30] C.-M. Linker. *Feldkalibrierung eines Albedo-Neutronendosimeters in einem Protonentherapiezentrum.* Master's thesis, TU Dortmund, 2017.

[31] M. Heiny. Ph.D. thesis, TU Dortmund. Dissertation in preparation.

[32] L. Fecke. *Hochdosisverhalten von Thermolumineszenz-Dünnschichtdetektoren.* Bachelor's thesis, Heinrich Heine Universität Düsseldorf, 2015.

[33] W. Gieszczyk and P. Bilski. A simplified numerical approach to non-radiation induced high-temperature signals in thermoluminescence. GlowVIEW – a useful tool for a multiple glow-curve analysis. *Radiation Measurements*, 107:102–110, 2017.

[34] A. J. J. Bos et al. Effects of cooling and heating rate on trapping parameters in LiF:Mg, Ti crystals. *Journal of Physics D: Applied Physics*, 25(8):1249–1257, 1992.

[35] S. Mender. *Bestimmung der Nachweisgrenze des Thermolumineszenzdosimetersystems TL-DOS für die Tiefenpersonendosis $H_p(10)$.* Bachelor's thesis, TU Dortmund, 2016.

[36] E. Jones, T. Oliphant, P. Peterson et al. SciPy: Open source scientific tools for Python, 2001. URL `http://www.scipy.org`, [Online; accessed 2017-07-27].

[37] W. McKinney. Data Structures for Statistical Computing in Python. In S. van der Walt and J. Millman, editors, *Proceedings of the 9th Python in Science Conference*, pages 51–56. 2010.

[38] F. Pedregosa et al. Scikit-learn: Machine Learning in Python. *Journal of Machine Learning Research*, 12:2825–2830, 2011.

[39] J. D. Hunter. Matplotlib: A 2D Graphics Environment. *Computing in Science & Engineering*, 9(3):90–95, June 2007.

[40] M. Waskom et al. seaborn: v0.8.1, September 2017.

[41] J. van Dijk and H. Julius. Glow Curve Analysis for Constant Temperature Hot Gas TLD Readers. *Radiation Protection Dosimetry*, 47(1-4):479–482, 1993.

[42] J. van Dijk and F. Busscher. The Zero Signal and Glow Curves of Bare LiF:Mg,Ti Detectors in a Hot Gas TLD System. *Radiation Protection Dosimetry*, 101(1-4):59–64, 2002.

[43] H. Stadtmann, C. Hranitzky and N. Brasik. Study of real time temperature profiles in routine TLD read out—influences of detector thickness and heating rate on glow curve shape. *Radiation Protection Dosimetry*, 119(1-4):310–313, 2006.

[44] A. Savitzky and M. J. E. Golay. Smoothing and Differentiation of Data by Simplified Least Squares Procedures. *Analytical Chemistry*, 36(8):1627–1639, 1964.

[45] A. Lütfring. *Charakterisierung des Aufheitsverhaltens und glühkurvenbasierte Rekonstruktion der Detektortemperatur eines Dünnschicht-Thermolumineszenzdosimeters.* Master's thesis, TU Dortmund, 2016.

[46] G. Kitis, J. M. Gomez-Ros and J. W. N. Tuyn. Thermoluminescence glow-curve deconvolution functions for first, second and general orders of kinetics. *Journal of Physics D: Applied Physics*, 31(19):2636–2641, 1998.

[47] A. Bos et al. An Intercomparison of Glow Curve Analysis Computer Programs: I. Synthetic Glow Curves. *Radiation Protection Dosimetry*, 47(1-4):473–477, 1993.

[48] A. Bos et al. An Intercomparison of Glow Curve Analysis Computer Programs: II. Measured Glow Curves. *Radiation Protection Dosimetry*, 51(4):257–264, 1994.

[49] V. Pagonis, S. Mian and G. Kitis. Fit of First Order Thermoluminescence Glow Peaks using the Weibull Distribution Function. *Radiation Protection Dosimetry*, 93(1):11–17, 2001.

[50] V. Pagonis and G. Kitis. Fit of Second Order Thermoluminescence Glow Peaks Using the Logistic Distribution Function. *Radiation Protection Dosimetry*, 95(3):225–229, 2001.

[51] G. Kitis et al. Thermoluminescence under an exponential heating function: I. Theory. *Journal of Physics D: Applied Physics*, 39(8):1500–1507, 2006.

[52] G. Kitis et al. Thermoluminescence under an exponential heating function: II. Glow-curve deconvolution of experimental glow-curves. *Journal of Physics D: Applied Physics*, 39(8):1508–1514, 2006.

[53] M. Moscovitch, Y. Horowitz and J. Oduko. LiF Thermoluminescence Dosimetry via Computerised First Order Kinetics Glow Curve Analysis. *Radiation Protection Dosimetry*, 6(1-4):157–159, 1983.

[54] Y. Horowitz, M. Moscovitch and M. Wilt. Computerized glow curve deconvolution applied to ultralow dose LiF thermoluminescence dosimetry. *Nuclear Instruments and Methods in Physics Research Section A: Accelerators, Spectrometers, Detectors and Associated Equipment*, 244(3):556–564, 1986.

[55] G. Kitis, E. Carinou and P. Askounis. Glow-curve de-convolution analysis of TL glow-curve from constant temperature hot gas TLD readers. *Radiation Measurements*, 47(4):258–265, 2012.

[56] F. Mentzel. Master's thesis, TU Dortmund, 2018. Thesis in preparation.

[57] M. Steil. *Glühkurvenanalyse zur Unterscheidung von Strahlungsarten mittels Multivariaten Analysemethoden.* Bachelor's thesis, TU Dortmund, 2018.

[58] Y. Horowitz. Editorial - Fading in LiF:Mg,Ti. *Radiation Protection Dosimetry*, 32(3):147, 1990.

[59] S. Doremus and G. Higgins. Pre-Irradiation Fade and Post-Irradiation Fade for LiF:Mg,Ti, TLD-600, and TLD-700, as a Function of Time. *Radiation Protection Dosimetry*, 54(2):119–125, 1994.

[60] C. Furetta, C. Kuo and P. Weng. Fading prediction in thermoluminescent materials using computerised glow curve deconvolution (CGCD). *Nuclear Instruments and Methods in Physics Research Section A: Accelerators, Spectrometers, Detectors and Associated Equipment*, 423(1):183–189, 1999.

[61] M. Weinstein et al. A simple method for avoiding fading correction of absorbed dose from glow curves of TLD-100. *Radiation Measurements*, 37(1):81–86, 2003.

[62] M. Moscovitch. Automatic Method for Evaluating Elapsed Time Between Irradiation and Readout in LiF-TLD. *Radiation Protection Dosimetry*, 17(1-4):165–169, 1986.

[63] C. Furetta and J. Azorín. Simultaneous determination of dose and time elapsed since irradiation using CaSO4:Dy thermoluminescent dosimeters. *Nuclear Instruments and Methods in Physics Research Section A: Accelerators, Spectrometers, Detectors and Associated Equipment*, 280(2):318–321, 1989.

[64] M. Budzanowski et al. Estimation of the Time Elapsed Between Exposure and Readout Using Peak Ratios of LiF:Mg,Cu,P (MCP-N,GR200A). *Radiation Protection Dosimetry*, 85(1-4):149–152, 1999.

[65] J. A. Harvey and K. J. Kearfott. Reproducibility of glow peak fading characteristics of thermoluminescent dosimeters. *Radiation Measurements*, 46(3):319–322, 2011.

[66] J. Lingweiler. *Vorstudie zur Unterscheidung von Einfach- und Mehrfachbestrahlung von Thermolumineszenzdosimetern mithilfe von Multivariater Analyse*. Bachelor's thesis, TU Dortmund, 2018.

[67] L. Speicher. *Untersuchung des Einflusses von Pre-Irradiation-Fading auf Glühkurven*. Bachelor's thesis, TU Dortmund, 2018.

[68] C. Bishop. *Pattern Recognition and Machine Learning*. Information Science and Statistics. Springer, 2006.

[69] T. Hastie, R. Tibshirani and J. Friedman. *The Elements of Statistical Learning: Data Mining, Inference, and Prediction, Second Edition*. Springer Series in Statistics. Springer New York, 2 edition, 2009.

[70] M. Kubat. *An Introduction to Machine Learning*. Springer International Publishing, 2 edition, 2017.

[71] F. Rosenblatt. The perceptron: A probabilistic model for information storage and organization in the brain. *Psychological Review*, 65(6):386–408, 1958.

[72] K. Hornik, M. Stinchcombe and H. White. Multilayer feedforward networks are universal approximators. *Neural Networks*, 2(5):359–366, 1989.

[73] J. Nocedal. Updating Quasi-Newton Matrices with Limited Storage. *Mathematics of computation*, 35:773–782, 07 1980.

[74] D. P. Kingma and J. Ba. Adam: A Method for Stochastic Optimization. *CoRR*, abs/1412.6980, 2014.

[75] L. Röhrig. Bachelor's thesis, TU Dortmund, 2018. Thesis in preparation.

Danksagung

An dieser Stelle möchte ich mich bei allen bedanken, die mich während meines Studiums unterstützt und mir geholfen haben, diese Arbeit anzufertigen.

Zuerst möchte ich Prof. Dr. Kevin Kröninger danken, der mir die Möglichkeit gegeben hat, an seinem Lehrstuhl zu arbeiten und mich während dieser Zeit betreut hat.

Des Weiteren möchte ich Prof. Dr. Dr. Wolfgang Rhode sowie allen Mitgliedern der Prüfungskommission meinen Dank aussprechen, dass sie sich bereit erklärt haben, meine Arbeit zu lesen und zu bewerten.

Zudem bin ich Jörg, HWK, Myriam und dem gesamten Team am MPA sehr verbunden, dass sie mir während der Durchführung meiner Messungen mit Rat und Tat zur Seite standen.

Für die gute Zusammenarbeit, die schöne Zeit am Lehrstuhl sowie die leckeren Kuchen möchte ich mich bei allen aktuellen und ehemaligen Mitgliedern des Lehrstuhl EIV bedanken und möchte dabei besonders die beiden guten Seelen des Lehrstuhls, Markus und Andrea, hervorheben.

Mein Dank gilt auch Jens, Olaf und Flo die meine Arbeit kritisch gelesen haben und mir mit dem ein oder anderen Kommentar geholfen haben, sie zu verbessern. Abschließend möchte ich noch Flo besonders danken, der mir geholfen hat, die verschiedenen Fits und Berechnungen in unsere Software zu implementieren, zu testen und zu dokumentieren.

Zu guter Letzt möchte ich besonders meiner Familie und meiner Freundin sagen:
Danke, dass ihr immer für mich da seid.